GENERATION OF HIGH INTENSITY FEMTOSECOND LASER PULSES AND APPLICATIONS TO STUDIES OF TRANSIENT PHENOMENA

by

James G. Fujimoto

S.B., Massachusetts Institute of Technology
(1979)

S.M. and E.E., Massachusetts Institute of Technology
(1981)

SUBMITTED IN PARTIAL FULFILLMENT OF THE REQUIREMENTS

FOR THE DEGREE OF

DOCTOR OF PHILOSOPHY

at the

MASSACHUSETTS INSTITUTE OF TECHNOLOGY

Signature of Author James G. Fujimoto
Department of Electrical Engineering and Computer Science
May 1, 1984

Certified by _____
Thesis Supervisor

Accepted by _____
Chairman, Departmental Committee on Graduate Students

GENERATION OF HIGH INTENSITY FEMTOSECOND LASER PULSES AND APPLICATIONS TO STUDIES OF TRANSIENT PHENOMENA

by

James G. Fujimoto

Submitted to the Department of Electrical Engineering and Computer Science on May 1, 1984 in partial fulfillment of the requirements for the degree of Doctor of Philosophy.

ABSTRACT

This thesis research concerns the development of a femtosecond gigawatt dye laser amplifier and its application to the investigation of ultrafast transient physical processes. Several experimental studies have been performed which develop and extend time resolved spectroscopy into the femtosecond regime to obtain new results on specific topics of current scientific interest in nonlinear optics and solid state physics. These investigations include:

1. Transient four wave mixing and optical gating. Scattered pulse durations in parametric mixing are examined both theoretically and experimentally. The application of this process for optical gating and pulse shortening has been demonstrated by the generation of high intensity pulses of 37 femtoseconds duration.

2. Generation and measurement of optical pulses as short at 16 femtoseconds. Amplified 65 femtosecond pulses have been compressed to 16 femtoseconds using nonlinear self phase modulation in a short optical fiber followed by compression with a diffraction grating pair. These pulses consist of only eight optical cycles and are the shortest optical pulses produced to date.

3. Multiphoton photoemission and nonequilibrium electron/lattice temperatures in tungsten. High intensity 75 femtosecond optical pulses have been used to observe multiphoton and thermally assisted photoemission and to produce nonequilibrium electron heating in tungsten. Pump-probe measurements indicate an electron-phonon energy transfer time of several hundred femtoseconds. This constitutes the first direct time resolved measurement of electron-phonon energy relaxation in metals.

4. Femtosecond time resolved exciton dynamics in CdSe. The transient behavior of the exciton resonance in highly excited CdSe has been investigated by femtosecond pump and continuum probe reflectivity measurements. Screening by free carriers is observed to develop in less than 100 femtoseconds. This is the first investigation of screening in II-VI semiconductors performed on a femtosecond time scale.

Thesis supervisor: Erich P. Ippen
Title: Professor of Electrical Engineering

This thesis is dedicated to:

Frank Barrows

and

Issai Lefkowitz

Whose lives and work embody

a true spirit of Excellence and Honor

ACKNOWLEDGEMENTS

This research represents the combined help and guidance of many people. It is a great pleasure to express my sincere thanks and appreciation to all who have made this research program possible.

First and foremost I would like to express my gratitude to my advisor, Professor Erich Ippen, for his guidance and support. His broad scientific experience and keen physical insight have made my doctoral studies with him a truly enriching and educational experience. I am especially grateful for his patience, understanding, and encouragement throughout this research.

I would like to thank Professor Hermann Haus and Professor Mildred Dresselhaus for their expert advice and guidance as members of my thesis committee. Their suggestions and critical comments have contributed greatly to this thesis and are sincerely appreciated. I am also grateful to Professor Nicolaas Bloembergen for valuable advice on various aspects of this research.

I wish to express my sincere thanks to my colleagues and collaborators, Drs. Jia-Ming Liu, Sergey Shevel, Sandro DeSilvestri, and Carmen Puliafito. Their experience and expertise have made much of this research possible. It has been a pleasure to work with them and I am grateful for their friendship and support. I would especially like to thank Any Weiner, a fellow graduate student and colleague. Without his expert research on the intricacies of the femtosecond ring laser, this project would not have been possible. I would also like to thank members of the picosecond optics and integrated optics group, especially Chris Gabriel, Ghavam Ghavamishahidi, Mohammed Islam, Lynne Molter-Orr, Mike Stix, and Dr. Ernst

Wintner, for many helpful discussions and comments. The undergraduate research work of Ed Bade and Paul Dresselhaus is also gratefully acknowledged.

I would like to thank the staff of the Research Laboratory of Electronics, especially Donna Gale, Frank Barrows, Henry Stram, Richard Keyes, George Leach, Joe Mitchell, Joe Sincuk, and Dave Taylor. Without their technical and administrative skills, this laboratory would not exist.

I would like to thank my friends and colleagues, Bart and Jeanne Johnson, Mansour Shayegan, and Eileen Schwartz, whose help and friendship enriched my graduate years.

I would especially like to express my sincere thanks and appreciation to Dr. Steve T.K. Yee. A good friend and expert scientist, it has been a great pleasure to work with him these past years.

I would also like to express my sincere thanks and appreciation to Carla Millhauser for her emotional support, encouragement, and inspiration throughout these difficult years of graduate study as well as her expert editing and typing skills in the preparation of this manuscript.

Finally I wish to thank my parents whose continued patients, support, and understanding have made this all possible. Their belief in the true value of scholarship and learning has been an inspiration throughout all of my studies.

TABLE OF CONTENTS

Page

LIST OF FIGURES

LIST OF TABLES

CHAPTER 1

INTRODUCTION

The passively modelocked ring dye laser and multiple stage dye amplifier is one of the few laser systems capable of producing optical pulses shorter than 100 femtoseconds in duration and is presently the only source of high intensity femtosecond pulses (1-3). This thesis research involves the development of a femtosecond gigawatt dye amplifier and its application to the investigation of ultrafast transient physical processes in nonlinear optics and solid state physics.

A four stage femtosecond dye amplifier has been constructed. Pumped with a Nd/YAG laser and used in conjunction with a modelocked ring dye laser, the femtosecond dye amplifier operates at 620 nm and produces 65-85 femtosecond pulses with peak intensities of up to several gigawatts. These high intensities allow the investigation of nonlinear and high excitation phenomena as well as the use of nonlinear optical techniques for the generation of femtosecond optical pulses at other wavelengths. The femtosecond dye laser and amplifier is thus a powerful and highly versatile experimental system which provides the basis for a comprehensive research program in femtosecond time resolved spectroscopy.

In addition, this thesis develops and demonstrates new femtosecond generation and measurement techniques as well as extends picosecond spectroscopy into the femtosecond regime. Several experimental studies have been performed which demonstrate the application of time resolved spectroscopy with high intensity femtosecond pulses to obtain new results on specific topics of current scientific interest in nonlinear optics and solid state physics. The investigations which have been performed include:

1. Transient Four Wave Mixing and Optical Gating in the Femtosecond Regime - The transient behavior of parametric scattering four wave mixing has been investigated both experimentally and theoretically (4,5). Special emphasis is placed on the measurement of scattered pulse duration and the determination of material time constants such as population and dephasing relaxation times. Experimental investigations have been performed which demonstrate the application of this process for optical gating and pulse shortening. High power pulses of 37 femtoseconds duration have been generated.

2. Generation and Measurement of Optical Pulses as Short as 16 Femtoseconds - Amplified 65 femtosecond pulses have been compressed to 16 femtoseconds using nonlinear self phase modulation in a short optical fiber followed by pulse compression with a diffraction grating pair (6). These pulses consist of only eight optical cycles and are the shortest optical pulses generated to date. Pulse duration measurements were obtained by noncollinear second harmonic generation autocorrelation in a thin crystal of KDP. A discussion of the generation and measurement techniques relevant to extremely short pulse durations is presented.

3. Multiphoton Photoemission and Nonequilibrium Electron and Lattice Temperatures in Tungsten - High intensity 75 femtosecond optical pulses have been used to observe multiphoton and thermally assisted photoemission from a tungsten metal surface. Evidence has been found for the generation of a transient thermal nonequilibrium between the electrons and lattice (7). Pump-probe measurements indicate an electron-phonon energy transfer time of several hundred femtoseconds.

This constitutes the first direct, time resolved measurement of electron-phonon energy relaxation in metals.

4. Femtosecond Time-Resolved Exciton Dynamics in CdSe - The transient behavior of the exciton resonance in highly excited CdSe is experimentally investigated by femtosecond pump and continuum probe reflectivity measurements (8). The onset of screening by free carriers is observed to develop in less than 100 femtoseconds. This is the first investigation of screening in II-VI semiconductors performed on a femtosecond time scale.

REFERENCES

1. R.L. Fork, B.I. Greene, and C.V. Shank, "Generation of Optical Pulses Shorter than 0.1 psec by Colliding Pulse Mode Locking," Appl. Phys. Lett. 38, 671 (1981).

2. R.L. Fork, C.V. Shank, and R.T. Yen, "Amplification of 70-fs Optical Pulses to Gigawatt Powers," Appl. Phys. Lett. 41, 223 (1982).

3. R.L. Fork, C.V. Shank, R. Yen, and C. Hirlimann, "Femtosecond Optical Pulses," IEEE J. Quantum Electron. QE-19, 500 (1983).

4. J.G. Fujimoto and E.P. Ippen, "Transient Four Wave Mixing and Optical Pulse Compression in the Femtosecond Regime," Opt. Lett. 8, 446 (1983).

5. J.G. Fujimoto and T.K Yee, "Influence of Dephasing Relaxation on the Transient Properties of Parametric Four-Wave Mixing," Applied Physics B, in press.

6. J.G. Fujimoto, A.M. Weiner, and E.P. Ippen, "Generation and Measure ment of Optical Pulses as Short at 16 Femtoseconds," Applied Physics Letters, in press.

7. J.G. Fujimoto, J.M. Liu, E.P. Ippen, and N. Bloembergen, "Multiphoton Photoemission and Nonequilibrium Electron and Lattice Temperatures in Metallic Tungsten," to be presented at the Ultrafast Phenomena Conference of the Optical Society of America, Monterey, California, June, 1984.

8. J.G. Fujimoto, S.G. Shevel, and E.P. Ippen, "Femtosecond Time-Resolved Exciton Dynamics in CdSe," Solid State Commun. 49, 605 (1984).

CHAPTER 2

THE FEMTOSECOND EXPERIMENTAL LASER SYSTEM

2.1 INTRODUCTION

The femtosecond laser system which is the heart of this research program consists of a colliding pulse modelocked (CPM) ring dye laser (1) and multiple stage dye amplifier (2,3). The CPM ring laser was developed by a fellow graduate student, Mr. Andrew Weiner. Mr. Weiner has been responsible for the construction of the ring laser and the implementation of a research program which utilizes the high repetition rate, low intensity output from this laser. My research has centered on the development and construction of the multiple stage femtosecond dye amplifier and the implementation of an experimental program which utilizes high intensity femtosecond optical pulses.

Construction of the laser systems began in the summer of 1981 and was not completed until the fall semester of 1982. Modifications and improvements to the laser system continue even at present. It is anticipated that the femtosecond system which was constructed by Mr. Weiner and myself will provide a foundation for an ongoing research effort in femtosecond spectroscopy and will be utilized by future generations of graduate students and researchers.

2.2 THE COLLIDING PULSE MODELOCKED RING DYE LASER

The colliding pulse modelocked (CPM) ring dye laser was first demonstrated by Fork et al (1) in 1981 and is a direct descendent of the linear cavity passively modelocked dye laser developed by Ippen and Shank (4-6) almost a decade ago. The previous linear cavity passively modelocked dye

laser could produce pulse durations of 0.7 ps with pulses as short as 0.3 ps obtainable by pulse compression techniques (6). The colliding pulse modelocked (CPM) ring dye laser is capable of producing pulses as short as 55 femtoseconds with better stability and lower fluctuations than possible from the previous linear cavity lasers. The modelocking mechanism is similar to that which occurs in linear passively modelocked lasers (7,8) except that the use of a ring geometry allows the simultaneous oscillation of two counter-propagating pulses which travel around the cavity and coherently interact or collide in the saturable absorber. The CPM ring geometry also allows the counter-propagating pulses to be amplified separately in the gain media. Theoretical investigations show that the improved modelocking performance may be in part attributed to an increased stability region (9) as well as an increase in the effective saturable absorber cross section (10) over linear modelocking. However, it is also possible that four wave mixing or phase conjugation may play an important role in the improved pulse durations and stability observed from the CPM lasers.

Figure 2.1 shows a schematic diagram of the CPM ring dye laser that has been constructed in our laboratory. Pump power is provided by a cw Argon ion laser (Spectra Physics Model 171) at typical intensities of 4-6 W. The gain medium is a flowing jet of Rhodamine 6G in ethylene glycol. Passive modelocking is accomplished by a thin jet of 3,3'-Diethyloxadicarbocyanine iodide (DODCI) in ethylene glycol. The colliding pulse modelocking process is most effective and provides the shortest pulses when the dimensions of the saturable absorber dye jet are comparable to or shorter than the laser pulse length and the saturable absorber is highly

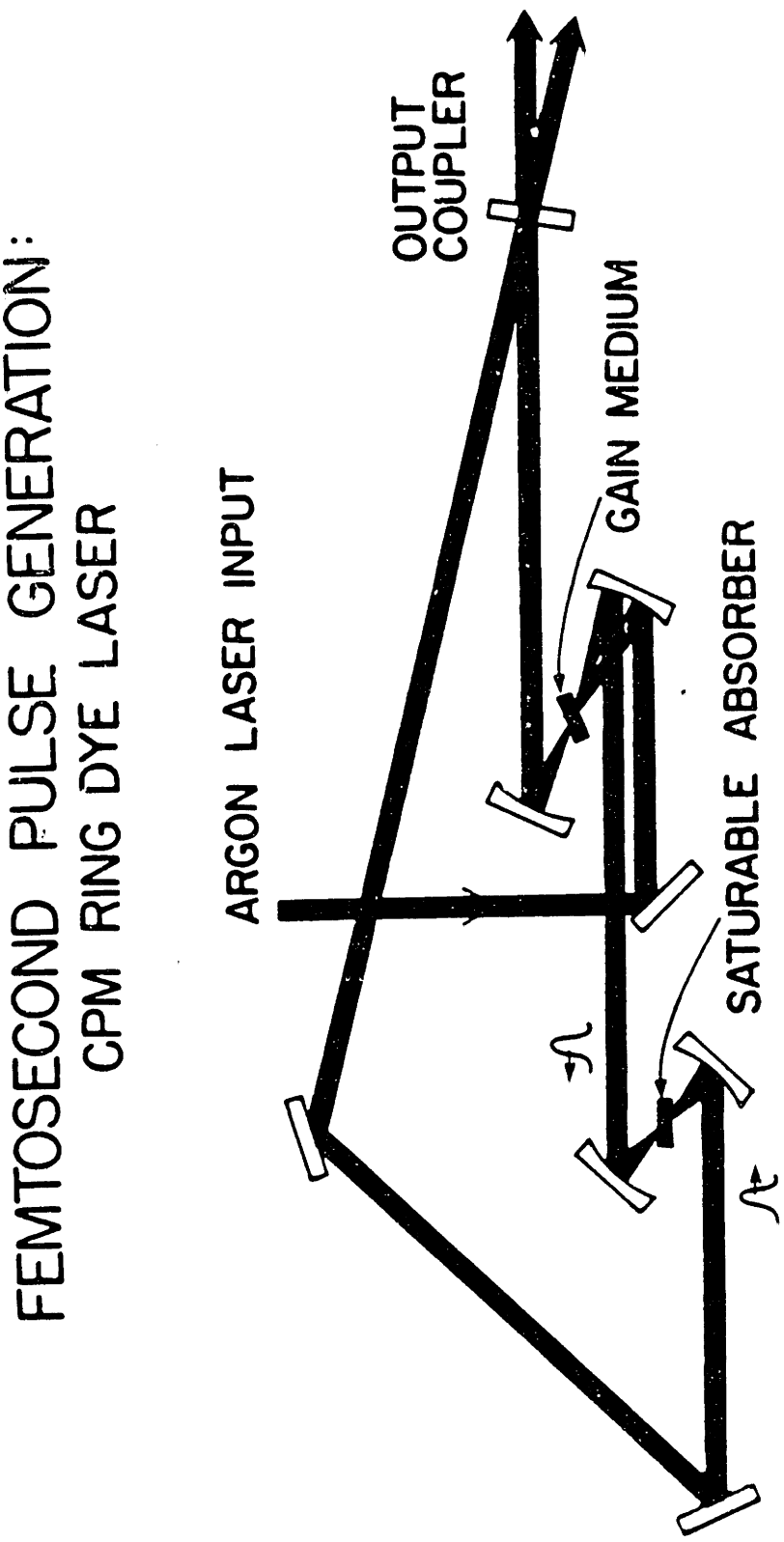

Figure 2.1 Schematic diagram of colliding pulse modelocked ring laser.

concentrated. This acts to enhance the coherent interaction of the counter-propagating pulses within the saturable absorber.

Pulse duration measurements of the modelocked ring laser output were performed by noncollinear, background free, second harmonic generation autocorrelation in a nonlinear KDP crystal (11). Figure 2.2 shows an autocorrelation trace of the ring laser output obtained under optimum operating conditions. The full width at half maximum FWHM of the autocorrelation is 85 femtoseconds. Assuming a sech^2 incident pulse shape, this implies a FWHM pulse duration of 55 femtoseconds. The pulse durations obtained under normal operating conditions are typically 65-75 femtoseconds.

The laser oscillates at a wavelength of approximately 620 nm with a spectral bandwidth of $\sim$10 nm to produce near transform limited coherent pulses with negligible substructure. The pulse repetition rate is $\sim$8 ns as determined by the transit time around the ring cavity. The average power in each of the two output beams is $\sim$15 mW. This yields single pulse energies of $\sim$120 pJ with peak intensities of $\sim$2 kW.

2.3 THE FEMTOSECOND DYE AMPLIFIER

Multiple stage dye amplifiers were first introduced in the mid 1970s for use with Nd:YAG and nitrogen pumped dye lasers (12,13). These systems produced high intensity pulses of several nanoseconds duration or longer with narrow spectral bandwidth and were designed principally for applications to nonlinear optics and spectroscopy of atomic or molecular vapors. The use of a multiple stage dye amplifier for picosecond pulses was first demonstrated by Ippen and Shank in 1978 (14,15). In conjunction with a linear cavity passively modelocked dye laser, this system consisted of a three stage amplifier pumped by a Nd:YAG laser and was capable of

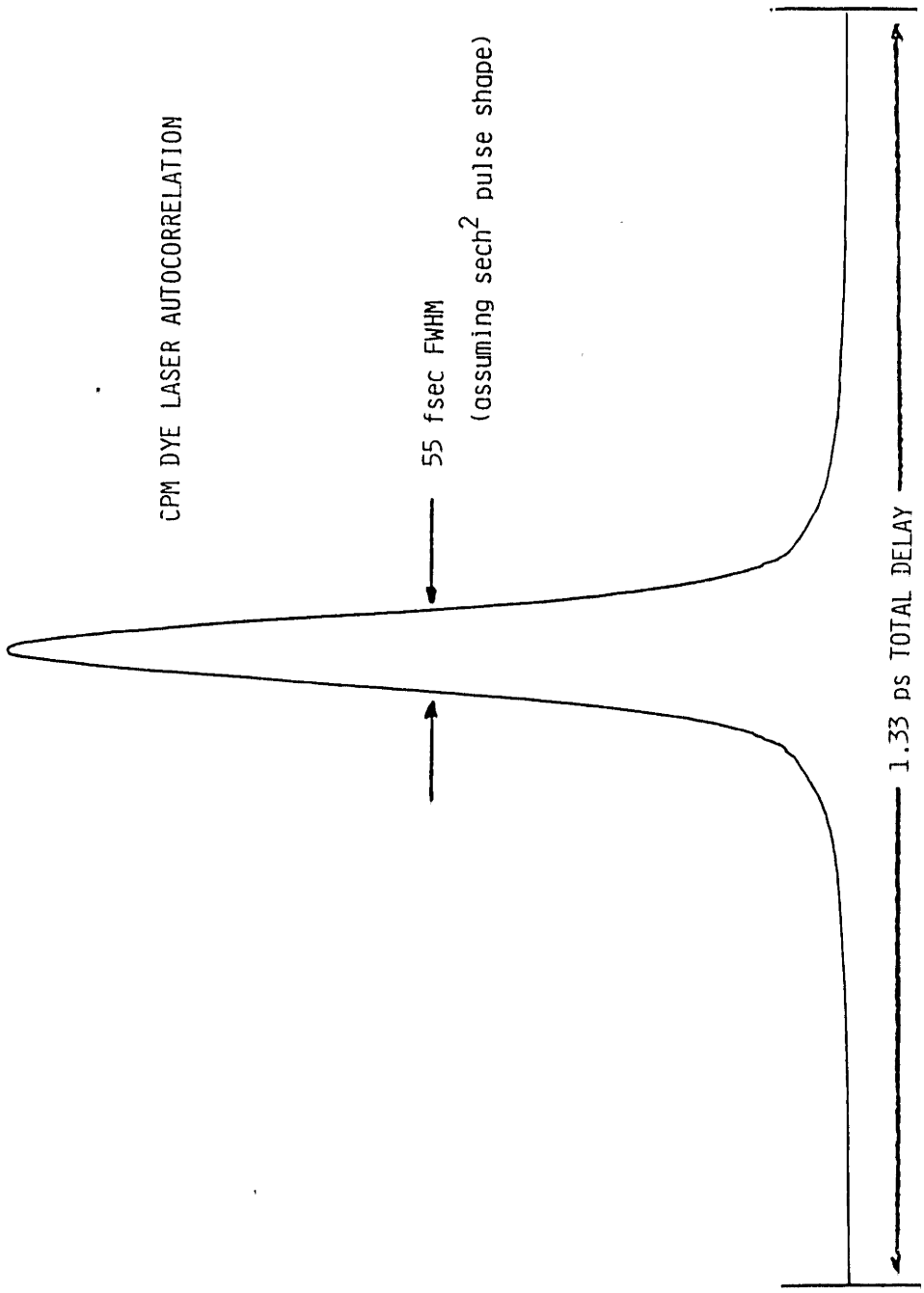

Figure 2.2 Autocorrelation of modelocked ring laser output.

producing 0.5 picosecond pulse durations with peak powers of 3 GW. Subsequently, other types of multistage dye amplifiers have also been developed for use with picosecond synchronously modelocked dye lasers (16,17). With the advent of the colliding pulse modelocked ring dye laser, these high power amplification techniques could be extended into the femtosecond regime. Using a four stage Nd:YAG pumped dye amplifier, Fork et al in 1982 (2,3) demonstrated the generation of 70-90 femtosecond amplified pulses with peak powers of 0.3-2 GW.

The multiple stage dye amplifier that has been developed and constructed in our laboratory is similar in design to that described by Fork et al (2,3). The amplifier consists of four gain stages pumped by a Nd:YAG laser operating at 10 Hz. The total gain is approximately 10^7 to produce output pulses of 400 microjoules with 75-85 femtoseconds duration yielding peak powers in excess of 5 GW.

A schematic diagram of the amplifier is shown in Figure 2.3. There are four gain stages G1-G4 isolated by three saturable absorber jets SA1-SA3. The pump laser is a Q-switched, frequency doubled Nd:YAG (Quanta Ray DCR1) which produces 150 mJ pulses at 532 nm with a repetition rate of 10 Hz. A photodiode is used to monitor the output pulse train from the CPM ring laser and fire the Nd:YAG at an optimum time so that a single optical pulse is selected for amplification. In practice, the stability of the multistage dye amplifier is directly related to the Nd:YAG laser stability and is particularly sensitive to fluctuations in the temporal substructure of the YAG laser pulses. By redesigning the YAG laser Q-switch and carefully optimizing operating parameters, it was possible to obtain 8 ns pulse durations with stable 2 ns substructure. In addition, it was necessary to carefully synchronize the YAG laser to the CPM output to a

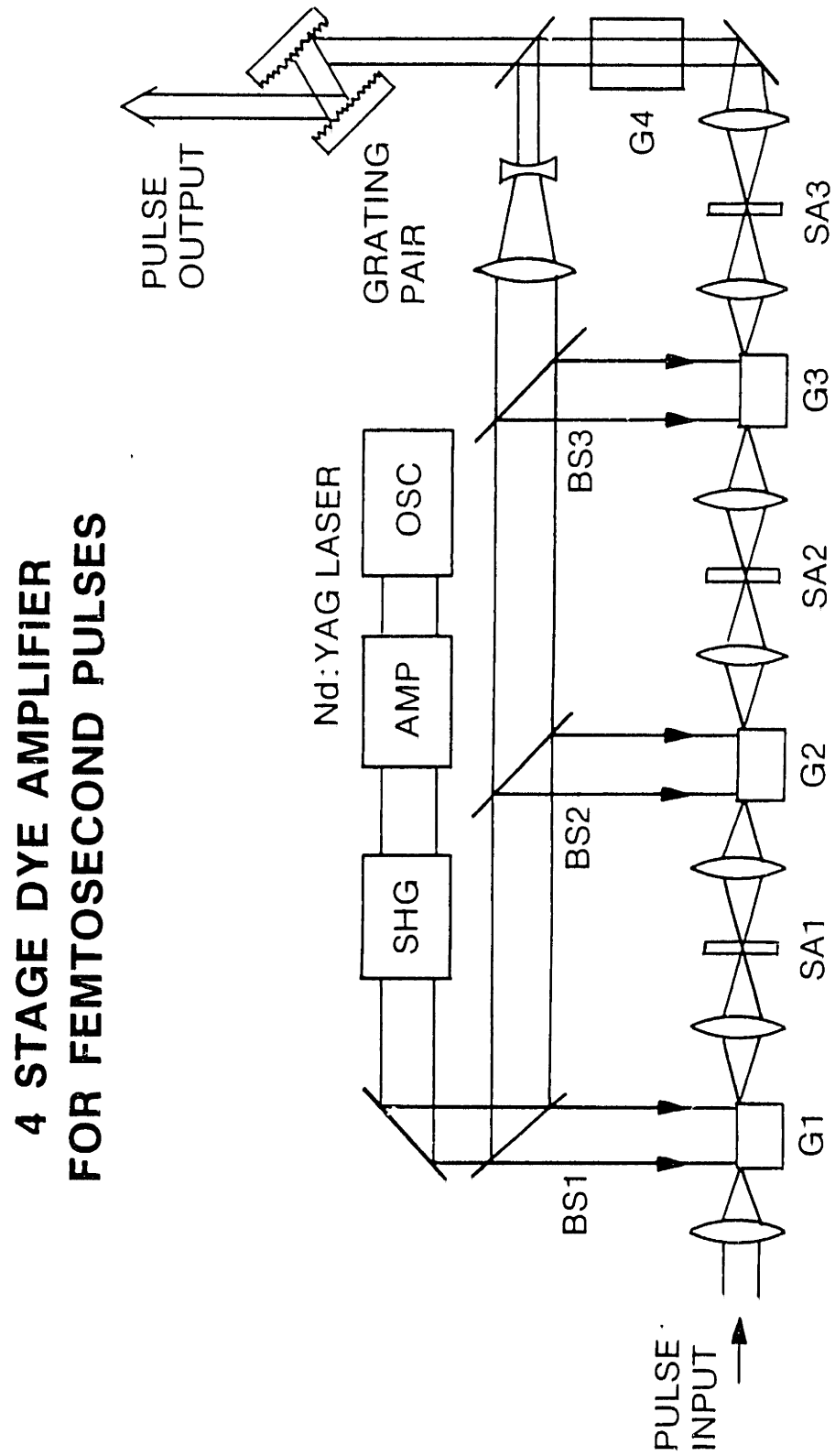

Figure 2.3 Schematic of four stage femtosecond dye amplifier.

precision of less than 1 ns. Under these conditions, the stability of the dye amplifier pulse energy fluctuations was better than 10-15% rms. The shot-to-shot energy fluctuations of the amplified femtosecond pulses are directly relevant to obtaining high signal to noise ratios in experimental measurements using this system. Fluctuations and signal averaging problems are especially critical in view of the fact that many experimental investigations involve the measurement of highly nonlinear processes.

As shown in Figure 2.3, the first three stages of the amplifier are transversely pumped while the increased pulse energy in the fourth stage necessitates longitudinal pumping. The Nd:YAG laser beam is first expanded to a diameter of 40 mm to pump stages G1-G3, then reduced to a diameter of 1 cm for longitudinal pumping in G4. Beamsplitters select approximately 5%, 5%, and 20% of the pump energy for the first three stages respectively while the fourth stage is pumped in a collinear counter-propagating geometry using a dichroic mirror. Most of the stored energy is contained in the final stage.

The gain medium in the first stage is a highly concentrated 2.5 x 10^{-4} M solution of Kiton Red with 1% Ammonix L.O. added to prevent dimer formation. The remaining stages employed successively more dilute solutions of Sulforhodamine 640 with concentrations of 7 x 10^{-5} M, 5 x 10^{-5} M, and 1 x 10^{-5} M. The dye concentrations in the transversely pumped stages could be empirically chosen by making the penetration depth of the Nd:YAG pump beam comparable to the amplified beam diameter. This insured a relatively homogenous gain across the transverse profile of the amplified beam. The concentrations were also optimized to compromise between gain and excessive spontaneous emission. Kiton Red was chosen for the first stage because its peak spontaneous emission wavelength was not highly amplified by

the Sulforhodamine 640 in the remaining stages. Both dyes were matched to the output wavelength and bandwidth of the CPM dye laser.

The transversely pumped gain stages were constructed with 3 cm path length quartz dye cells tilted close to Brewster's angle with respect to the amplified beam. The pump beams were coupled into the cells by focussing with cylindrical lenses. The cells used flowing dye solutions circulated at low flow rates by gear pumps and filtered to remove air bubbles. Teflon inserts were positioned in the cells to restrict the dye flow to the pumped region near the edge of the cell. This resulted in a long, thin gain medium and prevented amplified spontaneous emission in the transverse direction which would result in self-dumping (12). The fourth stage consisted of a 4 cm long cylindrical flow cell with Brewster angle windows. In each stage a careful alignment of the CPM femtosecond laser beam and the Nd:YAG pump was required in order to maximize gain while preventing amplified spontaneous emission.

Special attention is required to design the dye amplifier system so that it yields the proper gain without compromising pulse duration or producing excessive amplified spontaneous emission noise. Saturable absorber jets of Malachite green in ethylene glycol SA1-SA3 were employed between the gain stages to isolate the stages and prevent amplified spontaneous emission as well as to preserve the short pulse durations. Dye concentrations were adjusted to produce small signal attenuations of 10^{-2}, 10^{-3}, and 10^{-3} in the saturable absorbers SA1-SA3 respectively. The amplified beam diameter was successively expanded before each stage to avoid gain saturation from the high peak intensities. The beam diameters were 0.5, 2, 5, and 10 mm in stages G1-G4 respectively. The approximate gain in the stages was 750, 100, 50, and 10. Including losses, this yielded a

total amplifier gain of approximately 10^7.

Dispersive pulse broadening which occurs in the gain media and optical elements of the amplifier was compensated for by a pair of 600 l/mm diffraction gratings (18) separated by a slant distance of approximately 4 cm. A suitable adjustment of the diffraction gratings could also precompensate for any dispersive optical elements within the experimental system. However, special care is required to avoid any nonlinear frequency generation effects which were prone to occur in the saturable absorbers and fourth stage. These effects would produce pulse broadening which could not be compensated for by diffraction grating recompression. Before the gratings, the amplified pulses were approximately 400 femtoseconds in duration with energies of 1 mJ. Grating recompression yielded 75-85 femtosecond duration pulses (see Figure 2.4) with energies of 400 microjoules.

In summary, the four stage femtosecond dye amplifier has a total gain of approximately 10^7 and produces pulse durations of 75-85 femtoseconds with energies of 400 microjoules at a wavelength of 620 nm. The repetition rate is 10 Hz and is limited by the Nd:YAG pump laser. Amplified pulse energy fluctuations are less than 10-15% rms.

2.4 APPLICATIONS OF HIGH INTENSITY FEMTOSECOND PULSES

The femtosecond colliding pulse modelocked ring dye laser and four stage dye amplifier constitute a powerful and versatile system for femtosecond time resolved spectroscopy. Although the low repetition rate of the amplifier precludes many of the powerful signal averaging techniques which may be employed in conjunction with the modelocked ring dye laser, the high peak powers available from amplified pulses allow a wide variety

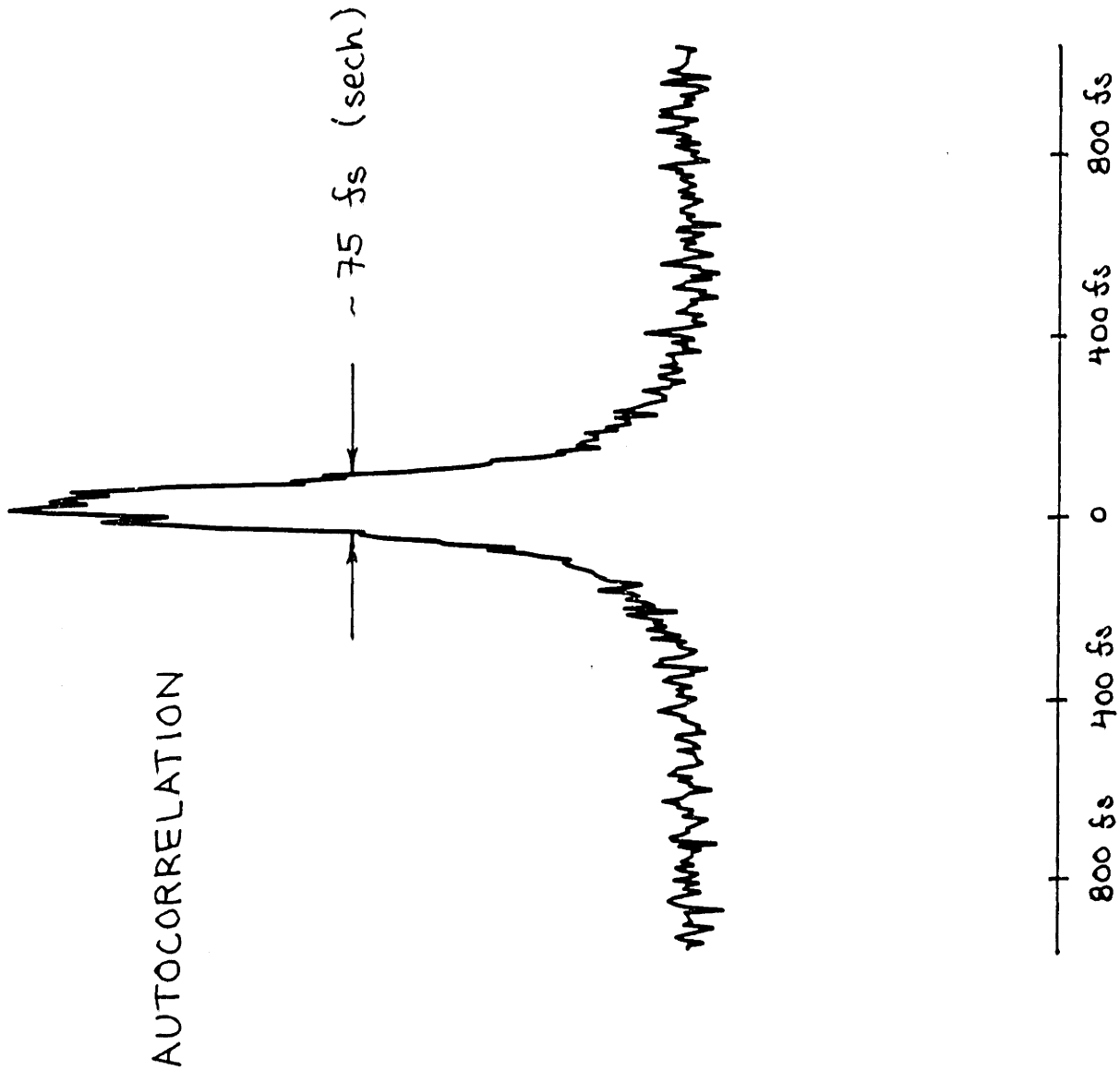

Figure 2.4 Autocorrelation of amplified femtosecond laser pulses.

of experimental studies which would be impossible with low intensity femtosecond pulses.

High intensity pulses may be applied to the time resolved investigation of many nonlinear phenomena which would be difficult to observe at lower intensities. The use of short pulse duration often makes possible the generation of nonlinear effects which would occur above the damage threshold of the material if longer pulse durations were employed. In addition, high intensity pulses make possible the study of high excitation phenomena and phase transitions. These topics are of special interest in the field of solid state and semiconductor physics. For example, previous investigators have applied high intensity femtosecond techniques to the study of phenomena such as plasma formation (19) and melting (20) in silicon.

Finally and perhaps most significantly, the femtosecond dye amplifier allows the application of nonlinear optical techniques for the generation of femtosecond pulses at wavelengths other than the fundamental laser output. This is particularly relevant to femtosecond optical studies in solid state physics in view of the fact that many semiconductors of interest in electronics or electro-optics have band gaps in the near infrared. Furthermore, the use of multiple wavelength pump-probe experiments can generally provide a more complete and accurate description of transient physical processes than measurements performed at a single wavelength. There are essentially three different techniques which may be applied to generate femtosecond pulses at other wavelengths. These include Raman scattering, continuum generation, and nonlinear parametric amplification.

Stimulated Raman scattering has been used effectively in the picosecond pulse regime for shifting the pulse wavelengths into the near infrared

(14). Although high conversion efficiencies are possible, only relatively small wavelength shifts can be produced and, assuming a fundamental wavelength of 620 nm, the technique is effective only out to wavelengths of ∿750 nm. In addition, many of the Raman lines become transient on a femtosecond time scale.

Perhaps the most powerful technique at present is continuum generation by self phase modulation (21). Self phase modulation occurs when an intense optical pulse is incident on a material which has an intensity dependent index of refraction. The presence of the rapidly changing intensity induces a temporal variation of the material index which in turn modulates the optical field frequency. Continuum generation in materials such as H_2O, D_2O, and ethylene glycol produces a relatively featureless broadband white light continuum which extends from approximately 300 nm in the ultraviolet out to almost 1.6 microns in the near infrared. By performing continuum generation in a thin jet of ethylene glycol in order to prevent dispersive pulse broadening, previous investigators (21) have observed continuum pulse durations of less than 100 femtoseconds. Although the conversion efficiency is relatively low, the broadband femtosecond continuum is ideally suited for use as a probe in pump-probe measurements of transient absorption or reflectivity.

Finally, one of the potentially promising techniques for the generation of femtosecond pulses in the near infrared is the use of parametric amplification. In this approach the amplified femtosecond pulses would be used to generate a continuum as well as to pump a nonlinear crystal such as lithium niobate or lithium iodate to parametrically amplify selected portions of the continuum. Variations of this approach have been used to construct parametric oscillators for the generation of tunable picosecond

pulses (22,23). However, pulse broadening from group velocity mismatch and dispersion may provide a serious limitation to the amplification of femtosecond pulse durations using this technique.

REFERENCES

1. R.L. Fork, B.I. Greene, and C.V. Shank, "Generation of Optical Pulses Shorter than 0.1 psec by Colliding Pulse Mode Locking," Appl. Phys. Lett. 38, 671 (1981).

2. R.L. Fork, C.V. Shank, and R.T. Yen, "Amplification of 70-fs Optical Pulses to Gigawatt Powers," Appl. Phys. Lett. 41, 223 (1982).

3. R.L. Fork, C.V. Shank, R. Yen, and C. Hirlimann, "Femtosecond Optical Pulses," IEEE J. Quantum Electron. QE-19, 500 (1983).

4. E.P. Ippen, C.V. Shank, and A. Dienes, "Passive Mode Locking of the CW Dye Laser," Appl. Phys. Lett. 21, 348 (1972).

5. C.V. Shank and E.P. Ippen, "Subpicosecond Kilowatt Pulses from a Mode-Locked CW Dye Laser," Appl. Phys. Lett. 24, 373 (1974).

6. E.P. Ippen and C.V. Shank, "Dynamic Spectroscopy and Subpicosecond Pulse Compression," Appl. Phys. Lett. 27, 488 (1975).

7. G.H.C. New, "Pulse Evolution in Mode-Locked Quasi-Continuous Lasers," IEEE J. Quantum Electron. QE-10, 115 (1974).

8. H.A. Haus, "Theory of Mode Locking with a Slow Saturable Absorber," IEEE J. Quantum Electron. QE-11, 736 (1975).

9. D. Kuhlke, W. Rudolph, and B. Wilhelmi, "Calculation of the Colliding Pulse Mode Locking in CW Dye Ring Lasers," IEEE J. Quantum Electron. QE-19, 526 (1983).

10. M.S. Stix and E.P. Ippen, "Pulse Shaping in Passively Mode-Locked Ring Dye Lasers," IEEE J. Quantum Electron. QE-19, 520 (1983).

11. E.P. Ippen and C.V. Shank, Ultrashort Light Pulses: Picosecond Techniques and Applications, S.L. Shapiro, ed., Springer-Verlag, New York, 1977, p. 83.

12. P. Drell and S. Chu, "A Megawatt Dye Laser Oscillator-Amplifier System for High Resolution Spectroscopy," Opt. Commun. 28, 343 (1979).

13. R. Wallenstein and H. Zacharias, "High Power Narrowband Pulses Dye Laser Oscillator-Amplifier System," Opt. Commun. 32, 429 (1980).

14. E.P. Ippen and C.V. Shank, Picosecond Phenomena, C.V. Shank, E.P. Ippen, and S.L. Shapiro, eds., Springer-Verlag, New York, 1978, p. 103.

15. A. Migus, C.V. Shank, E.P. Ippen, and R.L. Fork, "Amplification of Subpicosecond Optical Pulses: Theory and Experiment," IEEE J. Quantum Electron. QE-18, 101 (1982).

16. T. Sizer II, J.D. Kafka, A. Krisiloff, and G. Mourou, "Generation and Amplification of Sub-Picosecond Pulses using a Frequency-Doubled Neodymium YAG Pumping Source," Opt. Commun. 39, 259 (1981).

17. T. Sizer II, J.D. Kafka, I.N. Duling III, C.W. Gabel, and G. Mourou, "Synchronous Amplification of Subpicosecond Pulses, IEEE J. Quantum Electron. QE-19, 506 (1983).

18. E.B. Treacy, "Optical Pulse Compression with Diffraction Gratings," IEEE J. Quantum Electron. QE-5, 454 (1969).

19. C.V. Shank, R. Yen, and C. Hirlimann, "Time-Resolved Reflectivity Measurements of Femtosecond-Optical-Pulse-Induced Phase Transitions in Silicon," Phys. Rev. Lett. 50, 454 (1983).

20. C.V. Shank, R. Yen, and C. Hirlimann, "Femtosecond-Time-Resolved Surface Structural Dynamics of Optically Excited Silicon," Phys. Rev. Lett. 51, 900 (1983).

21. R.L. Fork, C.V. Shank, C. Hirlimann, R. Yen, and W.J. Tomlinson, "Femtosecond White-light Continuum Pulses," Opt. Lett. 8, 1 (1983).

22. A. Seilmeier, K. Spanner, A. Laubereau, and W. Kaiser, "Narrow-Band Infrared Pulses with Sub-Picosecond Time Resolution," Opt. Commun. 24, 237 (1978).

23. F. Wondrazek, A. Seilmeier, and W. Kaiser, "Picosecond Light-Pulses Tunable from the Violet to the Near Infrared," Appl. Phys. B 32, 39 (1983).

CHAPTER 3

TRANSIENT PARAMETRIC FOUR WAVE MIXING

3.1 INTRODUCTION

Transient four wave mixing by parametric scattering has been shown to be a promising technique for studies of coherent transient behavior (1-4). Related transient third order nonlinear optical effects have been employed for phase conjugate optical gating (5,6) and are also commonly observed as a coherent coupling term in pump-probe experiments (7-10). The development of the CPM ring dye laser and dye amplifier makes possible the investigation of these phenomena on a femtosecond time scale.

In this chapter we describe the application of the femtosecond dye amplifier to experimental studies of transient parametric four wave mixing. Special emphasis is placed on the analysis and measurement of parametric scattered pulse durations and their relationship to the transient properties of the four wave mixing process and the nonlinear material. This is relevant not only to the measurement of material time constants such as population relaxation and dephasing times, but also to the application of transient four wave mixing for optical gating. While previous investigators have examined parametric scattering as an approach to measuring material time constants (1-4), this is, to our knowledge, the first investigation which considers actual transient pulse durations. A summary of the experimental results described in this chapter is published in (11).

In addition to the experimental investigation of transient parametric scattering, theoretical studies were conducted. This research was performed in collaboration with Dr. Ting K. Yee from Lincoln Laboratories,

Calculations were performed using diagrammatic density matrix perturbation theory to investigate scattered parametric pulse durations and energies, relating them to material population and dephasing lifetimes as well as incident pulse shape. This investigation is described in detail in Appendix A.

3.2 PHYSICAL MODEL FOR TRANSIENT PARAMETRIC SCATTERING

For the purpose of interpreting our experimental measurements, let us begin by constructing a simple physical model for transient parametric scattering. Figure 3.1 illustrates a schematic diagram of the parametric scattering four wave mixing geometry. Two intense laser pulses with fields E_1, E_2 and wavevectors k_1,k_2 are directed into a thin nonlinear sample in a copropagating nearly collinear geometry. A variety of nonlinear effects are produced in the material. Some of these processes induce changes in absorption and coupling between the pulses in the k_1 and k_2 directions, giving rise to pump-probe and coherent coupling effects. Other processes produce a scattering of the incident fields in the $2k_1-k_2$ and $2k_2-k_1$ parametric directions. Our objective is to predict the transient behavior of the parametric signal as a function of the temporal delay ΔT between the incident pulses.

The incident fields E_1 and E_2 induce a polarization response in the media. If the pulses are coherently overlapping, these polarizations will interfere with a spatial periodicity of k_1-k_2. This periodic excitation in turn induces a periodic population change in the nonlinear media which functions like a transmission diffraction grating to scatter the incident fields into the parametric directions. This effect is also responsible for coherent coupling in pump-probe experiments.

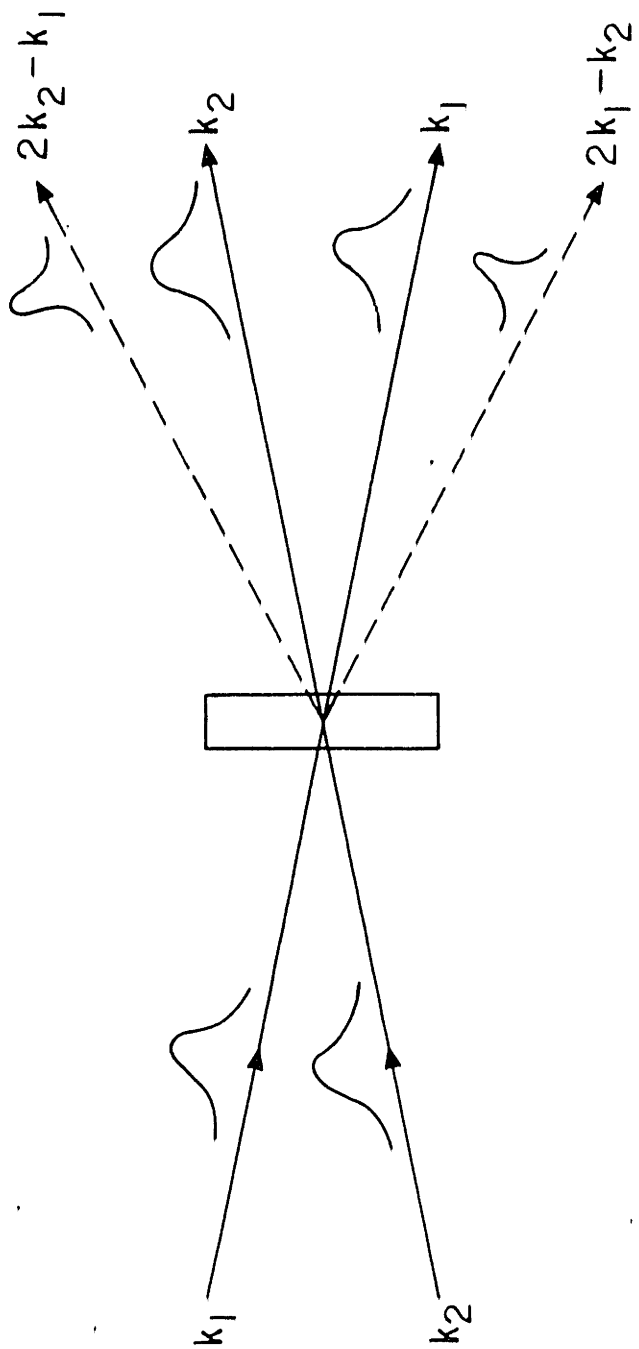

Figure 3.1 Parametric scattering four wave mixing geometry.

Consider this process in the simplest limits where the laser pulsewidth t_p is long compared to the material dephasing time T_2 but short compared to the population relaxation time T_1. In this case the polarization response of the material will instantaneously follow the incident fields while the induced population will be long lasting. The transient temporal behavior of the parametric scattering process can be described as shown in Figure 3.2. Assume the incident fields have pulse envelopes $E_1(t)$ and $E_2(t+\Delta t)$ and are separated by a variable time delay ΔT. Then the spatially periodic induced population grating will be given by the time integral of $E_1(t)E_2^*(t+\Delta T)$. This population grating acts as a transient optical gate which scatters the incident pulses. Varying the time delay ΔT between E_1 and E_2 will change the time at which the gating occurs and will, in general, also change the risetime of the gating. It is important to note that the amplitude of the induced population is determined by the temporal overlap of the fields $E_1(t)$ and $E_2(t+\Delta T)$. Thus parametric scattering four wave mixing is only observed when the incident pulses are coherently overlapping.

Using this simple physical model, the third order polarization for the parametric four wave mixing signal in the $2k_1-k_2$ direction is given by:

$$(3.1) \qquad P^{(3)}(t,\Delta T) \sim E_1(t) \int_{-\infty}^{t} E_1(t')E_2(t'+\Delta T)dt'$$

The expression for the signal in the conjugate $2k_2-k_1$ direction is obtained by interchanging E_1 and E_2^*. As discussed in Appendix A, this result is equivalent to that derived using a conventional density matrix perturbation theory analysis in the limit of $T_2 \ll t_p \ll T_1$. Note, however,

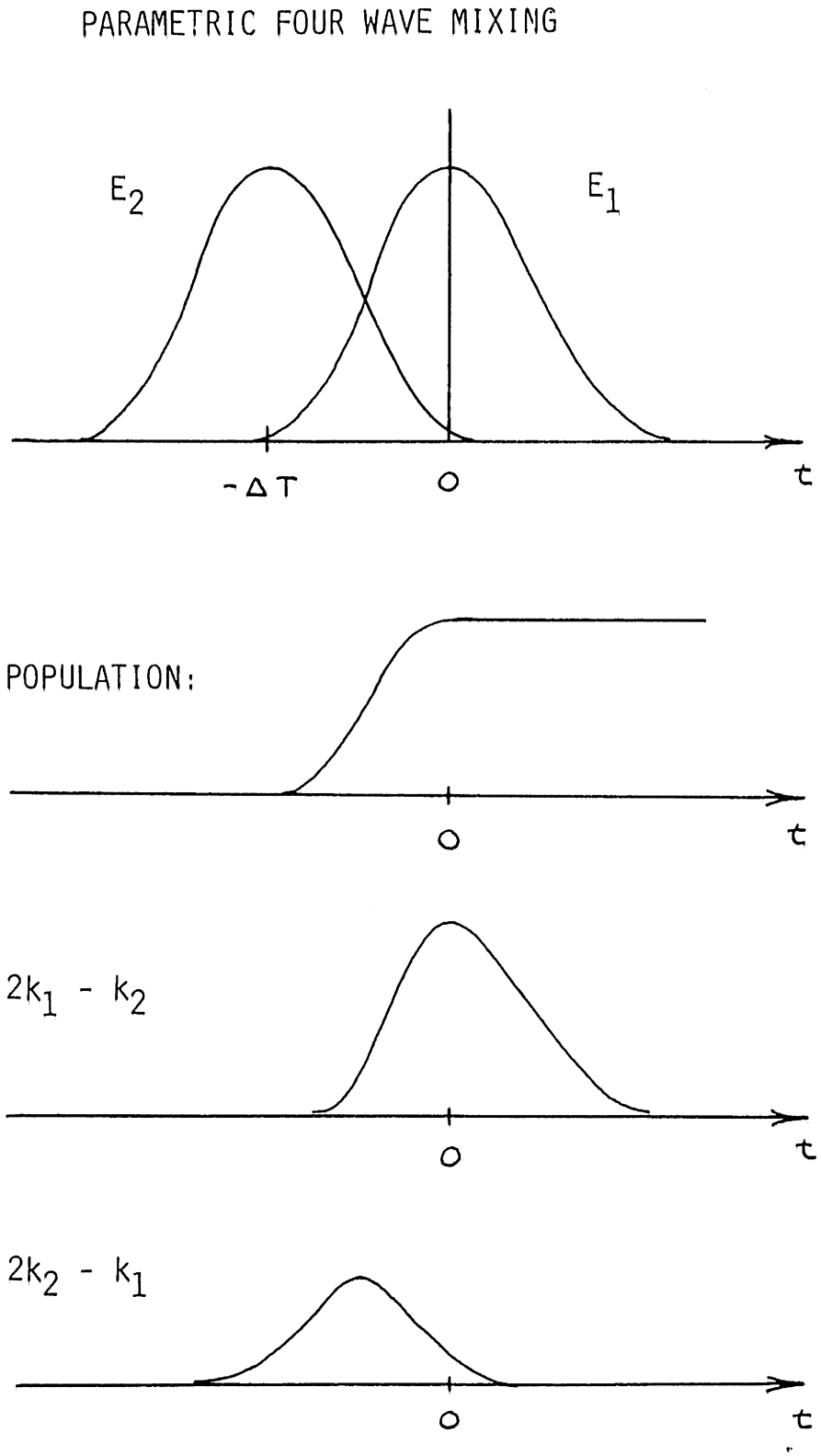

Figure 3.2 Simple physical model of parametric scattering.

that this model assumes a thin nonlinear material and neglects effects of field propagation and phase matching. In addition, it is assumed that higher order processes such as saturation and multiple scattering are negligible.

Equation 3.1 may be numerically integrated to describe the transient behavior of the parametric signal for arbitrary incident pulse separations and pulse shapes. Figure 3.3 shows the FWHM pulse duration of the parametric signal intensity $I \sim [P^{(3)}(t,\Delta T)]^2$ as a function of incident pulse separation ΔT assuming unit FWHM gaussian and sech incident pulses. The pulse shortening of the parametric pulse results from the transient optical gating effect of the induced population grating. Note that the parametric pulse duration has a strong functional behavior on both incident pulse separation ΔT as well as pulse shape.

The total energy of the parametric signal is a function of the incident pulse separation and is described by:

$$(3.2) \qquad \varepsilon(\Delta T) \sim \int_{-\infty}^{\infty} [P^{(3)}(t,\Delta T)]^2 dt$$

Figure 3.4 illustrates the parametric signal energy as a function of ΔT assuming gaussian and sech incident pulse shapes. Note the asymmetry and peak shift of $\varepsilon(\Delta T)$. Using a density matrix analysis of parametric four wave mixing including T_1 and T_2 relaxation effects, previous investigators (1,2) have shown that a careful measurement of this asymmetry and peak shift may be employed to determine an upper bound on T_2. In our experiment we focus instead upon the pulse duration of the transient parametric signal. In this context, $\varepsilon(\Delta T)$ presents practical limitations on the accurate measurement of parametric pulse widths for large positive or

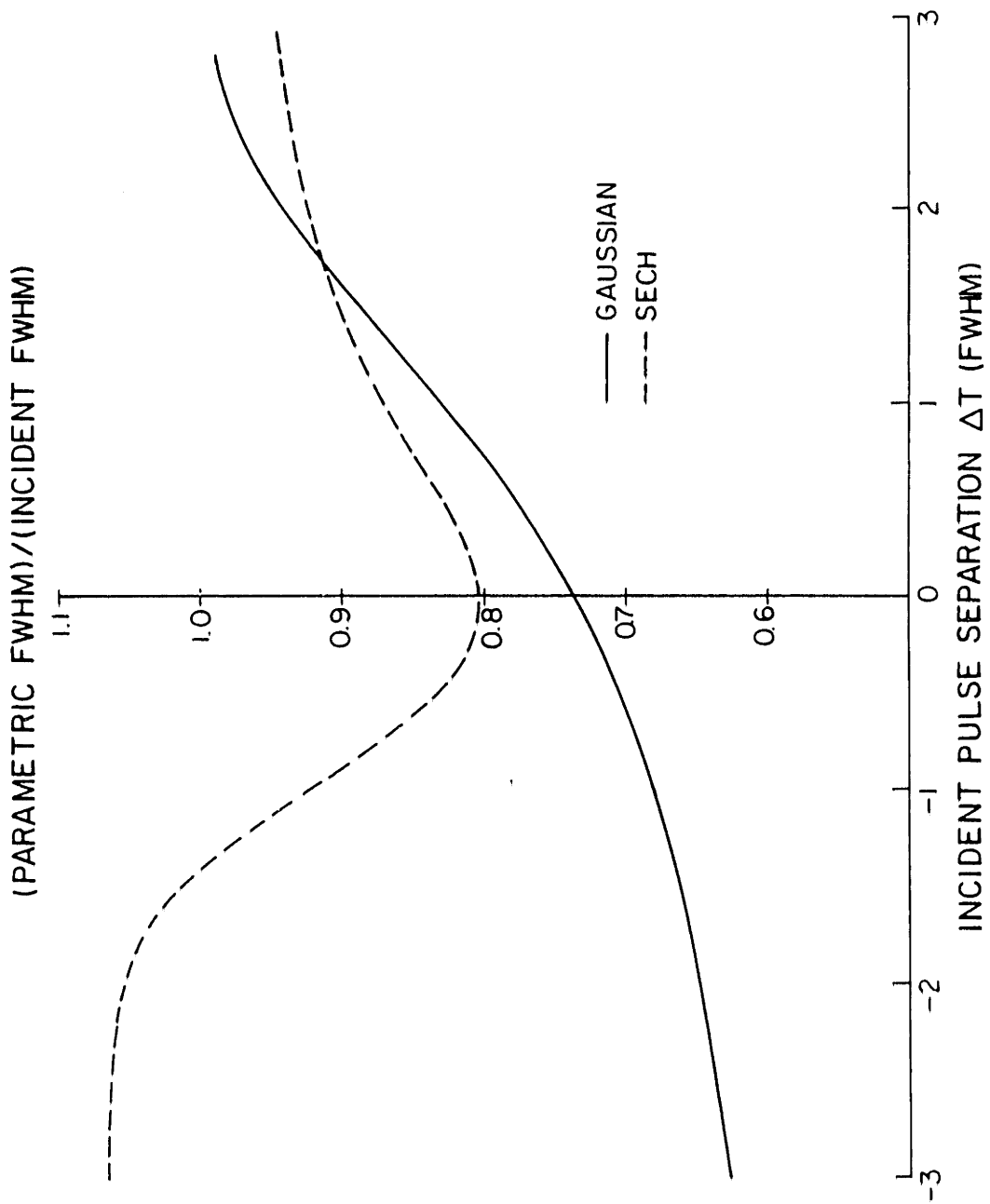

Figure 3.3 Theoretically predicted parametric pulse duration vs. incident pulse separation.

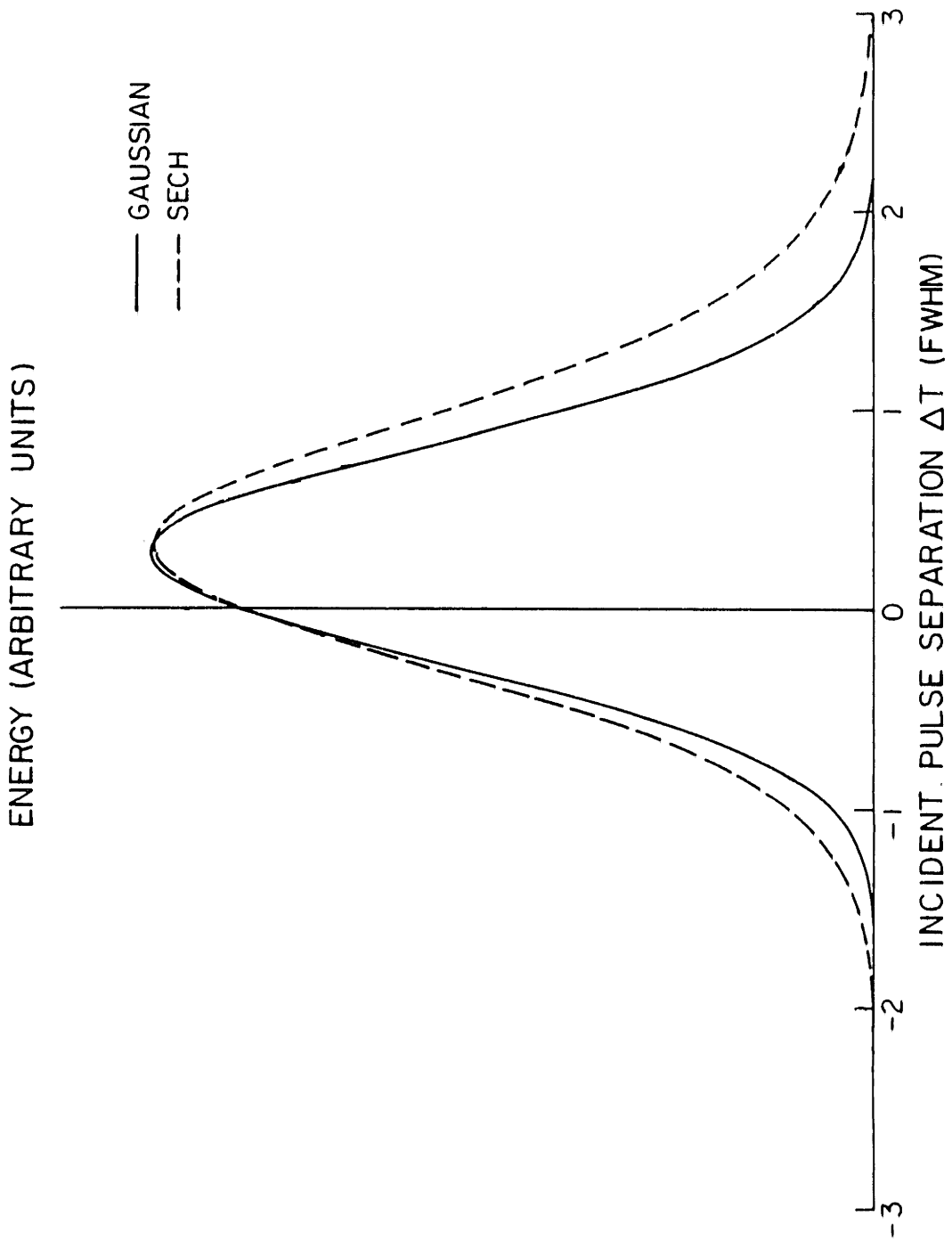

Figure 3.4 Theoretically predicted parametric pulse energy vs. incident pulse separation.

negative values of ΔT where the scattered energies are small.

3.3 EXPERIMENTAL DESCRIPTION

The ring dye laser and four stage dye amplifier produced pulses as short as 75 fs with energies of 400 microjoules. However, for the purposes of this experiment it was desirable to compromise pulse energy to obtain shorter pulses. Using only three stages of amplification followed by spatial filtering and grating pair compression, it was possible to achieve 65 fs pulses with 50 μJ energy.

A beamsplitter and conventional mechanical delay geometry was used to produce two spatially separated beams with pulses of equal energy. The time delay between the pulses was adjusted by a computer controlled 1 micron step size mechanical stage. The pulses were then focussed into a thin 0.1 mm path length cell containing 5×10^{-4} M Malachite green in methanol. The two incident beams were copropagating, crossing with an angle of $\sim 1.5^{o}$ to insure phase matching and reduce geometric time resolution limiting effects.

The parametrically scattered beams were clearly visible to the unaided eye and could be measured without difficulty. The integrated intensity or energy of the parametric signal was detected by a Si photodiode and averaged over several laser pulses to eliminate shot to shot energy fluctuations in the amplifier. The incident pulse separation was controlled by a computer and data were averaged over successive scans of the optical delay to suppress any long term fluctuations. Acceptable signal to noise ratios were obtained by averaging 5 laser shots per data point over 2 to 4 successive scans of the delay.

Figure 3.5 shows the parametric signal energy versus incident pulse separation ΔT. The delay axis is calibrated in units of FWHM based upon an autocorrelation measurement of the incident pulse duration assuming gaussian pulse shape. The zero of delay was determined by measuring both $2k_1-k_2$ and $2k_2-k_1$ parametric signals as a function of ΔT and noting that their traces are mirror symmetric about $\Delta T = 0$. The maximum observed efficiency of the parametric mixing process was approximately 3%; however, no attempts to improve phase matching or optimize dye concentration were made.

The pulse duration of the parametric signal was measured by collinear second harmonic generation autocorrelation in a 0.3 mm thick angle phase matched KDP crystal using a Michelson type delay line. Optical delay was adjusted by a computer controlled 0.1 micron resolution mechanical stepping motor stage. In order to reduce the effects of parametric pulse energy fluctuations, a portion of the parametric signal was detected by a photodiode which functioned as a reference. The computer monitored this reference signal and discriminated against excessive pulse energy fluctuations.

Because of the short pulse duration and high intensity of the parametric pulses, collinear autocorrelation was chosen over the crossed beam, background free geometry. A crossed beam autocorrelation would require careful control of focussing parameters at the KDP crystal in order to avoid time resolution limiting geometric arrival time effects which occur from the finite spot size and crossing angle between the beams. Conversely, in the collinear geometry, these resolution limiting effects could be precisely controlled by misaligning the two beams by a given number of fringes while using an arbitrarily large spot size.

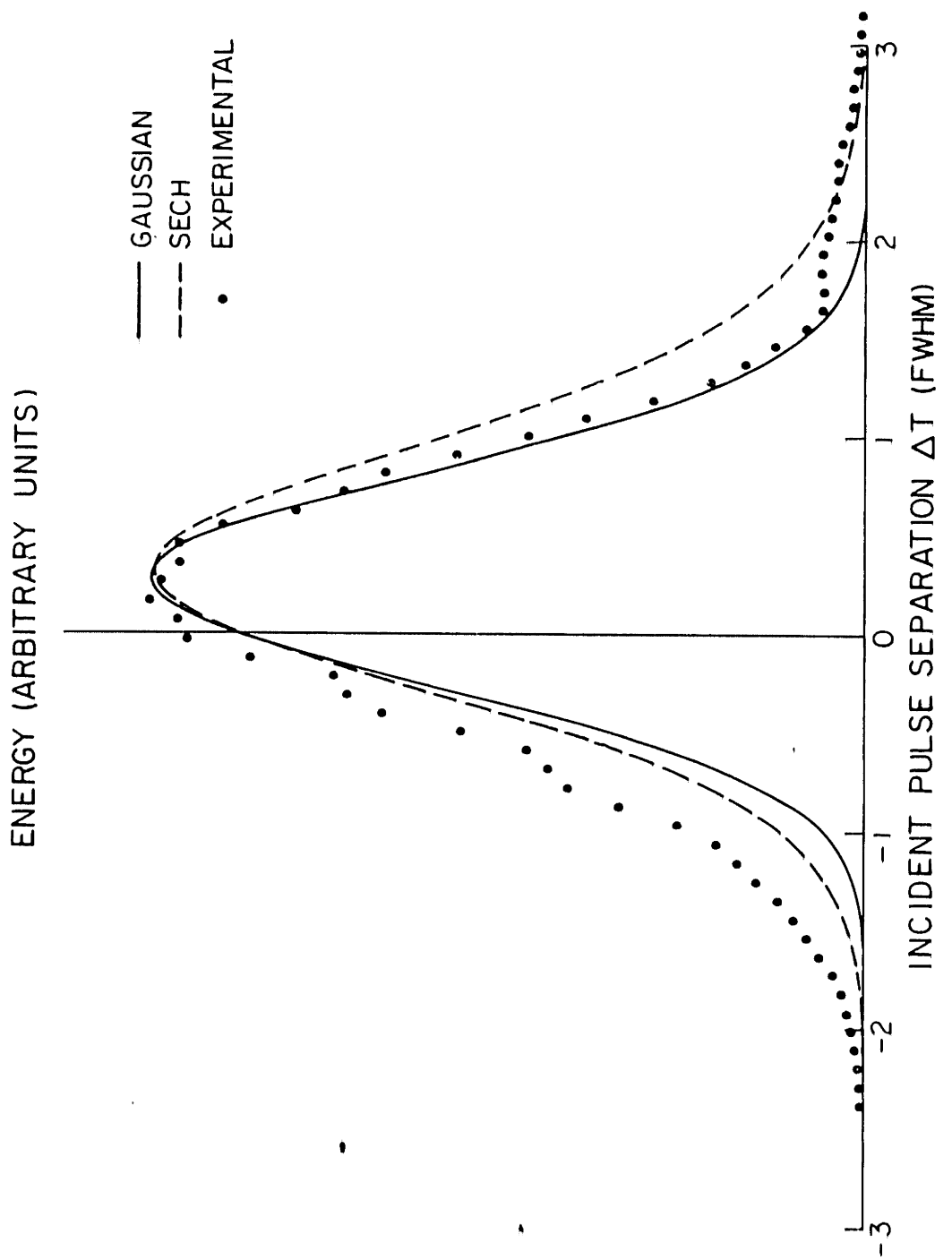

Figure 3.5 Experimentally measured parametric pulse energy vs. incident pulse separation.

Figure 3.6 illustrates the parametric pulse duration data presented as the ratio of the parametric autocorrelation FWHM to incident pulse autocorrelation for several values of incident pulse separation ΔT. The ΔT axis is normalized identically to that of Figure 3.5. A maximum pulse shortening of $\sim$0.54 was obtained for a delay of $\Delta T = 1.8$. Figure 3.7 shows autocorrelation traces of the input and parametric pulses demonstrating the generation of $\sim$37 fs ($\sim$40 fs) parametric pulses from $\sim$68 fs ($\sim$75 fs) input pulses assuming sech (gaussian) pulse shape.

3.4 DISCUSSION

Figures 3.5 and 3.6 summarize the experimental measurements of parametric pulse duration and energy. Before comparing these results to theoretical predictions, it is important to note that the autocorrelations do not directly determine the duration of the pulse intensity without knowledge of the pulse shape. More specifically, this technique does not measure possible pulse shape asymmetry which is in fact theoretically predicted by our model of equation 3.1. In spite of the limitation, however, we believe that the measured autocorrelation FWHM correctly represents the general functional form of the parametric pulse duration with varying incident pulse separation ΔT. Assuming the worst case of gaussian pulses, the measured pulse durations should also correctly indicate an upper bound on the actual pulse durations.

The results of Figure 3.6 demonstrate that the parametric pulse durations have a strong functional dependence on the incident pulse separation, in agreement with our simple model predictions. The functional form of the pulse duration variation further suggests that the incident pulse shape is more closely gaussian than sech. For this reason, we have chosen

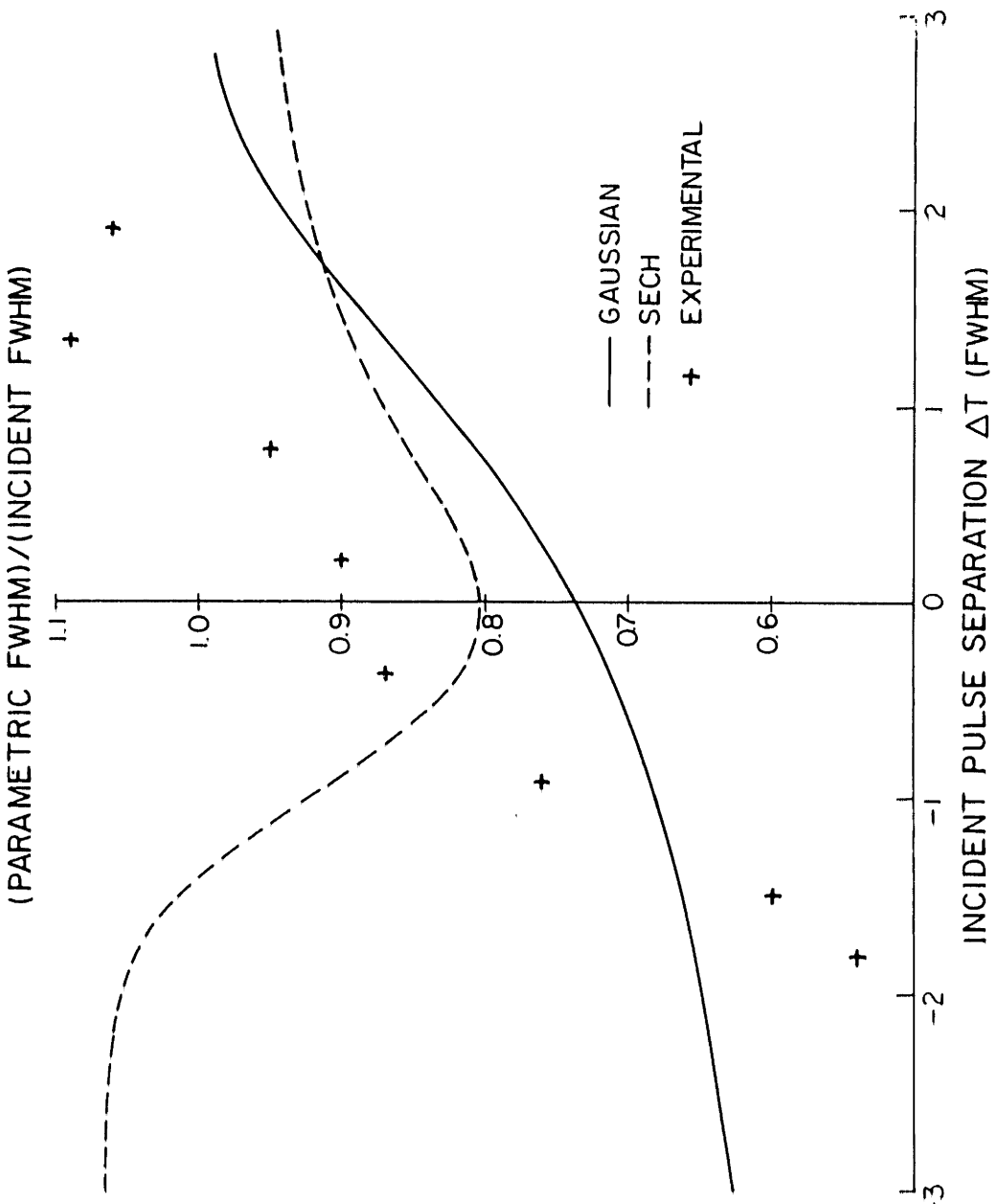

Figure 3.6 Experimentally measured parametric pulse duration vs. incident pulse separation.

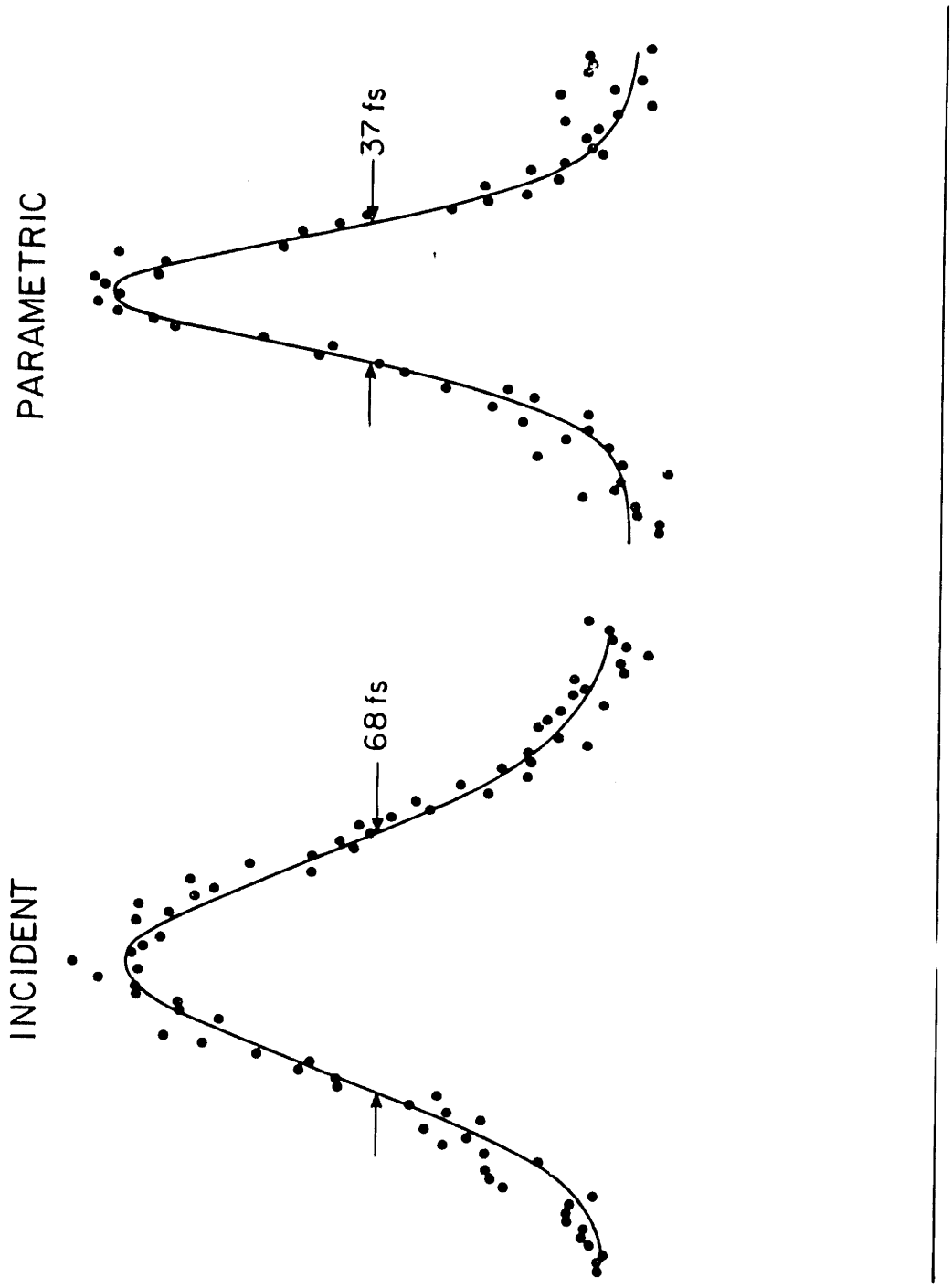

Figure 3.7 Autocorrelation traces of incident and parametrically scattered pulses showing optimum pulse shortening.

to normalize the ΔT axis of Figures 3.5 and 3.6 to the incident pulse duration assuming gaussian pulses. The rapid decrease in the parametric pulse width for $\Delta T<0$ and the fact that the ultimate pulse width is less than predicted by the simple theoretical model may indicate possible pulse shape asymmetry.

Figure 3.5 illustrates the measurements of integrated parametric signal intensity. Results are comparable to the theoretically predicted $\varepsilon(\Delta T)$ for both gaussian and sech incident pulse shapes. In particular the observed peak shift is in close agreement with the theoretical model. It is important to note, however, that the predicted parametric signal energies show a similar behavior for both gaussian and sech incident pulses. In fact, determination of material time constants or pulse shape using total scattered energy alone requires sensitive measurements taken over a large dynamic range (see Appendix A). In contrast, the measurement of the actual transient properties of the parametric signal, such as pulse width, provides a much more sensitive indicator of material time constants and pulse shape. In particular, we point out that the observation of parametric pulses of less than 40 fs duration as shown in Figure 3.7 provides direct evidence that the T_2 time in Malachite green is substantially less than 40 fs.

From an applied viewpoint, this investigation is interesting because it demonstrates the viability of parametric transient four wave mixing as a technique for optical gating and shortening of high power femtosecond pulses. The response time of this process is restricted in principle only by the bandwidth or T_2 time of the nonlinear material and geometric effects arising from finite spot size and beam crossing angle at the sample. Thus the technique can, in principle, be extended to function with even

shorter pulses. This approach may be compared to pulse compression by self phase modulation in optical fibers which yields superior compression but is restricted to lower powers (12). Because of its high power capability, parametric transient four wave mixing can be more easily implemented as an experimental source of high power femtosecond pulses. A further possible application of this technique might be to provide a high degree of isolation between pulse source and subsequent experimental stages in, for example, a multiple stage amplifier.

3.5 SUMMARY

This chapter has described the experimental investigation of transient parametric four wave mixing in the femtosecond regime. Measurements of parametric signal pulse duration were shown to be potentially useful as a sensitive indicator of material time constants and pulse shapes. To our knowledge, this experiment is one of the first attempts to characterize the actual transient time behavior of four wave mixing processes in the femtosecond regime. Finally, our results demonstrate the viability of transient parametric mixing as a technique for high power femtosecond pulse shortening. We believe that transient studies of this type will provide important insight into ultrafast processes in condensed matter. Additional investigations in solid state materials should be of particular interest for future nonlinear optical device applications.

REFERENCES

1. T. Yajima and Y. Tiara, "Spatial Optical Parametric Coupling of Picosecond Light Pulses and Transverse Relaxation Effect in Resonant Media," J. Phys. Soc. Japan 47, 1620 (1979).

2. T. Yajima, Y. Ishida, and Y. Tiara, "Investigation of Subpicosecond Dephasing Processes by Transient Spatial Parametric Effect in Resonant Media," in Picosecond Phenomena II, R.M. Hochstrasser, W. Kaiser, and C.V. Shank, eds. Springer-Verlag, New York, 1980, p. 190.

3. A.L. Smirl, T.F. Boggess, B.S. Wherrett, G.P. Perryman, and A. Miller, "Picosecond Optically Induced Anisotropic State Filling in Semiconductors," Phys. Rev. Lett. 49, 933 (1982).

4. A.L. Smirl, T.F. Boggess, B.S. Wherrett, G.P. Perryman, and A. Miller, "Picosecond Transient Orientational and Concentration Gratings in Germanium," IEEE J. Quantum Electron. QE 19, 690 (1983).

5. D.M. Bloom, C.V. Shank, R.L. Fork, and O. Teschke, "Sub-Picosecond Optical Gating by Optical Wavefront Conjugation," in Picosecond Phenomena, C.V. Shank, E.P. Ippen, and S.L. Shapiro, eds., Springer-Verlag, New York, 1978, p. 96.

6. J.O Tocho, W. Sibbett, and D.J. Bradley, "Picosecond Phase-Conjugation Reflection and Gain in Saturable Absorbers by Degenerate Four-Wave Mixing," In Picosecond Phenomena II, R. Hochstrasser, W. Kaiser, and C.V. Shank, eds., Springer-Verlag, New York, 1980, p. 372.

7. E.P. Ippen and C.V. Shank, in Ultrashort Light Pulses, S.L. Shapiro, ed., Springer-Verlag, New York, 1977, p. 83.

8. A. Von Jena and H.E. Lessing, "Coherent Coupling Effects in Picosecond Absorption Experiments, "Appl. Phys. 19, 131 (1979).

9. Z. Vardeny and J. Tauc, "Picosecond Coherence Coupling in the Pump and Probe Technique," Opt. Commun. 39, 396 (1981).

10. B.S. Wherrett, A.L. Smirl, and T.F. Boggess, "Theory of Degenerate Four-Wave Mixing in Picosecond Excitation-Probe Experiments," IEEE J. Quantum Electron. QE-19, 680 (1983).

11. J.G. Fujimoto and E.P. Ippen, "Transient Four-Wave Mixing and Optical Pulse Compression in the Femtosecond Regime," Opt. Lett. 8, 446 (1983).

12. C.V. Shank, R.L. Fork, R. Yen, and R.H. Stolen, "Compression of Femtosecond Optical Pulses," Appl. Phys. Lett. 40, 761 (1982).

CHAPTER 4

GENERATION AND MEASUREMENT OF OPTICAL PULSES AS SHORT AS 16 FEMTOSECONDS

4.1 INTRODUCTION

The use of nonlinear optical fiber techniques for the generation of femtosecond optical pulses is perhaps one of the most promising and active areas of current femtosecond research (1-8). In particular, the use of nonlinear self phase modulation in optical fibers has emerged as a valuable and powerful technique for the compression of picosecond pulses into the femtosecond regime (4-8). Using a two stage fiber compression technique, Nikolaus and Grischkowsky (7) have recently demonstrated pulse compression factors as high as 65x to produce tunable 90 femtosecond pulses by compressing the output of a synchronously modelocked dye laser. Pulses as short as 30 femtoseconds have been generated by Shank et al (8) by compressing femtosecond pulses from a CPM ring dye laser and amplifier.

In this chapter we describe an extension of these fiber compression techniques to generate pulses as short as 16 femtoseconds. These pulses consist of only eight optical cycles and are the shortest optical pulses generated to date. Pulse duration measurements were obtained with noncollinear second harmonic generation autocorrelation in a thin KDP crystal. Careful attention and special experimental techniques were required for the generation and measurement of these extremely short pulse durations. This research was performed in close collaboration with a fellow graduate student, Mr. Andrew Weiner. A summary of this investigation is scheduled for publication in (9).

4.2 DISPERSION AND ULTRASHORT PULSES

When a short pulse propagates through a material with dispersion, it develops a time dependent phase which results in a frequency chirp. For a normally dispersive media, this chirp is negative and the high frequency components of the pulse are retarded with respect to the low frequency components. This is manifest as a broadening of the temporal pulse duration. For gaussian pulses of the form $I(t) = \exp(-4t^2 \ln 2/T^2)$ with a FWHM of T, the dispersively broadened pulse width is given by (10,11):

$$T' = T[1 + (T_c/T)^4]^{1/2} \tag{4.1}$$

$$T_c = 2[\ddot{\beta} z \ln 2]^{1/2} = 2\left[\frac{\lambda^3}{2\pi c^2}\frac{d^2n}{d\lambda^2} z \ln 2\right]^{1/2} \tag{4.2}$$

T_c is defined to be the critical pulse width, where z is the propagation distance. The broadened pulse width is a nonlinear function of the dispersion and propagation distance. For pulse durations comparable to or less than the critical pulse width, significant dispersive broadening occurs.

For most optical materials and typical propagation lengths, the critical pulse width is less than 100 femtoseconds (see Table 4.1). Thus the effects of dispersive broadening on pulses from the CPM ring dye laser or amplifier are usually negligible. However, with the generation of yet shorter pulse durations, these dispersive effects become extremely significant. Fortunately, the effects of normal dispersion can be compensated for by simply introducing a comparable source of anomalous dispersion. Dispersively broadened pulses can be recompressed and their original pulse durations recovered by propagating through a given length of anomalously

T_c CRITICAL PULSEWIDTHS FOR DISPERSION		
LENGTH	T_c BK7 GLASS	T_c KDP
100 μm	4.1 fs	5.4 fs
500 μm	9.3 fs	12 fs
1 mm	13 fs	17 fs
1 cm	41 fs	54 fs
10 cm	130 fs	-

Table 4.1 Critical pulsewidths for BK7 glass and KDP

dispersive material to introduce a positive frequency chirp which cancels the effects of the negative chirp produced by normal dispersion.

This type of pulse recompression has been demonstrated by using the anomalous dispersion of a resonant absorption line in Na vapor (12) as well as exciton absorption in CdSe (13). However, the most practical approach is to employ a pair of diffraction gratings to produce a frequency dependent phase shift (14). The diffraction gratings are used in a parallel configuration as shown in Figure 4.1. There is no angular separation of wavelengths since the angular diffraction of one grating is cancelled by the other. The anomalous dispersion arises from the fact that different frequency components of the pulse follow a different optical path with high frequencies being advanced with respect to low frequencies. The anomalous dispersion produced by this type of grating pair is equivalent to that produced by a dispersive media with $d^2\beta/d\omega^2$ given by:

$$\ddot{\beta}z = -d\lambda^3/2\pi c^2\Lambda^2[1 - (\sin\theta_i - \lambda/\Lambda)^2] \tag{4.3}$$

where β is the propagation constant, d is the slant distance between the gratings, θ_i the incident beam angle with respect to the grating normal, and Λ the grating periodicity (11,14). Note that the amount of anomalous dispersion can easily be adjusted by varying the grating separation. Thus in laboratory applications the effects of dispersive pulse broadening can be compensated by empirically adjusting the gratings to produce the shortest measured pulse durations. In addition, any dispersive elements in the experimental apparatus may be precompensated for in this manner.

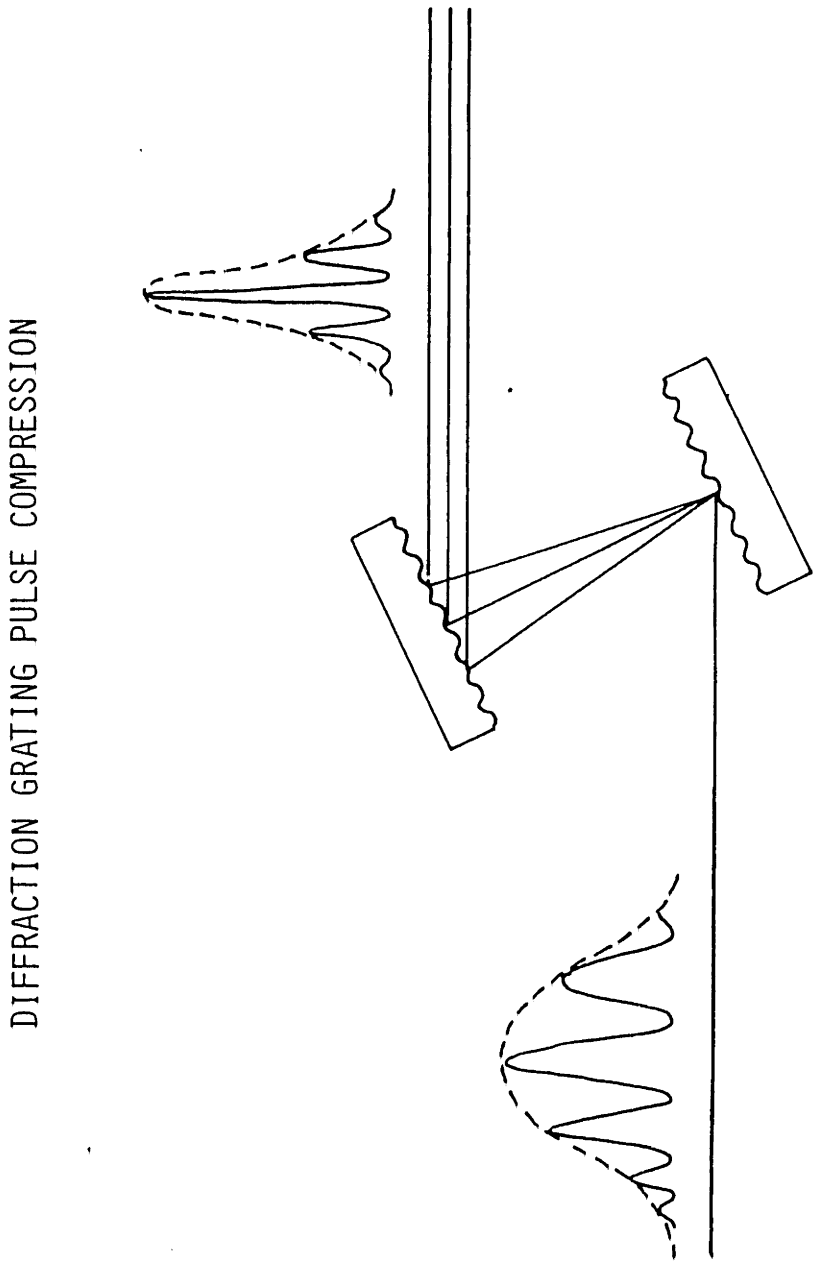

Figure 4.1 Recompression of dispersively broadened pulse using diffraction grating pair.

4.3 SELF PHASE MODULATION AND PULSE COMPRESSION IN OPTICAL FIBERS

While diffraction grating recompression may be employed to compensate for dispersive pulse broadening, of course, it cannot produce compression of unchirped pulses. In order to produce a true pulse compression, it is necessary to increase the spectral bandwidth of the pulse. This must be done using a nonlinear optical process. While a linear process can be used for signal filtering, the generation of additional frequencies requires the use of nonlinearities. Further, the nonlinear process must generate the required frequency bandwidth in such a way that the frequencies are produced with the appropriate phase so that the temporal profile of the pulse may be compressed either directly or through the use of suitable filtering. The use of nonlinear self phase modulation and dispersive compensation is well suited for this application (15,16).

Self phase modulation occurs when an intense optical pulse propagates through a material which has an intensity dependent index of refraction. If the nonlinearity is electronic and has a rapid relaxation time, the change in index is $\delta n = \frac{1}{2} n_2 E^2$. The pulse envelope will thus produce an intensity dependent phase shift which modulates the frequency of the optical pulse. With an effective interaction length of L, this gives rise to a frequency shift of $\delta\omega(t) = -(2\pi L/\lambda) d\delta n/dt$ which is proportional to $-dI/dt$. Figure 4.2 shows a schematic diagram of the self phase modulation produced by a pulse. The leading edge of the pulse produces a frequency downshift while the trailing edge produces a frequency upshift. The frequency sweep produced near the center of the pulse is approximately linear. This frequency chirp is similar to that produced by normal dispersion and the pulse may thus be compressed by the use of a diffraction grating pair. The effectiveness of this compression is determined by the amount of pulse

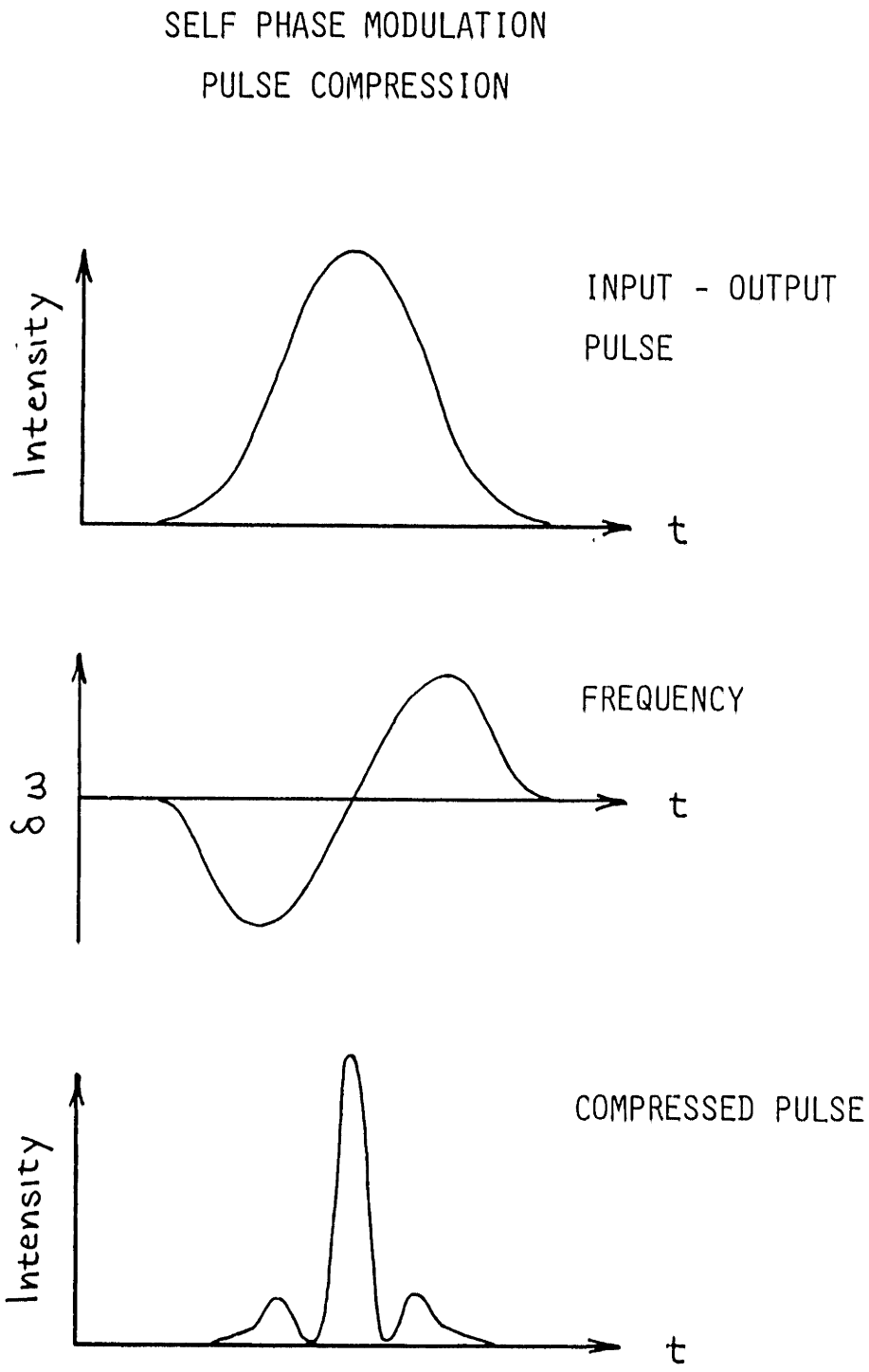

Figure 4.2 Self phase modulation pulse compression.

energy contained in the linearly swept portion of the frequency chirp. The other frequency components from the leading and trailing edges of the pulse give rise to side lobes or wings on the compressed pulse.

The use of self phase modulation for pulse compression had in fact been proposed over a decade ago by Fisher et al (16). However, the application of this process in a liquid or solid bulk nonlinear material was intractable because of other nonlinear effects such as self focussing and filamentation which distorted the spatial profile of the self phase modulated pulses and prevented effective pulse recompression. Thus the successful realization of this approach required the use of single mode optical fibers (17). Optical fibers not only provided the desired control of the spatial mode but also confined the field at high intensities over long propagation distances.

The use of optical fibers introduces an additional complication because of the fact that self phase modulation and dispersive pulse broadening may take place simultaneously. Thus these effects give rise to a constantly evolving field envelope and phase as the pulse propagates. Assuming a field of the form $E(z,t) = E(t)\cos(k_0 z - \omega_0 t - \phi)$, the propagation is described by the following set of coupled nonlinear differential equations for the envelope and phase:

$$\frac{\partial E}{\partial z} + k_1 \frac{\partial E}{\partial t} = -\tfrac{1}{2}k_2\left(2\frac{\partial \phi}{\partial t}\frac{\partial E}{\partial t} + E\frac{\partial^2 \phi}{\partial t^2}\right) \tag{4.4}$$

$$\frac{\partial \phi}{\partial z} + k_1 \frac{\partial \phi}{\partial t} = \tfrac{1}{2}k_2\left(\frac{1}{E}\frac{\partial^2 E}{\partial t^2} - \left(\frac{\partial \phi}{\partial t}\right)^2\right) - \kappa E^2 \tag{4.5}$$

Where $k_1 = \delta k/\delta\omega = 1/v_g$ is the reciprocal group velocity, $k_2 = \delta^2 k/\delta\omega^2$ is the dispersion, and $\kappa = 0.5\, k_0 n_2/n_0$ describes the self phase modulation

(4,5,18). With the substitution $u = E\exp(i\phi)$, these equations reduce to the nonlinear Schrodinger equation:

$$(4.6) \qquad i\left(\frac{\partial u}{\partial z} + k_1 \frac{\partial u}{\partial t}\right) = -\tfrac{1}{2}k_2 \frac{\partial^2 u}{\partial t^2} + \kappa|u|^2 u$$

For pulse wavelengths in the anomalous dispersion regime, this equation describes the formation and propagation of solitons (1,2). In general a solution of this equation requires the use of numerical techniques.

Solutions describing the propagation of pulses with simultaneous dispersion and self phase modulation (DSPM dispersive self phase modulation) predict that under certain conditions, enhanced pulse compression can be produced (5,18). This arises because the combined effects of dispersion and self phase modulation cause the pulse to develop a more linear frequency chirp over its duration with more of the pulse energy being contained in the chirped portion of the pulse. Thus recompression of the spectrally broadened pulse with a diffraction grating pair yields lower temporal sidelobes or wings than would occur with self phase modulation alone. This process is shown schematically in Figure 4.3. Although an analytical description of dispersive self phase modulation pulse compression is quite complicated, fortunately the compressed pulse durations are not especially critical functions of the pulse intensity or fiber length. Thus an empirical experimental optimization of the compression process is possible.

4.4 EXPERIMENTAL DESCRIPTION AND DISCUSSION

Figure 4.4 illustrates a schematic diagram of the experimental arrangement. For our application relatively low pulse energies were

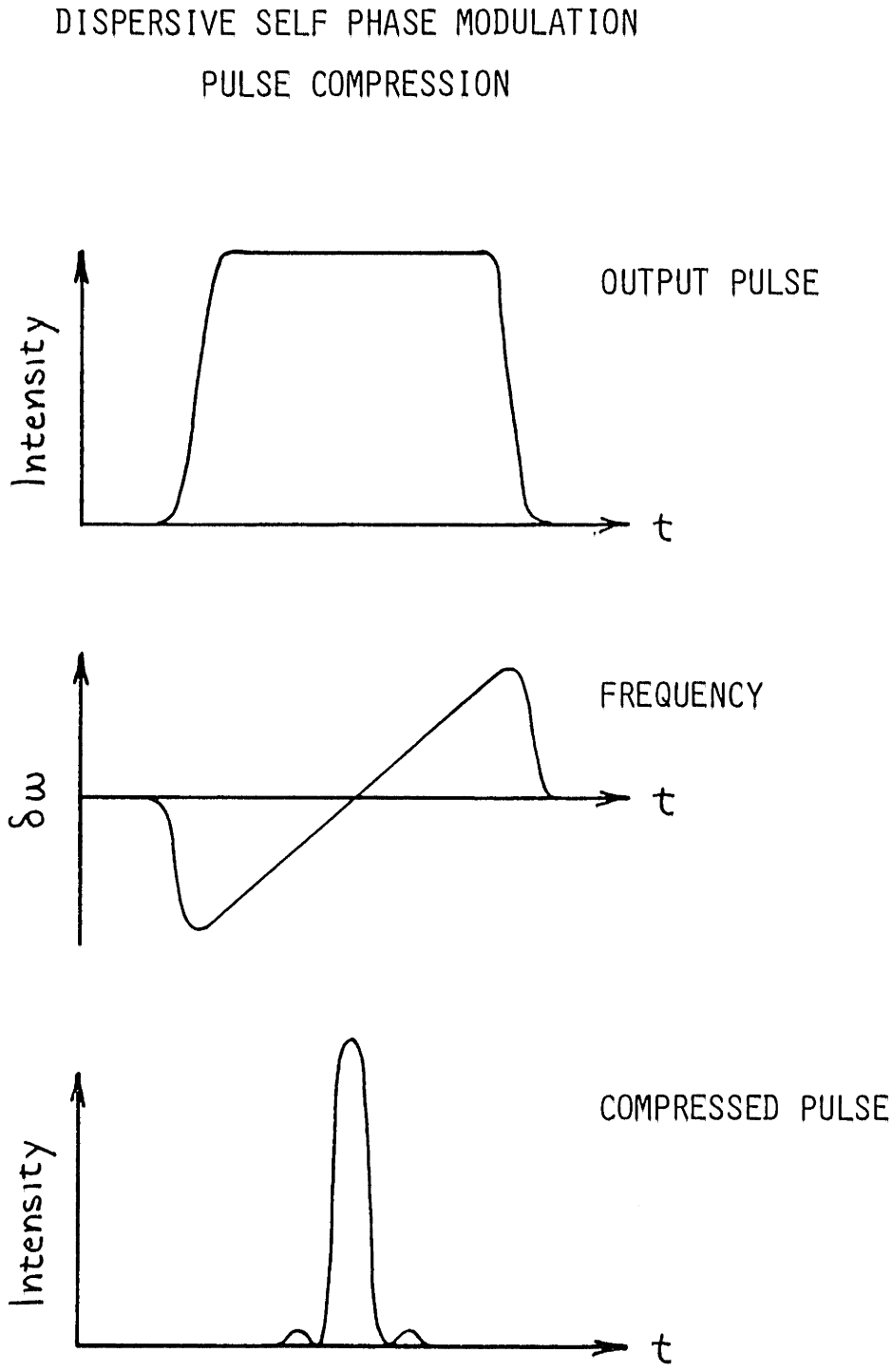

Figure 4.3 Dispersive self phase modulation pulse compression.

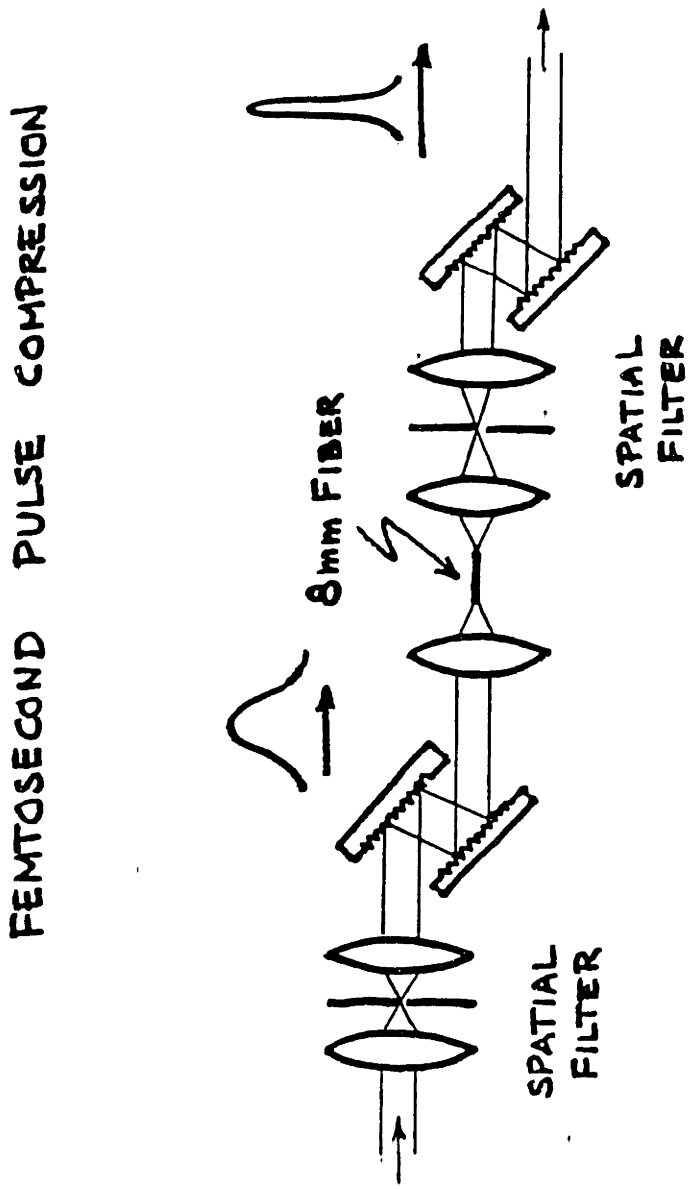

Figure 4.4 Schematic of experimental configuration for pulse compression.

required so that only the first two stages of the femtosecond dye amplifier were used. This allowed the production of shorter pulses with less spatial mode distortion than could be obtained using the entire four stages of amplification. The pulses after the first two gain stages and saturable absorbers were amplified by approximately 5×10^4 to yield single pulse energies of ~5 μJ. To improve the spatial profile, the output beam was spatially filtered by focussing through a 50 μm pinhole and then collimated to a diameter of 6 mm. This produced a near gaussian spatial mode. Dispersive broadening in the amplifier chain was compensated for after the spatial filter by a diffraction grating pair consisting of 600 l/mm gratings separated by a slant distance of about 2.5 cm. Part of the beam is directed into a reference photodiode to monitor pulse energy fluctuations. Pulse durations of 65 femtoseconds are obtained after the grating recompression.

The pulses are then coupled into a short 8 mm length of polarization preserving optical fiber (19) with a 10x microscope objective. The power coupled into the guided mode is adjusted by attenuating with neutral density filters with fine adjustment made by moving the objective in and out of focus. A HeNe alignment laser is also coupled into the fiber to facilitate alignment of the fiber and subsequent optics. Because of the low 10 Hz repetition rate of the dye amplifier, the total average intensity coupled through the fiber is very low and the beam is not easily visible. The pulses emerging from the fiber are imaged with a 40x microscope objective through a 100 μm pinhole to filter out cladding modes and yield a single mode. The beam is then recollimated to a diameter of 3 mm.

Spectral broadening produced by self phase modulation in the optical fiber is monitored with an optical multichannel analyzer. For this

experiment, about 5 nJ of pulse energy is coupled into the fiber resulting in a broadening of the input spectrum by a factor of ∿4. The change in color of the self phase modulated pulse is visibly apparent. As the input energy is increased, the spectrum broadens smoothly into a continuum. For short fibers, however, this is also close to the damage threshold.

The spectrally broadened pulses are recompressed by a pair of 600 1/mm diffraction gratings separated by a slant distance of ∿1.5 cm. Adjustment of this grating pair also pre-compensated for dispersion in the autocorrelator. Because of the relatively large spectral bandwidth of the pulses, the grating alignment was extremely critical. The parallelicity of the gratings was carefully adjusted to accuracies of less than 0.25^{o} by projecting the beams over a long distance. The relative rotation of the gratings was also extremely sensitive. Misalignments of as little as 0.5^{o} produced a visible separation of colors in the far field of the beam and a lengthening of the autocorrelation measurement.

A beam diameter of at least 3 mm on the gratings was required to avoid noticeable effects of spectral walk-off. Because of the fact that each ruling on the grating contributes an optical cycle of delay, there is a maximum compression that a grating pair can provide without spectral walk-off:

$$\Delta T << N\lambda/c \tag{4.7}$$

The maximum pulse width change ΔT is approximately limited to N optical cycles where N is the number of grating rulings that are illuminated by the beam diameter.

The compressed pulse durations were measured by noncollinear, background free, second harmonic generation (20). This was done to avoid problems associated with averaging over the nonlinear coherence fringes which occur in a collinear correlation measurement. It is important to note that the crossed beam configuration will in general introduce geometric time resolution limiting effects from the finite laser spot size and crossing angle of the beams at the second harmonic crystal. These effects must be minimized by making the angle between the beams as small as possible while focussing to a common, diffraction limited spot. For our measurements the estimated spot size was $\sim$35 μm with a beam crossing angle of $\sim 2^{\circ}$. For our 16 femtosecond pulse durations, the convolved contribution to the broadening in the autocorrelation is estimated to be less than $\sim$1 fs. However, it is essential that the beams have a near gaussian spatial mode structure and focus to a diffraction limited spot at the crystal since any deviation in spot size will increase the geometric broadening effect.

To minimize any dispersive effects that cannot be compensated for by the diffraction gratings, only front surface aluminum mirrors were used in the autocorrelator and beam steering after the optical fiber. It is important to note that the beamsplitter which is necessary in the autocorrelator provided a source of unbalanced dispersion between the two arms. In spite of the fact that a thin 1.0 mm thick plate beamsplitter was used, this still would contribute a dispersive broadening with a critical pulse width of $T_c \sim 13$ fs. Thus it was necessary to insert a glass plate of similar thickness in the other beam of the autocorrelator in order to restore a dispersive balance that could be compensated for by the diffraction gratings. The parallel beams exiting from the two arms of the auto-

correlator were focussed into the nonlinear crystal with a 15 cm focal length achromatic lens in order to prevent chromatic aberration from affecting the focussing and the second harmonic generation.

The second harmonic generation was performed in a 0.1 mm thick KDP crystal phasematched for 620 nm. The crystal was mounted with UV transmitting cement on a quartz plate (Cleveland Crystals) and was positioned with the crystal toward the incident pulses. The second harmonic signal is spatially aperatured to discriminate against the background beams and detected with a photomultiplier. However, a large enough aperature must be used in order not to filter out desired off-axis second harmonic components. Recent theoretical analysis (21) has shown that the autocorrelation measurement of bandwidth limited pulses is not critically sensitive to either the group velocity mismatch between the fundamental and second harmonic or limitations on the bandwidth of the phase matching. In addition, measurement errors arising from a dispersive broadening of the fundamental pulse in the crystal should also be quite small. For a 0.1 mm KDP crystal, the critical pulse width is $T_c \sim 5.4$ fs. Assuming an incident pulse duration of 16 fs, the dispersive broadening is less than 1 fs. However, it is important to note that a potential measurement error which can underestimate the pulse duration may occur in autocorrelation of a chirped pulse when using a narrow phase matching bandwidth. This effect can be minimized by carefully optimizing the setting of the diffraction grating compressor to avoid introducing chirp as well as using as short a crystal as possible to decrease the group velocity mismatch and increase bandwidth.

The relative delay between the pulse in the autocorrelator was varied

using a 0.1 μm step size stepping motor stage (Klinger Scientific). Scanning was done unidirectionally to eliminate backlash in the stage position. Autocorrelation measurements were taken by computer which controlled the stage position and monitored against laser pulse energy fluctuations on a shot to shot basis. Acceptable signal to noise ratios were obtained by discriminating against greater than 15% pulse energy fluctuations and summing over 5 laser shots per data point with averaging over 2 scans of the delay to reduce any long term fluctuations. The sensitivity of the measured pulse duration to input energy fluctuations was found to be significantly more critical for 16 femtosecond pulses than for those only a factor or two longer. This may be due to the fact that the pulse energies required for this short pulse compression are very close to the threshold for continuum generation in the optical fiber.

Figure 4.5 shows an autocorrelation measurement of the compressed pulses together with the input pulses obtained after two stages of the dye amplifier. The input pulse duration is ∿65 femtoseconds FWHM assuming a $sech^2$ pulse shape. The pulses are compressed by a factor of ∿4x with relatively little energy in the wings of the compressed pulse. Figure 4.6 illustrates a similar autocorrelation measurement of the compressed pulse on an expanded scale. The pulse duration is 16 femtoseconds assuming a $sech^2$ pulse shape. Measurements of the bandwidth of the compressed pulses obtained with a spectrometer and OMA indicate that the pulses are coherent and near transform limited with a time-bandwidth product of $\Delta\nu\Delta t \tilde{=} .43$.

It is important to note that the pulse generation, compression, and measurement with the system that we have described has been very reproducible. The autocorrelation measurements of Figures 4.5 and 4.6 are representative of many traces obtained in the 15-17 femtosecond range. With

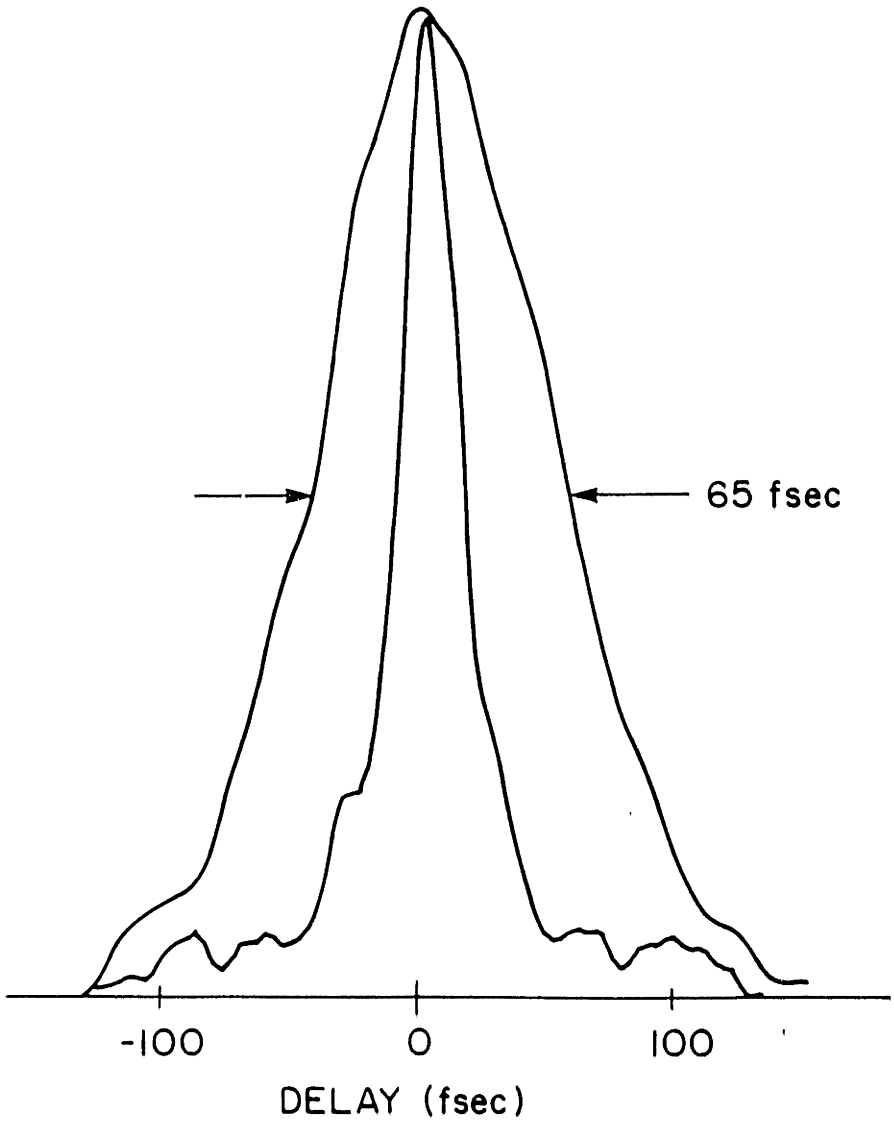

Figure 4.5 Autocorrelation of incident and compressed pulses.

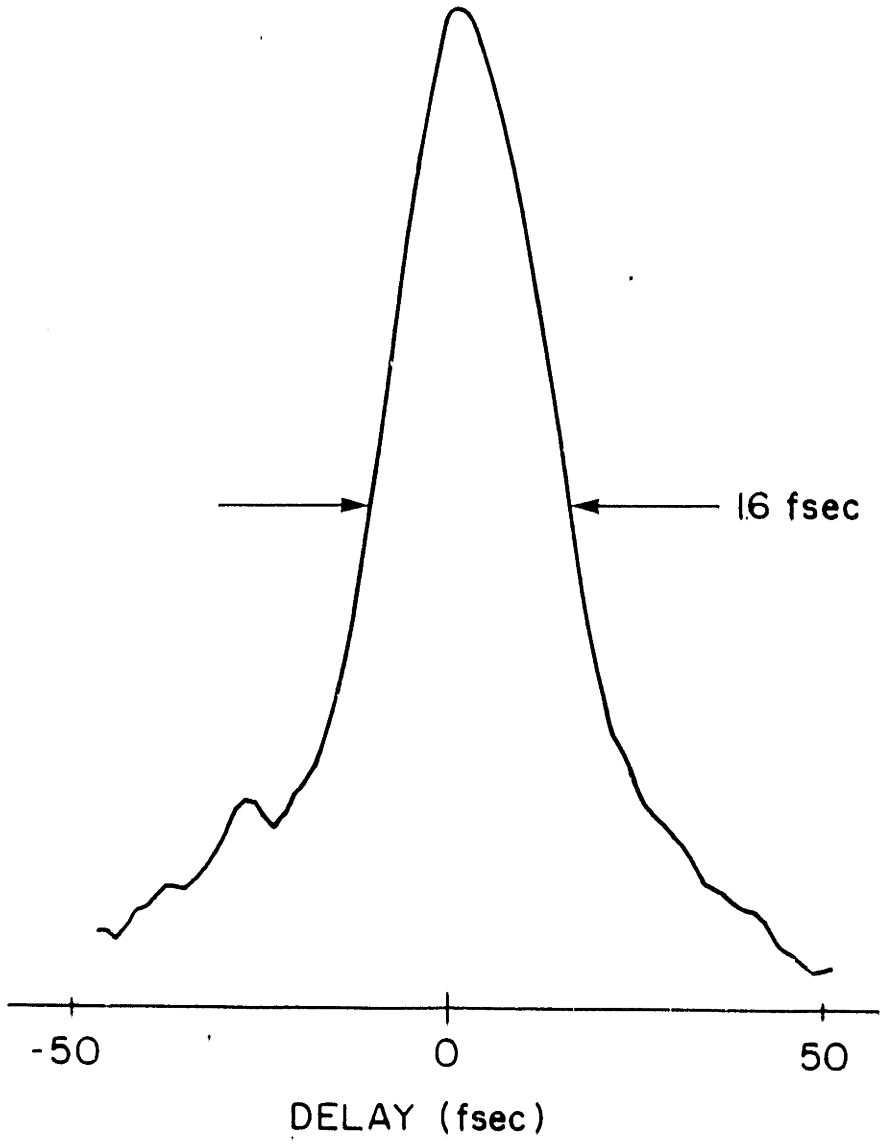

Figure 4.6 Autocorrelation of 16 femtosecond compressed pulse.

our present system, extension to higher powers and shorter fiber lengths has not yet resulted in the generation of shorter pulses. Further advances may require more careful tailoring of the input pulse shape and spectral profile as well as compensation of higher order propagation effects in the fiber, the grating compressor, and other optical elements.

4.5 SUMMARY

This chapter has described the experimental investigation of pulse compression in optical fibers. Using self phase modulation followed by compression with a diffraction grating pair, we have compressed amplified 65 femtosecond laser pulses to durations of 16 femtoseconds. These pulses consist of only eight optical cycles and are the shortest optical pulses generated to date.

The application of optical fiber pulse compression techniques promises to be increasingly useful in future femtosecond optical investigations since it provides a reliable approach for compressing picosecond laser pulses into the femtosecond regime. Used in conjunction with synchronously modelocked dye lasers, these techniques have the potential for producing tunable femtosecond pulses in the visible and near infrared (7). Because of their ability to provide spatial mode control and high intensity pulse confinement over long interaction distances, the use of the optical fibers should prove increasingly important for the future investigation of nonlinear optical phenomena in general.

REFERENCES

1. L.F Mollenauer, R.H. Stolen, and J.P. Gordon, "Experimental Observation of Picosecond Pulse Narrowing and Solitons in Optical Fibers," Phys. Rev. Lett. 45, 1095 (1980).

2. L.F. Mollenauer, R.H. Stolen, J.P. Gordon, and W.J. Tomlinson, "Extreme Picosecond Pulse Narrowing by Means of Soliton Effect in Single-Mode Optical Fibers," Opt. Lett. 8, 289 (1983).

3. L.F. Mollenauer and R.H. Stolen, "The Soliton Laser," Opt. Lett. 9, 13 (1984).

4. H. Nakatsuka, D. Grischkowsky, and A.C. Balant, "Nonlinear Picosecond-Pulse Propagation Through Optical Fibers with Positive Group Velocity Dispersion," Phys. Rev. Lett. 47, 910 (1981).

5. D. Grischkowsky and A.C. Balant, "Optical Pulse Compression Based on Enhanced Frequency Chirping," Appl. Phys. Lett. 41, 1 (1982).

6. B. Nikolaus and D. Grischkowsky, "12x Pulse Compression Using Optical Fibers," Appl. Phys. Lett. 42, 1 (1983).

7. B. Nikolaus and D. Grischkowsky, "90-fs Tunable Optical Pulses Obtained by Two-Stage Pulse Compression," Appl. Phys. Lett. 43, 228 (1983).

8. C.V. Shank, R.L. Fork, R. Yen, R.H. Stolen, and W.J. Tomlinson, "Compression of Femtosecond Optical Pulses," Appl. Phys. Lett. 40, 761 (1982).

9. J.G. Fujimoto, A.M. Weiner, and E.P. Ippen, "Generation and Measurement of Optical Pulses as Short as 16 Femtoseconds," to be published in Applied Physics Letters.

10. D. Marcuse, "Pulse Distortion in Single-Mode Fibers," Appl. Opt. 19, 1653 (1980).

11. H.A. Haus, Waves and Fields in Optoelectronics, Prentice-Hall, New Jersey, 1984.

12. H. Nakatsuka and D. Grischkowsky, "Recompression of Optical Pulses Broadened by Passage Through Optical Fibers," Opt. Lett. 6, 13 (1981).

13. G.W. Fehrenbach and M.M. Salour, "Polariton-Induced Compensation of Picosecond Pulse Broadening in Optical Fibers," in Picosecond Phenomena III, K.B. Eisenthal, R.M. Hochstrasser, W. Kaiser, and A. Laubereau, eds., Springer-Verlag, New York, 1982, p. 126.

14. E.B. Treacy, "Optical Pulse Compression with Diffraction Gratings," IEEE J. Quantum Electron. QU-5, 454 (1969).

15. F. Shimizu, "Frequency Broadening in Liquids by a Short Light Pulse," Phys. Rev. Lett. 19, 1097 (1967).

16. R.A. Fisher, P.L. Kelley, and T.K. Gustafson, Appl. Phys. Lett. 14, 140 (1969).

17. R.H. Stolen and C. Lin, "Self-Phase Modulation in Silica Optical Fibers," Phys. Rev. A 17, 1448 (1978).

18. W.J. Tomlinson, R.H. Stolen, and C.V. Shank, "Compression of Optical Pulses Chirped by Self-Phase Modulation in Fibers," to be published.

19. R.H. Stolen, V. Ramaswamy, P. Kaiser, and W. Pleibel, Appl. Phys. Lett. 33, 699 (1978).

20. E.P. Ippen and C.V. Shank, Ultrashort Light Pulses: Picosecond Techniques and Applications, S.L. Shapiro, ed., Springer-Verlag, New York, 1977, p. 83.

21. A.M. Weiner, "Effect of Group Velocity Mismatch on the Measurement of Ultrashort Optical Pulss via Second Harmonic Generation," IEEE J. Quantum Electron. QE-19, 1276 (1983).

CHAPTER 5

MULTIPHOTON PHOTOEMISSION AND NONEQUILIBRIUM ELECTRON AND LATTICE TEMPERATURES IN TUNGSTEN

5.1 INTRODUCTION

Perhaps one of the most interesting and novel applications of high intensity femtosecond pulses is the generation and measurement of transient high excitation nonequilibrium phenomena. Examples of these processes which have been investigated by previous researchers include plasma formation (1) and melting (2) in silicon. This chapter describes the application of amplified femtosecond laser pulses to the experimental investigation of multiphoton and thermally assisted photoemission from tungsten. Evidence has been found for a transient thermal nonequilibrium between the electrons and lattice. Pump-probe measurements indicate an electron-phonon energy relaxation time of several hundred femtoseconds.

This research has been performed in collaboration with Professor Nicolaas Bloembergen of Harvard University and Dr. Jia-Ming Liu of GTE Laboratories.

5.2 MULTIPHOTON AND THERMALLY ASSISTED PHOTOEMISSION IN METALS

Let us begin by considering the processes of multiphoton and thermally assisted photoemission in metals (3). As shown in Figure 5.1, at low incident laser intensities when heating is negligible, the electrons are in a Fermi distribution which is close to zero temperature. In the case of tungsten, the work function is approximately 4.3 eV. Our laser photon energy is 2 eV and photoemission may occur by a three photon process. At low temperatures the two photon photoemission process is energetically

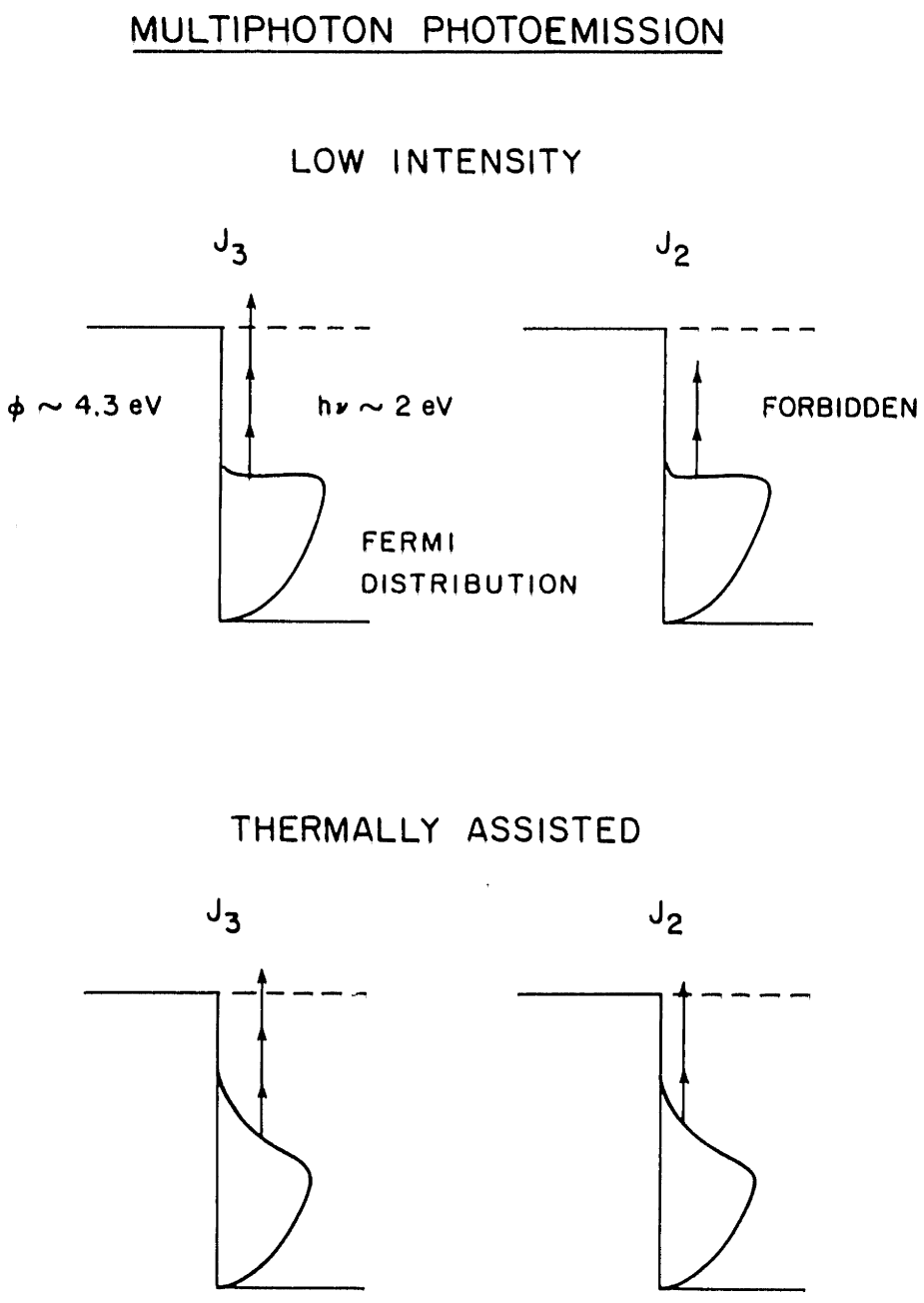

Figure 5.1 Multiphoton and thermally assisted photoemission in metals.

forbidden. If the laser intensity is increased, however, it may be possible to produce a substantial heating of the electron distribution. This produces a Fermi distribution with a high energy tail which allows the two photon photoemission process for electrons in these high energy states. This process is termed thermally assisted two photon photoemission and results in an increased photoemission current which accompanies electron heating. A quantitative description of the relationship of temperature to multiphoton and thermally assisted photoemission may be obtained by application of the generalized Fowler-DuBridge theory (4-6).

When a short optical pulse interacts with a metal, the energy is first absorbed by the electrons which thermalize rapidly by electron-electron scattering. The electrons then transfer energy to the crystal lattice through electron-phonon coupling via deformation potential scattering. Although the electron-phonon collision time as determined by dc conductivity measurements is of the order 10^{-14} - 10^{-15} seconds, the large mass disparity between the electrons and ions increases the energy transfer time to be between 10^{-11} - 10^{-13} seconds.

In the case when the incident laser pulse is long compared to the electron-phonon energy transfer time, the electrons and the lattice will remain in thermal equilibrium and the temperature increase is governed by the heat capacity of the lattice. The electron and lattice temperatures are equal and may be described by the following equation:

$$C_i \frac{\partial T}{\partial t} = K\nabla^2 T + A(\bar{r},t) \tag{5.1}$$

where $A(\bar{r},t)$ represents the heat source determined by the incident laser pulse, K is the thermal conductivity, and C_i is the lattice heat capacity

per unit volume.

When the incident laser pulse is shorter than or comparable to the electron-phonon energy transfer time, the electrons and the lattice are no longer in thermal equilibrium (7). Because of the smaller heat capacity of the electron gas, the electron temperature T_e may be much higher than the lattice temperature T_i. The evolution of the electron and lattice temperatures are then governed by a set of coupled nonlinear differential equations:

$$C_e(T_e)\ \frac{\partial T_e}{\partial t} = K\nabla^2 T_e - g(T_e - T_i) + A(\bar{r},t) \tag{5.2}$$

$$C_i\ \frac{\partial T_i}{\partial t} = g(T_e - T_i) \tag{5.3}$$

$C_e(T_e)$, the electronic heat capacity, depends linearly on the electron temperature. The electron and lattice temperatures are coupled through the coupling constant $g \sim \pi^2 m n v_s^2 / 6 T_i \tau_{ep}$, where m is the electron mass, n the electron density, v_s the sound velocity, and τ_{ep} the electron-phonon collision time (7,8). Since $\tau_{ep} \sim 1/T_i$, g is a constant independent of temperature.

Experimentally, electron temperatures and electron-lattice energy transfer times may be indirectly determined from measurements of the integrated photoemitted charge versus laser pulse intensity. The expected behavior of the photoemission is depicted in Figure 5.2. At low intensities where there is negligible heating, the power law dependence should be third order indicating the intrinsic three photon process. As the laser intensity is increased, heating should become predominant to produce thermally assisted photoemission. This results in an increased photocurrent

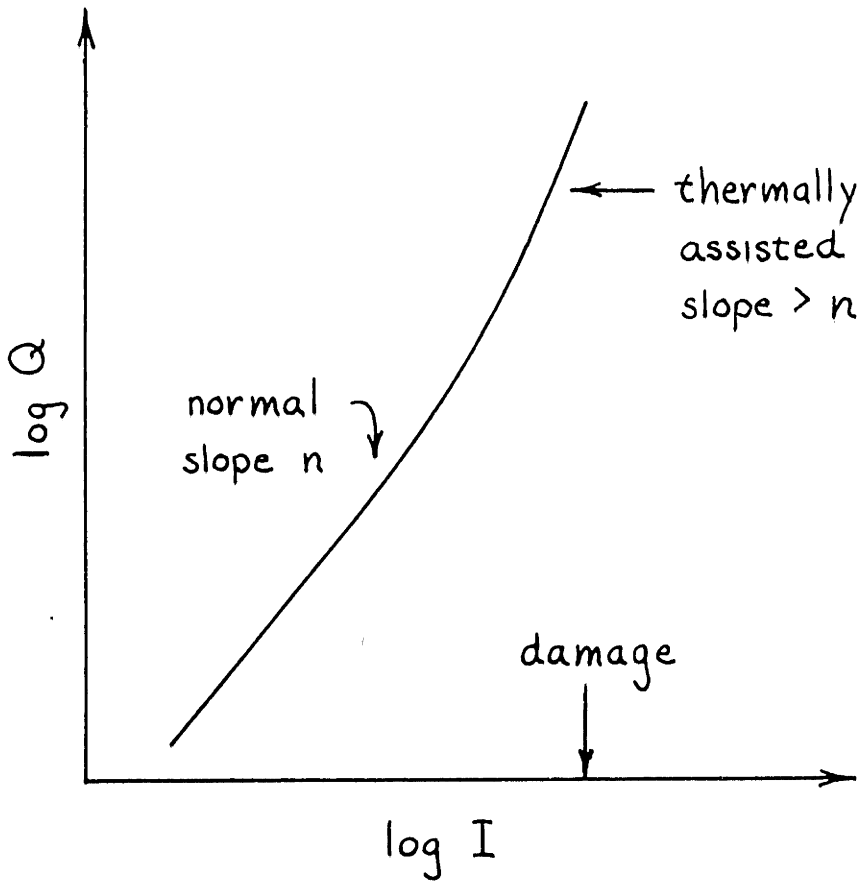

Figure 5.2 Predicted behavior of log emitted charge vs. log intensity.

and is manifest as a nonlinear deviation from the slope three dependence. The slope increases up to the damage threshold where the lattice temperature is equal to the melting temperature. A careful measurement of the photoemitted charge versus laser pulse intensity would indicate if the electrons and lattice were in equilibrium and provide bounds on the electron-phonon energy transfer time.

This approach has been demonstrated by previous investigators. In 1980 Yen et al (9,10) observed thermally assisted photoemission in tungsten using 30 ps pulses at 1.06 μm. No evidence for nonequilibrium electron and lattice temperatures was observed and it was determined that the electron-phonon coupling constant g was greater than 2×10^{11} W/cm^3°K. Subsequent measurements with 2 ps pulses at 300 nm in zirconium also did not indicate any nonequilibrium and placed similar bounds on the coupling constant (11). Very recently, however, evidence for nonequilibrium electron heating has been reported using low intensity picosecond reflectivity measurements in copper (12). This investigation employed thermomodulation spectroscopy to detect small temperature changes of 1°K. However, the time resolution was insufficient to permit the measurement of the electron-phonon energy transfer time.

5.3 EXPERIMENTAL DESCRIPTION

Photoemission measurements were obtained using amplified, high intensity 75 femtosecond laser pulses with the experimental configuration shown schematically in Figure 5.3. The laser pulses were directed at normal incidence onto the surface of a polished polycrystalline tungsten sample mounted inside a high vacuum chamber maintained at 10^{-7} Torr. Typical laser beam sizes at the sample surface were 0.75 - 1.0 mm diameter. A 1 mm

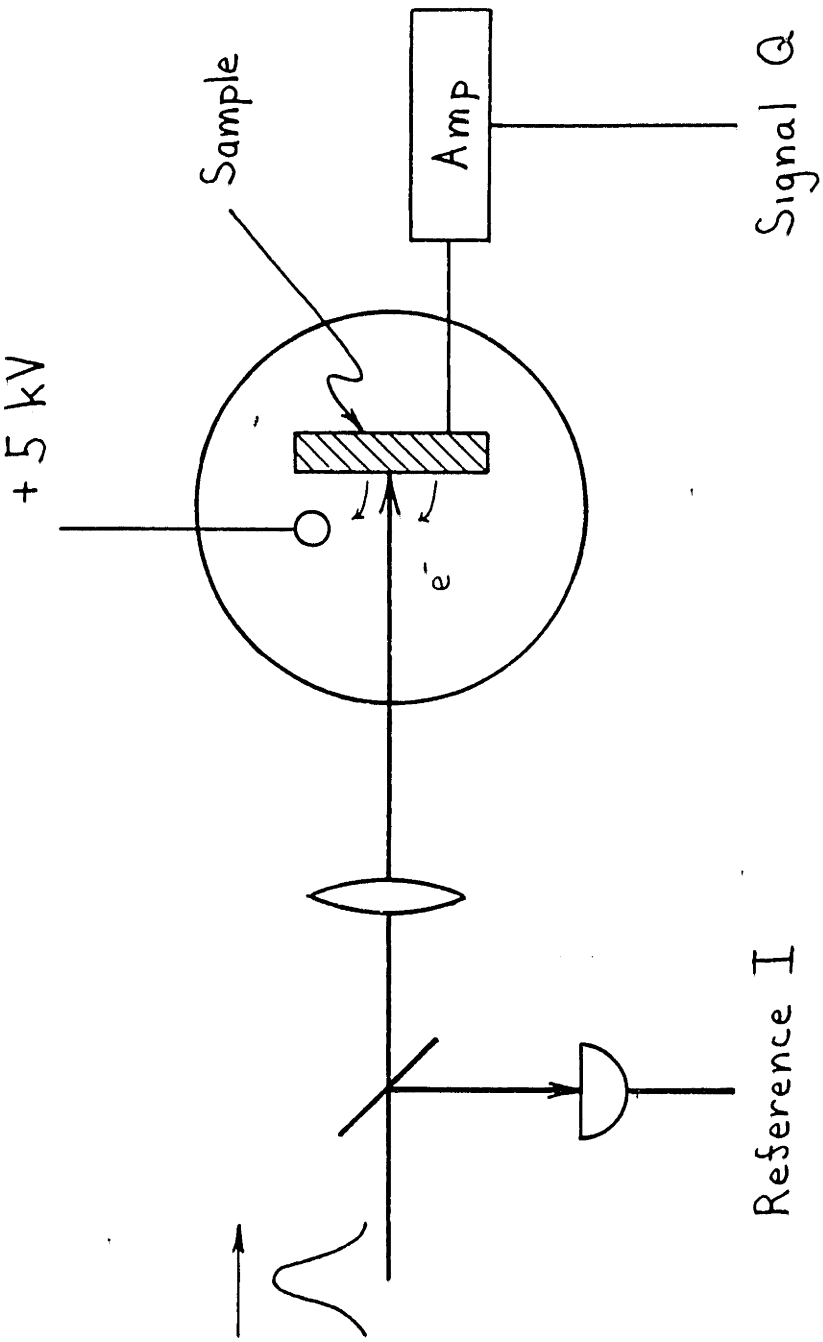

Figure 5.3 Schematic of experimental configuration for photoemission measurements.

diameter wire was mounted 2 mm in front of the sample of the sample surface and biased to 5 kV to function as an anode and to collect the photoemitted charges. The integrated charge emitted from the sample was detected by a high sensitivity low noise amplifier which had a detection limit of $<10^4$ elementary charges. A portion of the incident laser pulse was directed to a reference photodiode which measured the pulse energy. Both the reference and photoemission signals were digitized and recorded by computer on a shot to shot basis.

Pump-probe measurements were obtained by directing the femtosecond pulses into a conventional Michelson type optical delay line. The beam was split into two equal intensity pulses with a variable temporal delay adjusted by a micron step size mechanical stage. The two pulses were directed nearly collinearly onto the sample surface with only a slight misalignment introduced to average over fringes. The collinear configuration was chosen over the crossed beam configuration to reduce geometric time resolution limiting effects which arise from the finite beam spot size and crossing angle at the sample. Data acquisition was performed by a computer which controlled the delay between the two pulses and monitored the laser pulse energies on a shot to shot basis to discriminate against fluctuations. Acceptable signal to noise ratios in pump-probe data could be obtained by discriminating against greater than 25% pulse energy fluctuations and averaging 5 laser shots per data point and scanning 2 to 4 times over the delay range to average any long term fluctuations.

5.4 DISCUSSION OF EXPERIMENTAL RESULTS

The experimentally measured integrated charge emitted by 75 femtosecond laser pulses versus incident pulse intensity is shown on a log-log

plot in Figure 5.4. Each point represents a single laser shot and no averaging has been performed. Note the low scattering of the data points. This indicates that the pulse duration fluctuations of the amplified pulses are extremely small.

The dependence of the photocurrent on the laser pulse intensity differs substantially from what has been observed in previous picosecond photoemission experiments (9-11). At low intensities the dependence does not have the expected slope three of the intrinsic three photon process but instead has an approximate slope of four. At higher intensities the slope gradually decreases with increasing intensity up to the damage threshold. The damage threshold coincides with the onset of visible surface damage as well as the emission of positive ions from the sample.

The decrease in the slope of the photocurrent versus laser intensity which occurs at high intensities is in apparent contradiction to what is expected from thermally assisted photoemission. This behavior is attributed to a charge saturation effect which suppresses the increased photocurrent and masks the signature of thermally assisted photoemission. Because of the extremely short pulse durations, peak currents in excess of 1000 $\mathring{A}/cm^2$ are produced in the high intensity regime. Experimentally, the magnitude of the saturation effect was observed to vary with different anode voltages, becoming more severe for lower voltages. This implies that the charge saturation results from a space charge accumulation in the vacuum rather than an effect which is internal to the metal. The space charge decreases the detected photoemission by screening the tungsten sample surface from the anode extracting field

The observation of space charge saturation has been further investigated by pump-probe measurements of the time dependence of the saturation

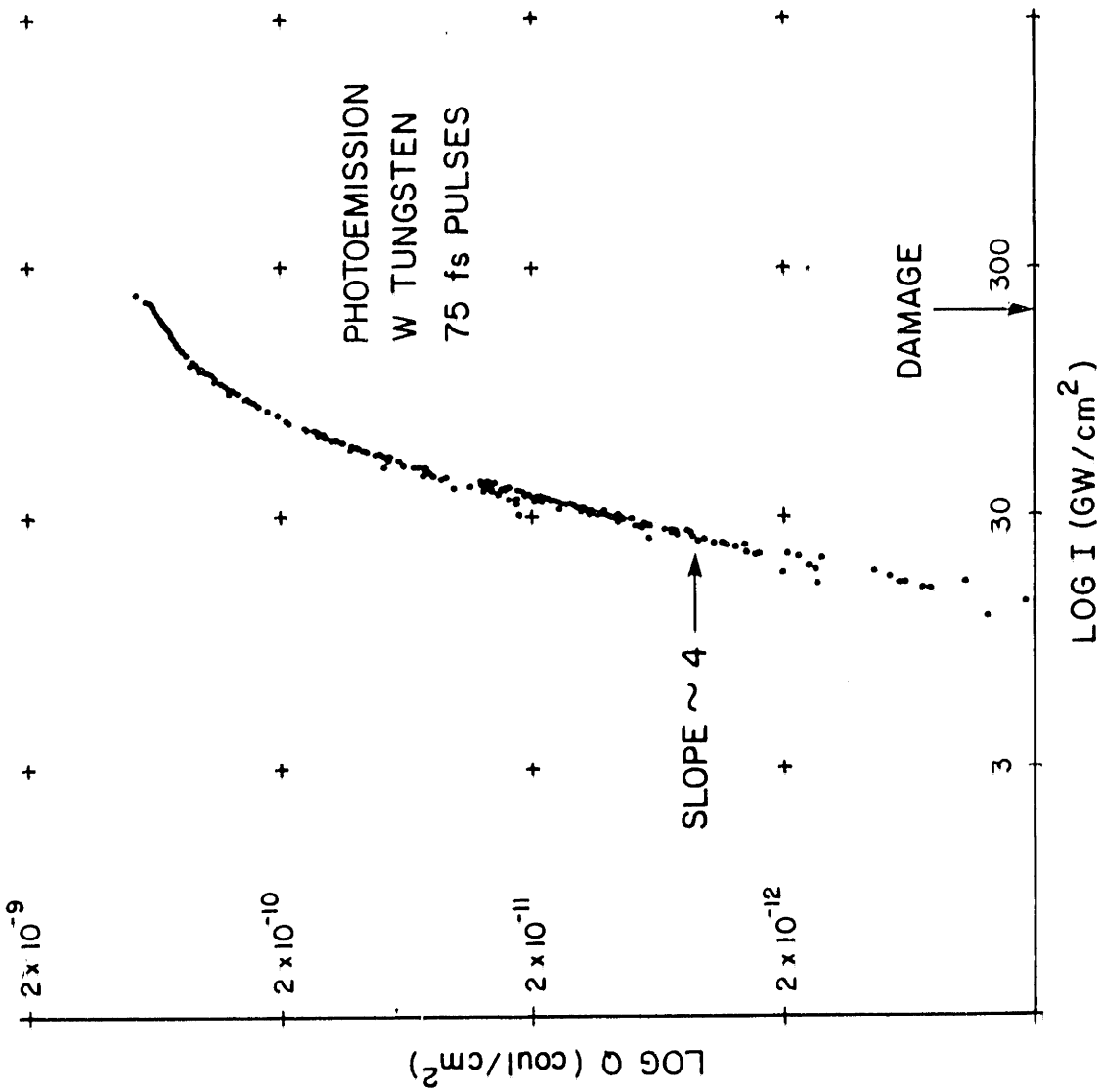

Figure 5.4 Experimentally measured log emitted charge vs. log incident laser pulse intensity.

effect. Figure 5.5 shows pump-probe data obtained using two pulses of equal energy. Traces for pulse intensities of 65 GW/cm^2 and 130 GW/cm^2 are chosen to investigate the highly saturated regime. The traces are symmetric because equal pump and probe pulse energies were used. In the absence of saturation, the total charge emitted from the two temporally separated pulses should be equal to the algebraic sum of the charge produced by the two pulses separately. The depression of the photocurrent observed when the two pulses are closely spaced in time is an indication of the degree of space charge saturation of one pulse produced by the other preceding pulse. Since the charge signal produced by each pulse independently is also saturated, the pump-probe measurement underestimates the degree of saturation. The results indicate, however, that the saturation phenomena is intensity dependent and recovers on a time scale of approximately 100 picoseconds. This is in fact commensurate with the amount of time required for the electrons leaving the metal surface to reach the collecting anode.

The presence of space charge saturation is a serious experimental artifact since it dominates the photoemission at high intensities and suppresses the increased photocurrent which is the signature of thermally assisted photoemission. Attempts to reduce the saturation effect by increasing the anode voltage by changing the geometry of the anode and tungsten electrodes have not resulted in substantial improvement.

Note, however, that even at low incident intensities the photoemission is still more nonlinear than the intrinsic three photon process. As shown in Figure 5.4, a dependence slope four is observed at intensities of <30 GW/cm^2. In fact, the nonlinearity may even be greater because of possible suppression by the space charge effect. Unfortunately, the

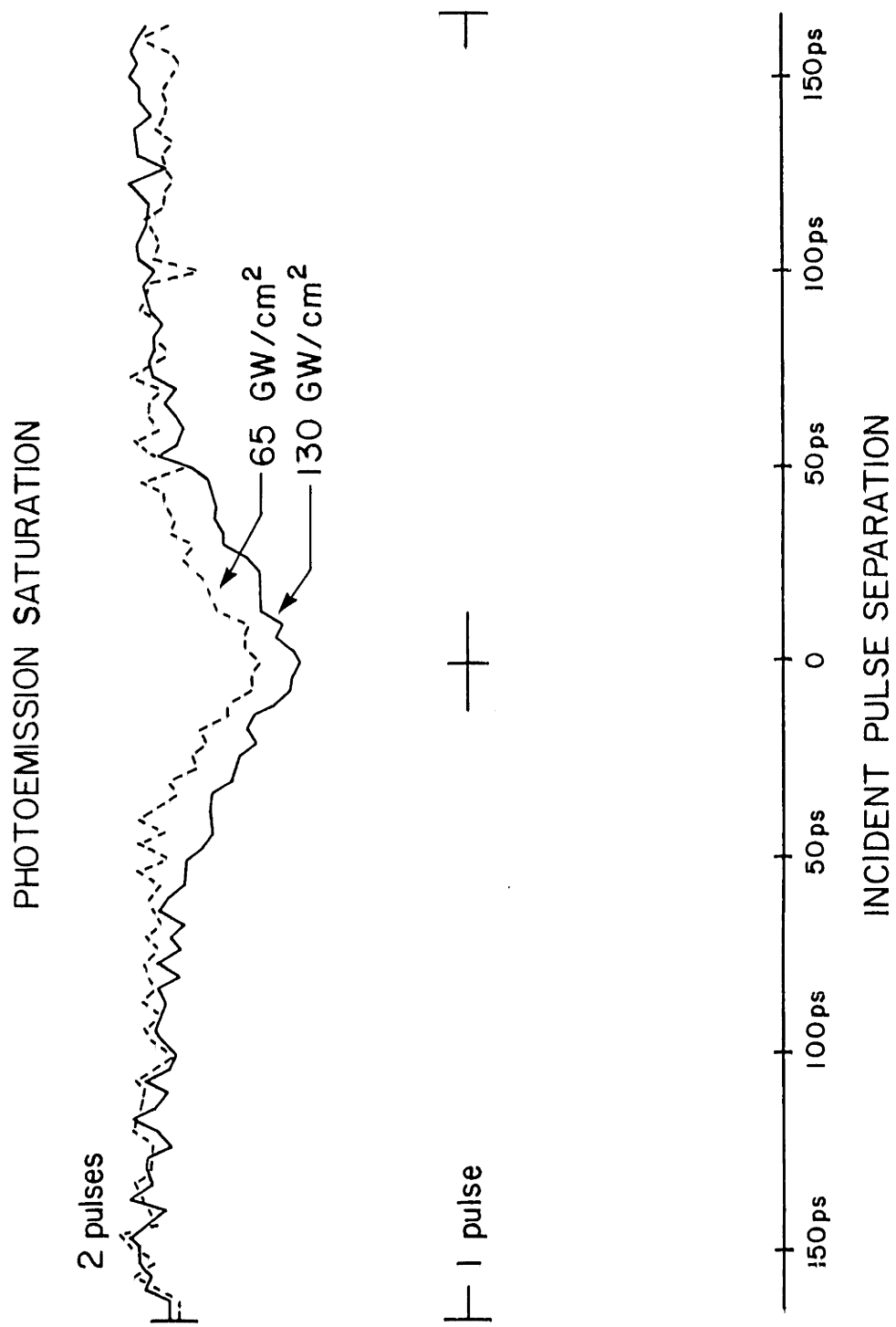

Figure 5.5 Pump-probe measurement of space charge saturation.

observation of the photoemission at even lower laser intensities was limited by the electron detection sensitivity. In spite of the high laser pulse intensities, the extremely short pulse durations yielded only a relatively small amount of total photoemitted charge.

If we interpret this high slope as being produced by a thermally assisted photoemission process, then energy arguments imply that there must be a thermal nonequilibrium between the electrons and the lattice. Since the incident intensities are almost an order of magnitude below the damage threshold, lattice temperature increases of only about 1/10 of the melting ter erature of 3683^{o}K would be possible if the electrons and the lattice were in thermal equilibrium. If, however, there was a transient nonequilibrium, then the same incident intensities could produce electron temperature increases of up to 2000^{o}K.

Evidence for disparate electron and lattice temperatures is further provided by femtosecond pump-probe measurements of the transient electron temperature. Figure 5.6 shows pump-probe measurements obtained using two pulses of equal intensity in the low intensity, unsaturated regime. When the two pulses are temporally overlapped, separated by delays of the order of the pulsewidth or less, the photocurrent is determined by the instantaneous intensity of the coherently overlapping pulses. This yields what is effectively a high order autocorrelation function of the pulse intensity. The expected peak to background contrast ratios would be 10:1 and 35:1 for third and fourth order nonlinearities respectively. The deviation of the contrast ratios of the experimental pump-probe data is the result of the space charge saturation which suppresses the photoemission at high intensities. The trace obtained with 27 GW/cm^2 pulse intensity has a lower contrast ratio than the 13 GW/cm^2 trace, indicating the severity of the

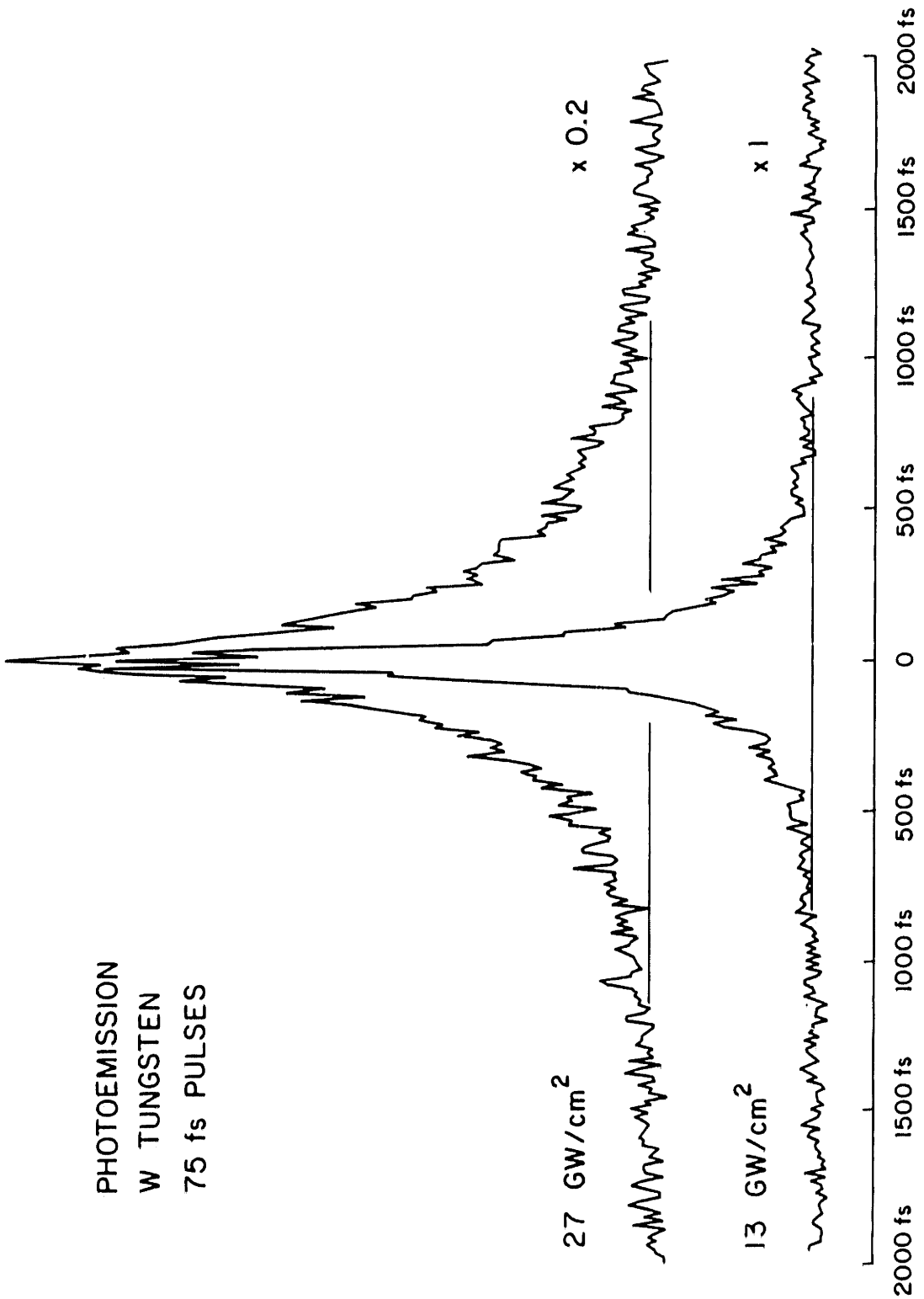

Figure 5.6 Pump-probe measurement of transient nonequilibrium electron-lattice energy transfer.

saturation effect with increasing intensity.

When the two pulses are several hundred femtoseconds apart and are not temporally overlapped, the pump-probe measurement shows the effects of a transient heating of the electrons by the first pulse as it enhances the photoemission induced by the second pulse arriving at a later time. The enhanced photoemission in the wings of the pump-probe correlation data indicates the presence of thermally assisted photoemission with electron temperature increases which last for several hundred femtoseconds.

Note that the actual electron cooling time is less than the time measured from the pump-probe correlation data. Because equal pulse energies were used for both the pump and probe, both pulses contribute equally to the heating. This is in contrast to the usual pump-probe method where the probe pulse is much weaker than the pump and has a negligible effect on the system. The use of different pump and probe pulse energies was not feasible in this experiment because of the fact that the photoemission from the individual pump and probe pulses could not be measured separately. Since the photoemission is a highly nonlinear function of intensity, the dominant contribution to the measured photoemitted charge would then come almost entirely from the pump pulse rather than the probe.

The pump probe data may be qualitatively compared with the behavior of the electron and lattice temperatures predicted by the anomalous heating equations 5.2 and 5.3. Although a closed form solution is impossible, the equations may be solved by computer using implicit finite-difference numerical techniques (10)*. Figure 5.7 illustrates the calculated electron

---

*The author wishes to acknowledge Dr. Jia-Ming Liu for performing this theoretical analysis.

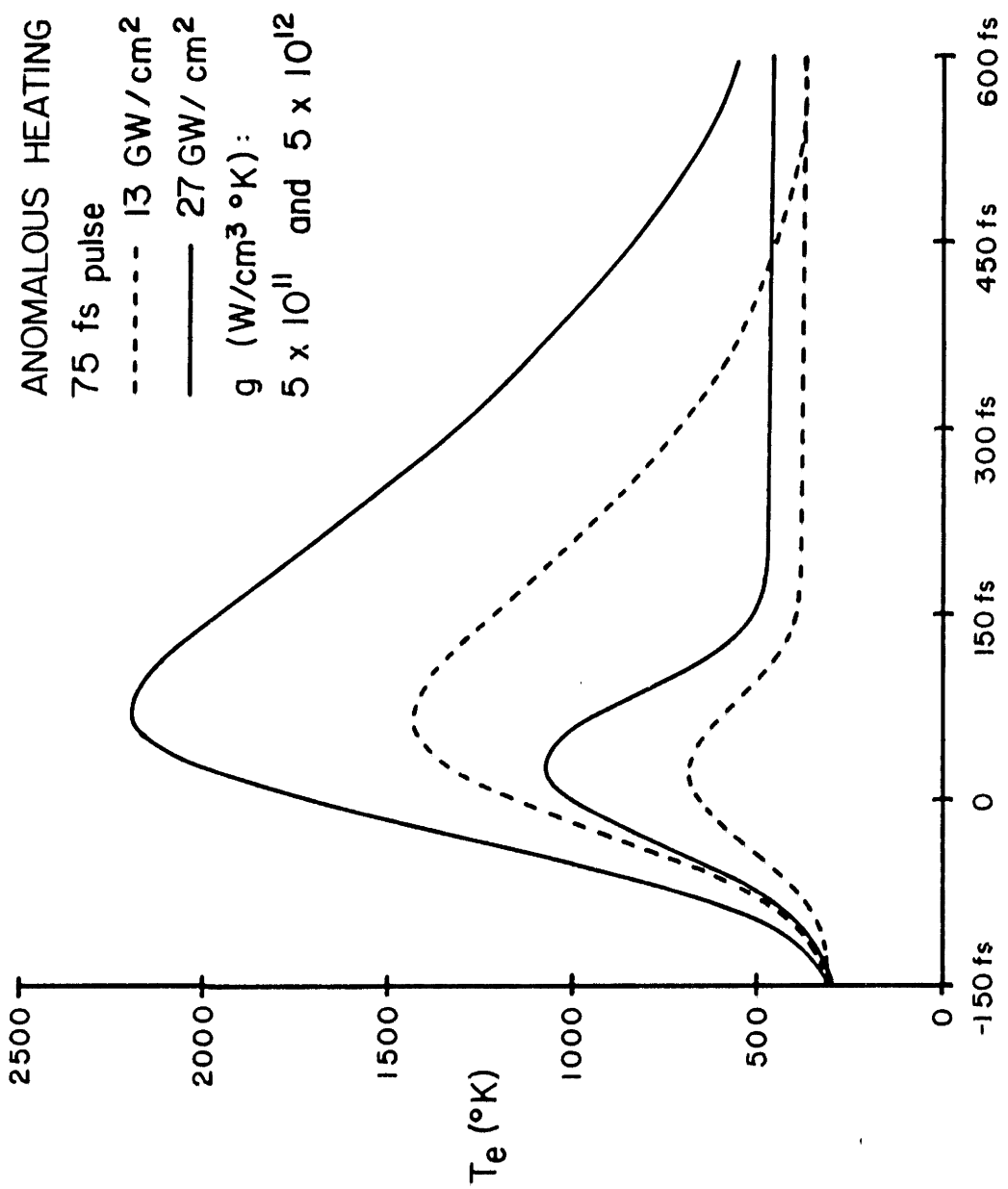

Figure 5.7 Calculated behavior of electron temperature vs. time for anomalous heating.

temperatures for anomalous heating in tungsten produced by 75 femtosecond laser pulses with incident intensities of 13 and 27 GW/cm^2. The upper and lower sets of curves correspond to values of the electron-phonon coupling constant of g equal to 5 x 10^{11} and 5 x 10^{12} W/cm^{3o}K, respectively. When the coupling constant is large the electrons and lattice remain essentially in equilibrium on our time scale. For g greater than $\sim$5 x 10^{13} W/cm^{3o}K, the electron and lattice temperatures approach the normal heating case described by equation 5.1. When the coupling constant is decreased, the electron temperature increases rapidly and requires longer to reach an equilibrum with the lattice. For values of g $\sim$ 1 x 10^{12} W/cm^{3o}K, the elevated electron temperature persists after the laser pulse excitation. As the laser intensity is increased the electron temperature as well as the cooling time increases.

This is in close agreement with our experimental measurements of Figure 5.6. In the trace obtained with 13 GW/cm^2, the wings of the trace persist for $\sim$750 fs. With an increased intensity of 27 GW/cm^2 the wings extend to $\sim$1.25 ps. Since the pump-probe data were obtained using equal pulse energies, the actual time scale of the electron cooling is less than the measured time from the correlation traces. Thus a comparison of the theoretical anomalous heating model with the experimental data indicates a value for the electron-phonon coupling constant of g $\sim$ 5 x 10^{11} - 1 x 10^{12} W/cm^{3o}K.

Although we have performed a qualitative comparison of experiment and theory, the value of the electron-phonon coupling constant can be measured with reasonable accuracy because of the fact that the anomalous heating behavior is strongly dependent on the electron-phonon coupling. Figure 5.8 shows the maximum value of the electron temperature predicted for

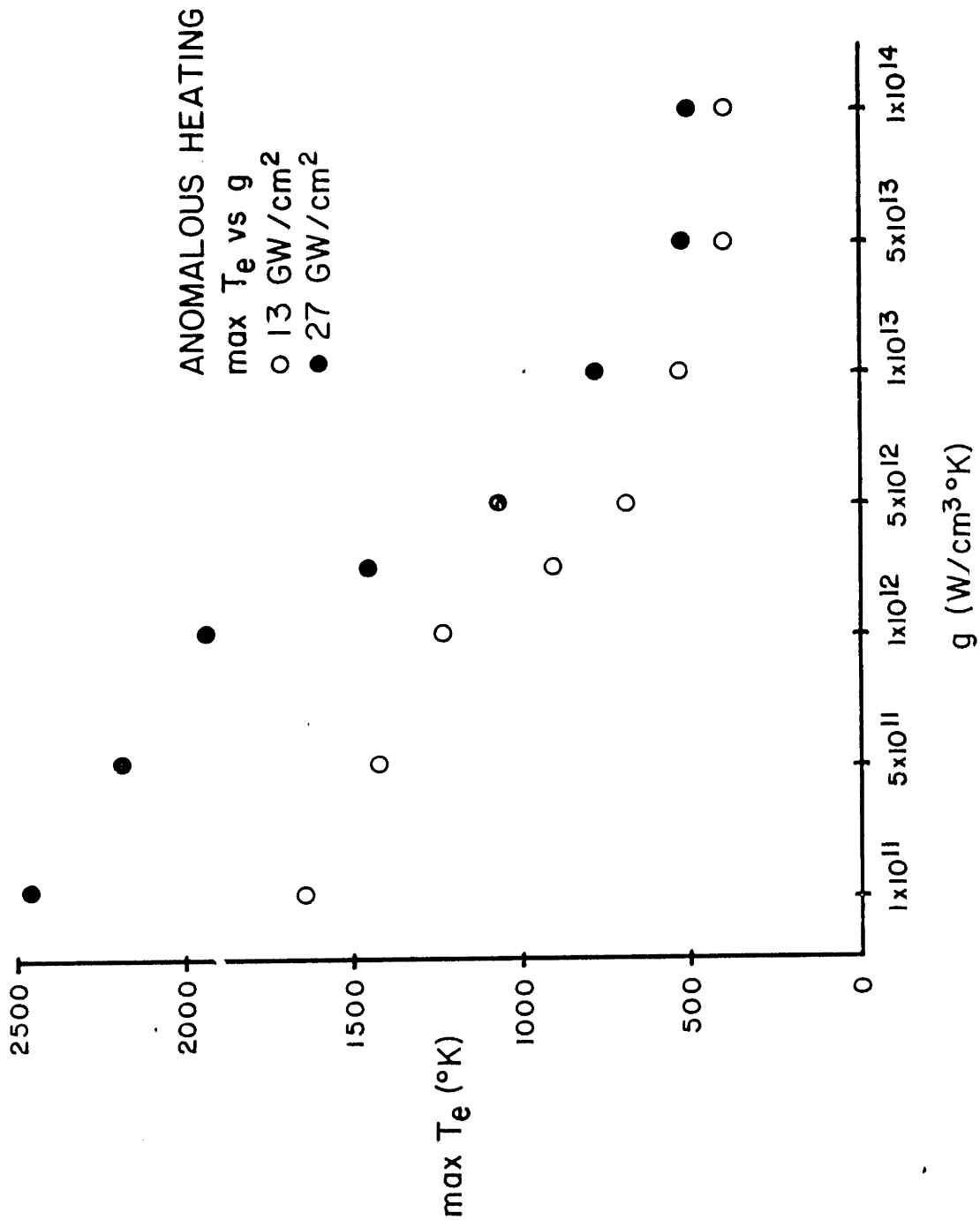

Figure 5.8 Calculated dependence of maximum electron temperature upon the electron-phonon coupling constant.

several different values of g. When g is less than $\sim 5 \times 10^{11}$ W/cm^{3o}K, the electrons and lattice temperatures are almost completely decoupled on our time scale so that the electron temperature increase is determined by the electronic heat capacity. The time required for the electrons to cool also increases rapidly with small values of the coupling constant. In contrast, for g greater than $\sim 5 \times 10^{13}$ W/cm^{3o}K, the electrons and lattice are almost in equilibrium and the temperature increase is determined by the lattice heat capacity. For intermediate values of g, the maximum electron temperature is a strong function of the coupling constant. Thus our experimental measurements determine the coupling constant to a relatively high degree of certainty.

5.5 SUMMARY

In summary, we have applied high intensity 75 femtosecond optical pulses to observe multiphoton and thermally assisted photoemission from tungsten. Space charge saturation has been a serious experimental limitation for these femtosecond pulse studies and arises because of the high current densities. Pump-probe measurements indicate that the saturation lasts for approximately 100 ps, commensurate with the time required for the electrons leaving the sample to be collected by the anode. Measurements of the nonlinear dependence of the integrated photoemitted charge on the incident laser pulse intensity provide evidence for anomalous heating of the electrons and disparate electron and lattice temperatures. Pump-probe measurements of the transient electron heating indicate an electron-phonon energy relaxation time of several hundred femtoseconds. A qualitative comparison with numerical calculations of anomalous heating shows the

electron-phonon coupling constant to be approximately $g \sim 5 \times 10^{11} - 1 \times 10^{12}$ W/cm^{3o}K.

REFERENCES

1. C.V. Shank, R. Yen, and C. Hirlimann, "Time-Resolved Reflectivity Measurements of Femtosecond-Optical-Pulse-Induced Phase Transitions in Silicon," Phys. Rev. Lett. 50, 454 (1983).

2. C.V. Shank, R. Yen, and C. Hirlimann, "Femtosecond-Time-Resolved Surface Structural Dynamics of Optically Excited Silicon," Phys. Rev. Lett. 51, 900 (1983).

3. S.I. Anisimov, V.A. Benderskii, and G. Farkas, "Nonlinear Photoelectric Emission from Metals Induced by a Laser Radiation," Sov. Phys. Usp. 20, 467 (1977).

4. R.H. Fowler, "The Analysis of Photoelectric Sensitivity Curves for Clean Metals at Various Temperatures," Phys. Rev. 38, 45 (1931).

5. L.A. DuBridge, "Theory of Energy Distribution of Photoelectrons," Phys. Rev. 43, 727 (1933).

6. J.H. Bechtel, "Heating of Solid Targets with Laser Pulses," J. Appl. Phys. 46, 1585 (1975).

7. S.I. Anisimov, B.L. Kapeliovich, and T.L. Perel'man, "Electron Emission from Metal Surfaces Exposed to Ultrashort Light Pulses," Sov. Phys. - JETP 39, 375 (1975).

8. M.I. Kaganov, I.M. Lifshitz, and L.V. Tanatarov, "Relaxation Between Electrons and the Crystal Lattice," Sov. Phys. - JETP 4, 173 (1957).

9. R. Yen, J. Liu, and N. Bloembergen, "Thermally Assisted Multiphoton Photoelectric Emission from Tungsten," Opt. Commun. 35, 277 (1980).

10. R. Yen, "Picosecond Laser Induced Nonlinear Photoemission from Metals," Ph.D. Thesis, Department of Physics, Harvard University (1981).

11. R. Yen, J.M. Liu, N. Bloembergen, T.K. Yee, J.G. Fujimoto, and M.M. Salour, "Picosecond Laser Interaction with Metallic Zirconium," Appl. Phys. Lett. 40, 185 (1982).

12. G.L. Eesley, "Observation of Nonequilibrium Electron Heating in Copper," Phys. Rev. Lett. 51, 2140 (1983).

CHAPTER 6

FEMTOSECOND TIME-RESOLVED EXCITON DYNAMICS IN CdSe

6.1 INTRODUCTION

Perhaps one of the most important aspects of the femtosecond dye amplifier is that it facilitates the application of nonlinear optical techniques to generate femtosecond pulses at wavelengths other than the fundamental laser output. In particular, continuum generation by self phase modulation (1) may be used to generate a broadband white light continuum which is ideally suited as a probe for transient measurements of absorption or reflectivity. In this chapter we describe the application of the pump and continuum probe technique to investigate exciton screening in highly excited CdSe using transient reflectivity measurement. To our knowledge, this is the first time-resolved study of screening in II-VI direct-gap semiconductors performed with femtosecond time resolution.

This experiment was performed in collaboration with Dr. Sergey G. Shevel from the Institute of Physics of the Academy of Sciences of the Ukranian SSR. Dr. Shevel was a visiting scientist in our laboratory for a period of three months during the spring of 1983. A summary of the experimental investigation described in this chapter has been published in (2).

6.2 HIGH EXCITATION PHENOMENA IN II-VI SEMICONDUCTORS

The optical properties of highly excited II-VI semiconductors have been the subject of extensive study for more than a decade (3-36). Highly excited semiconductors may be defined as those in which the density of electronic excitations has been increased by an external source to such high values that many body interactions are no longer negligible. This

results in the occurrence of new collective phenomena as well as radiative or nonradiative recombination processes which would not be manifest at lower densities (3). A wide variety of these phenomena have been theoretically predicted and experimentally investigated, including multiple particle excitonic effects, electron-hole plasma and liquid formation, band gap renormalization, and screening. Theoretical analysis has proven to be extremely challenging because, in contrast to the single particle approximations extensively employed in solid state physics, these phenomena are inherently many body processes. The situation for direct gap semiconductors is further complicated by the presence of radiative recombination processes which make these processes highly nonequilibrium. Thus an increased understanding of these phenomena must rely heavily upon experimental investigation.

For highly excited semiconductors at low temperatures, a phase transition between a low density gas of excitons and a liquid phase of a degenerate electron-hole plasma is expected (4-8). This phenomena of electron-hole liquid EHL formation has been investigated and well understood in indirect gap semiconductors such as Ge and Si but remains controversial and less clear in direct gap materials. Experimental investigations of these processes usually rely on measurements of luminescence or gain from the radiative recombination occurring in the electron-hole plasma (3,9-13). However, many of the earlier investigations were complicated because of stimulated emission artifacts which masked the desired luminescence behavior (14,15). Recently there has been a substantial interest in the dynamical behavior of these processes and several studies of time resolved luminescence have been conducted in the picosecond domain (16-25).

At higher temperatures, above the critical temperature for the formation of the electron-hole liquid, a phase transition and separation will no longer occur; however, the presence of free carriers will produce a screening of the Coulomb interaction between the electrons and holes. As the free carrier density is increased, the excitons will become unstable and ionize to undergo a Mott transition from a dielectric exciton gas to a plasma of unbound electrons and holes.

A simple estimate of the free carrier density necessary for the Mott transition may be obtained using the assumption of static screening (26,27). Under this condition, the screened Coulomb potential is:

$$V(r) = -\frac{e^2}{\varepsilon r}\exp(-k_D r) \tag{6.1}$$

$$k_D^2 = 8\pi n e^2/\varepsilon k_B T \tag{6.2}$$

Where k_D is the Debye-Huckel screening length, ε is the dielectric constant, n is the free carrier density, and T is the temperature. Excitonic bound states will be forbidden when the screening length becomes of the order of the exciton Bohr radius $k_D a_0 \tilde{=} 1$. This yields the Mott criteria:

$$n = \varepsilon k_B T/8\pi^2 e^2 a_0^2 = k_B T/16\pi E_x a_0^3 \tag{6.3}$$

In addition to the disappearance of the exciton at the Mott transition, one might also expect a decrease in the binding energy of the exciton with increasing screening. This would be manifest as a short wavelength shift of the exciton resonance. However, a more accurate description of the Mott transition using dynamical screening predicts the occurrence of band

edge renormalization which develops concomitantly with the screening. This causes a decrease in the band gap which tends to cancel any shift in exciton energy. The presence of free carriers produces both interaction vertex corrections which give rise to screening as well as self energy corrections which produce band edge renormalization. As a result, theoretical calculations using dynamical screening predict that the exciton energy remains almost constant as a function of carrier density (3,28-31).

Experimental investigations of exciton screening rely primarily on pump-probe measurements of the excitonic reflectivity or absorption as a function of free carrier concentration (3,12,32-34). In contrast to luminescence, the measurement of reflectivity or absorption in highly excited semiconductors requires the use of at least two independent laser wavelengths. Because of the experimental difficulties involved in this type of investigation, these phenomena have not been well investigated and few time resolved studies have been conducted (35,36). Experimental observations differ substantially. A short wavelength shift of the exciton resonance was observed in some early investigations (16,35); however, recent experiments have shown only a broadening and disappearance of the excitonic features with no appreciable energy shift (12,32-34,36).

6.3 REFLECTIVITY MODEL OF EXCITON RESONANCE

The effects of excitons on reflectivity lineshape may be modelled as a simple oscillator contribution to the dielectric constant (37,38).

$$\varepsilon(\omega) = \varepsilon' + \frac{4\pi\alpha\omega_0^2}{\omega_0^2 - \omega^2 - i\omega\Gamma} \tag{6.4}$$

Where ε' is the background dielectric constant, ω_0 is the exciton resonance

frequency, $4\pi\delta$ is the polarizability of the exciton, and Γ is a phenomenological damping constant. The reflectivity may then be calculated using standard electromagnetic theory (39). For an incident TE wave, the reflectivity is given by:

$$(6.5) \qquad r = \left| (\sqrt{\varepsilon_0}\cos\theta_1 - \sqrt{\varepsilon'}\cos\theta_2)/(\sqrt{\varepsilon_0}\cos\theta_1 + \sqrt{\varepsilon'}\cos\theta_2) \right|^2$$

θ_1 and θ_2 are the incident and refracted angles respectively. ε_0 and ε' are the dielectric constants of the incident and refracting media.

The application of this model is helpful to develop a phenomenological understanding of the effects of exciton screening on the lineshape parameters. A comparison of experimental results in this context has led to several contradictions. Some investigators (12) report that increasing carrier density results only in the increase of damping while others (32-34) report a decrease in exciton polarizability as well. In general, an accurate fit of experimental exciton lineshape requires the use of more complicated models (12). For our purposes, the simple reflectivity model will be used solely to determine the effect of screening on the phenomenological lineshape parameters for the purposes of a qualitative comparison.

6.4 EXPERIMENTAL DESCRIPTION

A schematic diagram of the experimental geometry for the pump and continuum probe measurement is shown in Figure 6.1. The incident high intensity femtosecond pulses were directed onto a beamsplitter and into an optical delay line. A portion of the beam was focussed into a 1 cm cell containing ethylene glycol to generate a broadband femtosecond continuum (1). A colored glass cutoff filter was used to select wavelengths longer

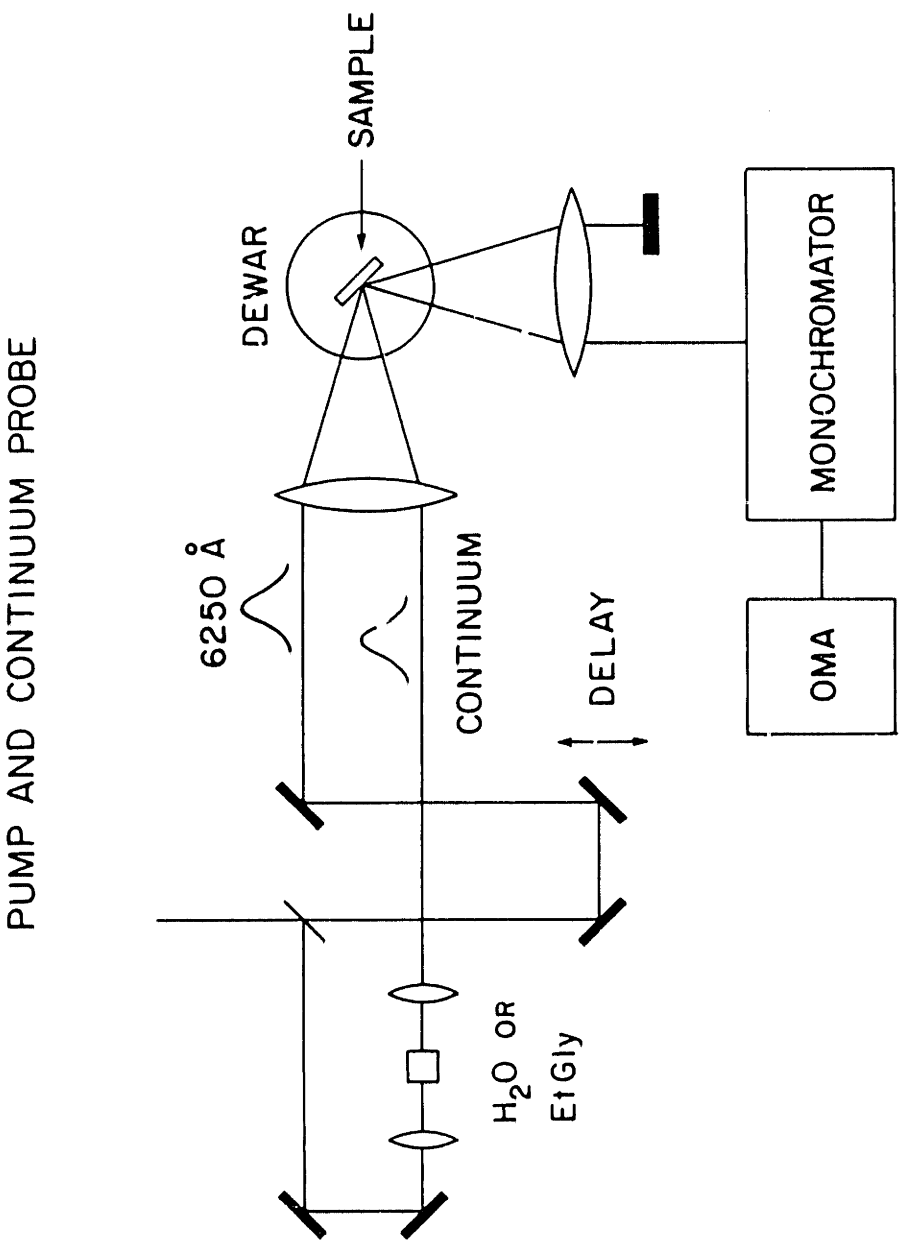

Figure 6.1 Schematic of pump and continuum probe experimental configuration.

than ∿665 nm to yield a flat relatively featureless portion of the continuum suitable for probing the excitonic reflectivity. The remainder of the beam at 620 nm was suitably attenuated and used as a pump. The time delay between the pump and probe pulses was varied by a computer controlled stepping motor mechanical stage with a 1 micron step size. The overall pump-probe geometry used a conventional separated beam delay line geometry. Although this experimental system was employed for reflectivity measurements, a similar design could be used for absorption and gain measurements.

The CdSe sample used for this experiment was a high purity single crystal with a thickness of about 90 microns. It was mounted with silicon oil on a sapphire window contacted to the cold finger of a liquid nitrogen dewar which maintained a sample temperature of $\sim 77^{\circ}K$. The edges of the sample were carefully masked with black paper to reduce contributions to the reflectivity spectrum from scattered light or stimulated emission.

Both pump and probe beams were focussed onto the CdSe crystal at a 45° angle of incidence with transverse (TE) polarization. The crystal was oriented with the c-axis perpendicular to the electric field (E⊥c) so that interactions with both the A and B excitons were allowed. Beam parameters were adjusted to yield 1 mm diameter, concentric pump and probe spots.

The reflected probe beam was filtered with a polarizer and focussed into a 0.3 m grating monochromator. The monochromator output was coupled directly to a scanning vidicon detector and controller (Princeton Applied Research Models 1256 and 1216). The vidicon consisted of a 500 x 500 array of silicon light sensitive diodes which were scanned by an electron beam in a vertical raster pattern. The sensitivity of the vidicon was $\sim 10^{3}$ photons/count. The monochromator projected the spectral components

of the input optical signal as a function of space on the vidicon so that by integrating and digitizing each raster line of the vidicon scan the entire spectrum of an incident optical pulse could be measured simultaneously. The vidicon output was processed by a fast signal averager (Nicolet Model 1170) which accumulated and averaged the spectra from successive laser shots. Reflectivity data was obtained by integrating over $\sim 10^3$ laser shots. The resolution of the monochromator and vidicon as ~ 5 Å.

To establish the effects of the continuum probe itself, reflectivity spectra were first obtained in the absence of the pump beam. Figure 6.2 shows the reflectivity resonance of the A exciton at approximately 684 nm as probed by several different fluences of the femtosecond continuum. The measured energy fluence E_{probe}, ranging from 0.4 $\mu J/cm^2$ to 80 $\mu J/cm^2$, is in each case the total continuum energy contained at wavelengths longer than $\sim$665 nm. For a reference, the reflectivity resonance was also measured with a standard, low-intensity, incandescent cw light source using the identical detection system and geometry. In subsequent pump-probe measurements, a probe energy fluence of 1 $\mu J/cm^2$ was used. Assuming that the continuum had a duration of $\sim$100 fs, this implied peak intensities at the sample surface of at least 10 MW/cm^2.

To examine the effects of above band-gap pumping, the continuum probe was delayed with respect to the pump, and reflectivity spectra were obtained $\sim$1 ps following the excitation at 620 nm. Results obtained for several different pump energy fluences are shown in Figure 6.3. The transient behavior of the screening of the excitonic resonance was then measured by varying the delay between the pump and probe pulses at a pump fluence of $E_{pump} = 25$ $\mu J/cm^2$. Figure 6.4 shows the development of the

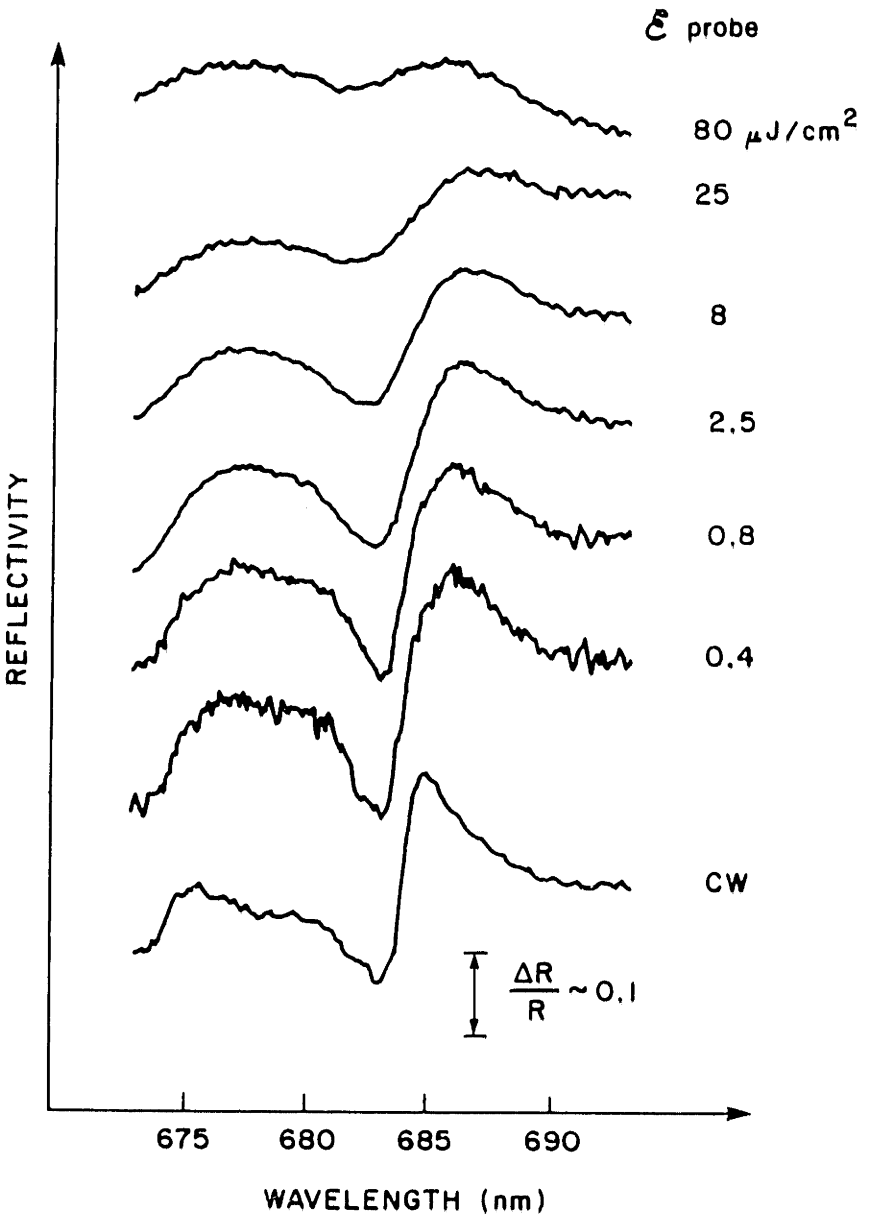

Figure 6.2 Exciton reflectivity lineshape as a function of continuum probe fluence.

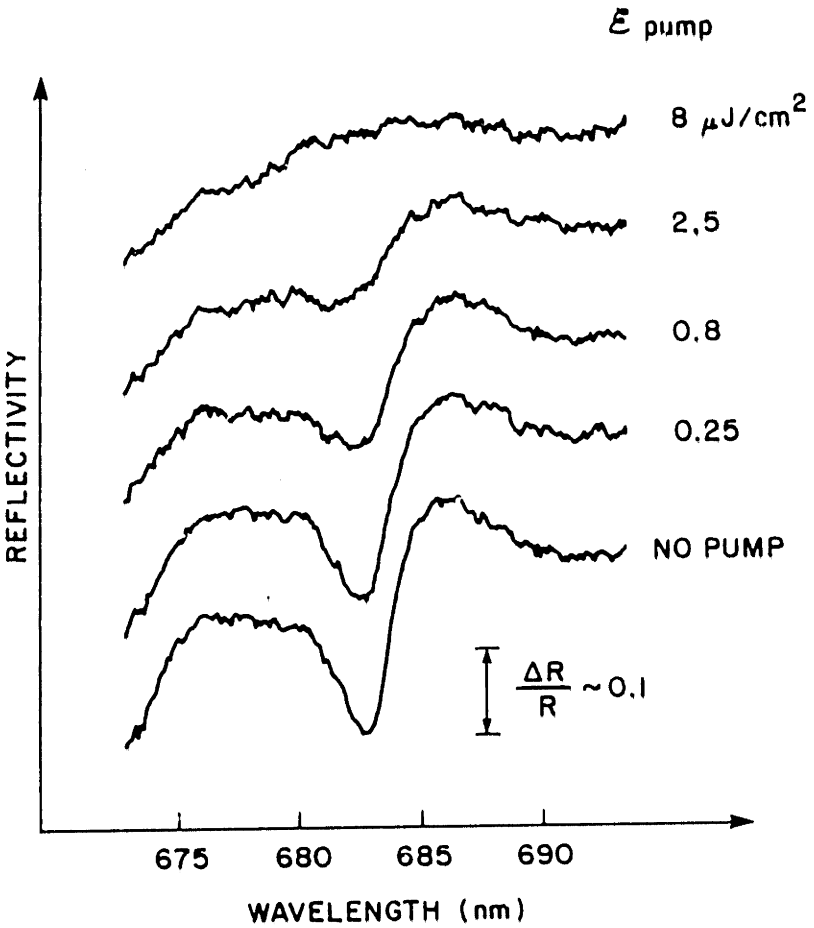

Figure 6.3 Exciton reflectivity lineshape as a function of pump fluence.

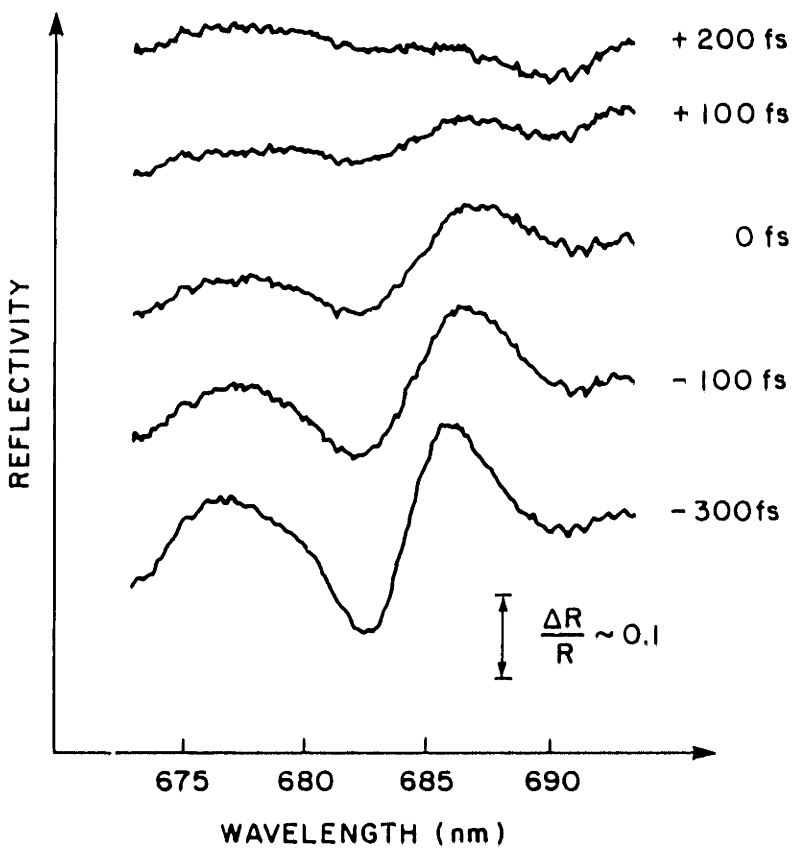

Figure 6.4 Femtosecond time-resolved measurement of exciton screening.

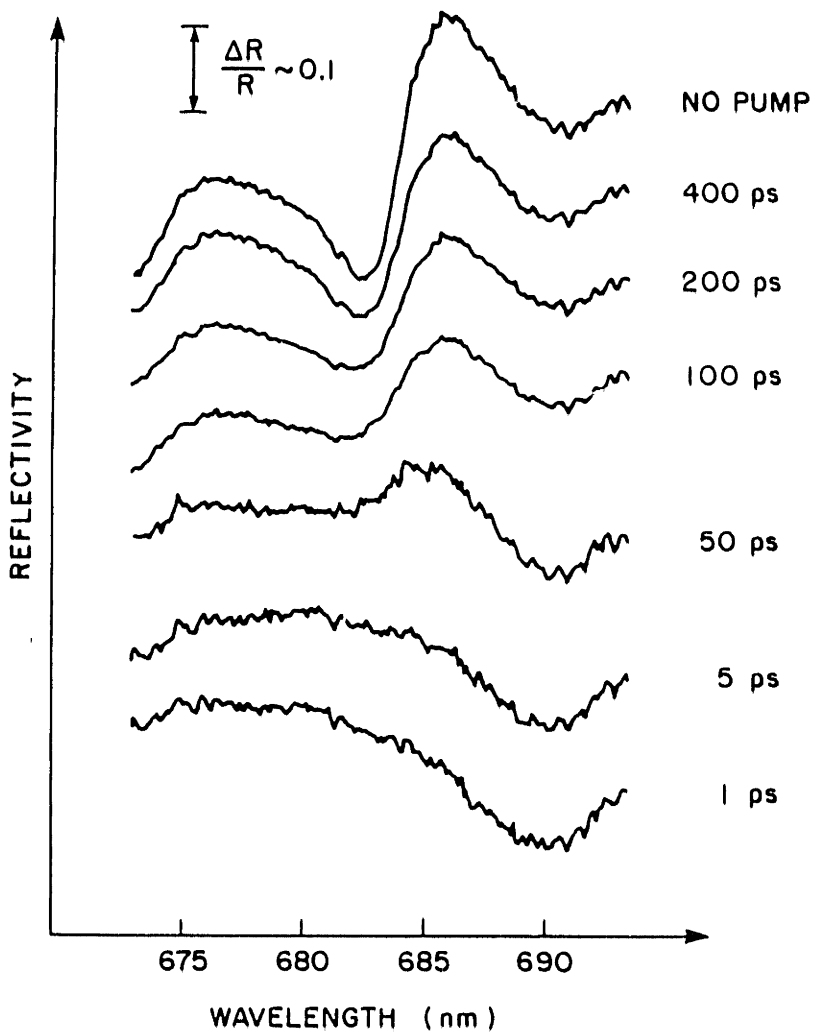

Figure 6.5 Picosecond time-resolved measurement of the recovery of the exciton resonance.

screening on a subpicosecond time scale. Figure 6.5 illustrates the recovery of the excitonic resonance which occurs several hundred picoseconds after the pump excitation.

6.5 DISCUSSION

The results of Figure 6.2 show that the excitonic reflectivity feature can be screened by the action of the 100 fs continuum probe alone, in the absence of the pump. A large 1 mm diameter, laser spot size on the sample was chosen to minimize these continuum self-screening effects while maintaining a measurable signal. Detection sensitivity and the low 10 Hz laser repetition rate prevented the use of lower continuum fluences. It should be noted, however, that a large spot size introduces geometric time resolution limiting effects which arise from the finite crossing angle between the pump and probe beams. In our experiments the angle between the pump and probe was $\sim 3^{o}$. With a 1 mm diameter spot, this implies a geometric arrival time spreading of approximately $(d/c)\sin\theta$ = 175 fs.

As shown in Figure 6.2, the self-screening is a relatively gradual function of the probe fluence. It develops over a two order of magnitude variation in fluence and results in a complete disappearance of the excitonic feature for fluences greater than 80 $\mu J/cm^2$. The reflectivity measured for the lowest probe fluence E_{probe} = 0.4 $\mu J/cm^2$ is in approximate agreement with the lineshape obtained from cw low intensity measurements. Although the total energy in the continuum was relatively constant, the energy density at any given wavelength fluctuated on a shot to shot basis. Reflectivity data was obtained by averaging over many laser shots, so that fluctuations could well be responsible for the apparent gradual dependence of the exciton reflectivity on E_{probe}.

Part of the continuum is absorbed directly by the exciton while part is absorbed by interband transitions producing free carriers. Thus, disappearance of the exciton reflectivity under these circumstances may be caused by resonant field effects, direct exciton saturation, or by free carrier screening. If we assume the latter to be true, the results of Figure 6.2 already imply that the screening develops on a time scale comparable to or less than the ∿100 fs duration of the continuum. Unfortunately, uncertainties in the interband absorption profile and the continuum spectral density preclude a quantitative estimate of the actual excited carrier concentration or its temporal development.

Figure 6.3 illustrates the excitonic screening produced by above band-gap excitation. Spectra were recorded by the continuum probe approximately 1 ps after the generation of free carriers by the pump pulse at 620 nm. Here, the excitonic reflectivity disappears more abruptly with increasing excitation energy fluence than in the case of screening by the continuum alone; but its disappearance still occurs over an order of magnitude variation in E_{pump} and must be classified as gradual, in agreement with previous work (12,32,34,36). Laser pulse energy fluctuations were less than 25% RMS for these measurements, so it is unlikely that the gradual onset of the screening is an experimental artifact.

The exciton feature is completely screened for pump fluences of E_{pump} greater than ∿8 $\mu J/cm^2$. Assuming an optical penetration depth of ∿1 μm, this corresponds to a carrier density of $n \sim 2 \times 10^{17}$ cm^{-3}. This carrier density is of the same order of magnitude as the Mott density (26,27). For CdSe the exciton binding energy for the A exciton is E_x = 15 meV (40) with a Bohr radius of a_0 = 54 Å. At a temperature of 77°K, using equation 6.3, this implies a Mott density $n_M \sim 6 \times 10^{16}$ cm^{-3}.

Although there is an apparent difference in the excitation fluence dependence of the screening of the excitonic reflectivity in Figures 6.2 and 6.3, the shape of the reflectivity line exhibits remarkably similar behavior in the two cases. As the incident fluence is increased, the peak to minimum change ΔR in the reflectivity decreases while the separation or linewidth $\Delta\lambda$ between the peak and minimum wavelengths increases. Within our experimental resolution, the exciton reflectivity feature broadens and disappears without any appreciable wavelength shift.

It is useful to qualitatively compare this experimentally observed lineshape behavior with the predictions of the simple theoretical model of equation 6.4 and relate this behavior to changes in the parameter values in this simple oscillator model. For CdSe the background dielectric constant is $\varepsilon' = 9.7$ and the polarizability of the A exciton is approximately $4\pi\alpha = 0.01$ (40). Typical values for damping at $77^{o}K$ are several meV. The exciton resonance wavelength is taken to be 6845 Å. Figure 6.6a shows the exciton reflectivity lineshapes obtained for a constant polarizability with an increase in damping while Figure 6.6b assumes a constant damping with a decrease in polarizability. Increasing the damping parameter produces a decrease in the reflectivity modulation ΔR while broadening the linewidth $\Delta\lambda$. In contrast, decreasing the excitonic polarizability $4\pi\alpha$ decreases the apparent linewidth as well as the relfectivity modulation ΔR. Note that because of the background dielectric constant, decreasing polarizability also shifts the reflectivity to longer wavelengths.

A quantitative comparison of the experimental data to this reflectivity model is quite difficult because the oscillator parameters are quite sensitive functions of the reflectivity modulation and linewidth. In general, a full fit of the reflectivity lineshape requires the application

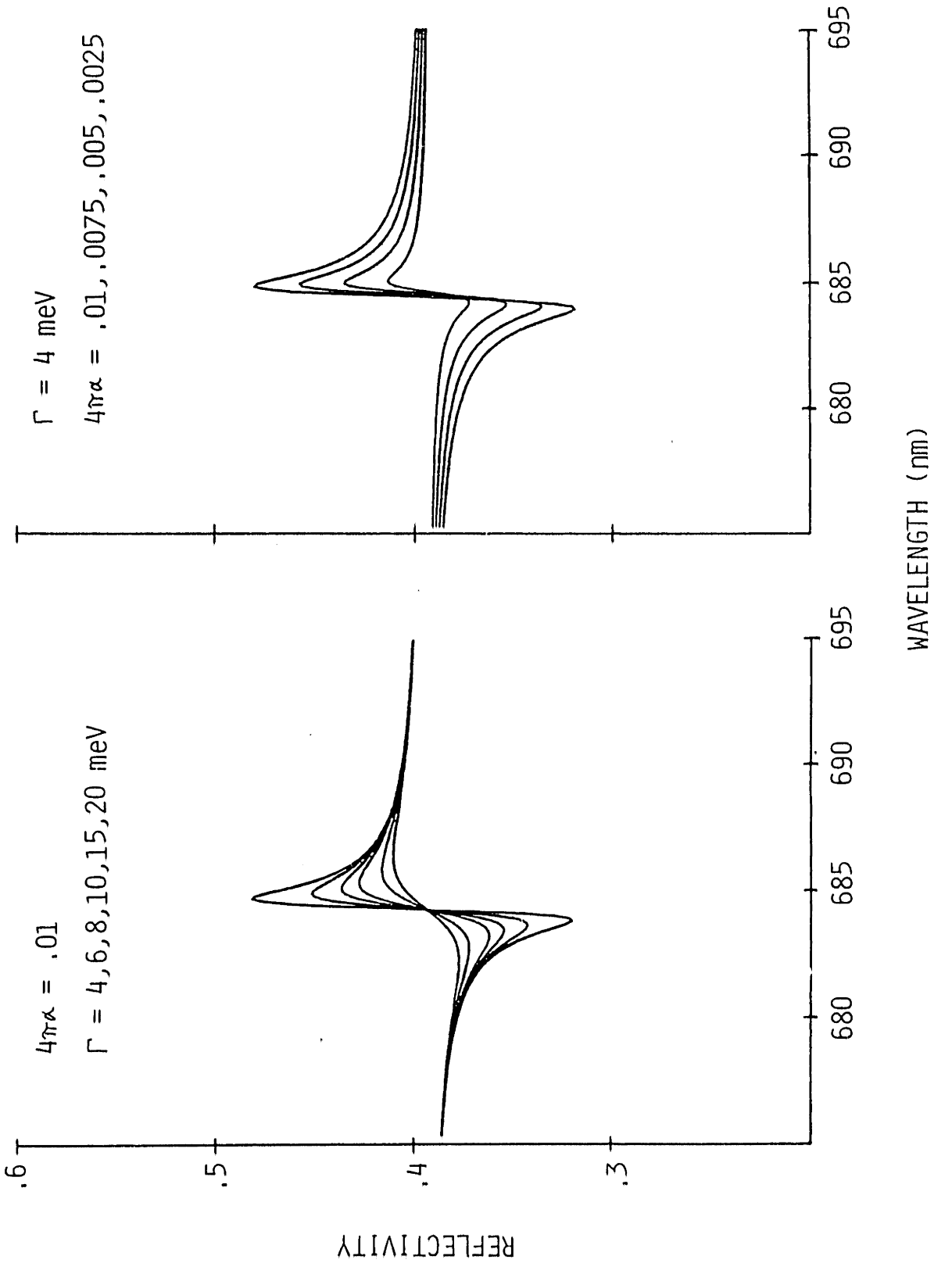

Figure 6.6 Exciton reflectivity lineshapes predicted by simple oscillator model.

of more complicated models involving the assumption of an exciton free layer and/or spatial inhomogeneities (12). While a quantitative fit of the experimental lineshape behavior is difficult, the results of Figures 6.2 and 6.3 indicate that the screening of the exciton can be modelled chiefly by an increase in damping. It should also be noted that while no evidence for a wavelength shift of the exciton reflectivity features is observed, it is possible that any changes in exciton binding energy, band gap renormalization, and exciton polarizability may act together to cancel out any apparent wavelength shift. A more quantitative description of the excitonic oscillator parameters and lineshape would require the use of more complex models as well as measurements obtained at lower temperatures where damping from thermal phonon scattering was less predominant.

Figures 6.4 and 6.5 illustrate the time-resolved transient behavior of the exciton screening. The femtosecond measurements of Figure 6.4 demonstrate that the screening develops on a time scale of 100 fs or less after the excitation of carriers. The apparent risetime of the screening is essentially the experimental resolution limit which results from the 100 fs duration of the continuum pulsewidth as well as geometric time resolution limiting effects arising from the sample spot size and crossing angle between the pump and probe beams. The rapid development of this screening may be taken as evidence that it is the result of free carriers alone, since there is insufficient time to permit the formation of excitons or exciton-exciton collision processes that have previously been attributed to the damping of the exciton line under high excitation conditions (12, 32-34). If, as predicted by theoretical calculations of dynamic screening, the exciton screening and band gap renormalization are directly related manifestations of high density free carriers, then our results are

directly commensurate with previous observations of rapid band edge renormalization in highly excited GaAs (41-43).

The recovery of the excitonic reflectivity resonance occurs on a time scale of several hundred picoseconds as shown in Figure 6.5. This is quite rapid in comparison to the excited carrier lifetime, but is in close agreement with previous results obtained by Frigo, et al (36). Their investigation attributes the rapid recovery of the exciton resonance to an accelerated diffusion of the carriers away from the surface of the sample facilitated by a screening of low temperature impurity scattering of the carriers. Caution must be exercised in applying this model to our temperatures since electron-phonon scattering of the carriers is no longer negligible. However, evidence for rapid spatial expansion of the electron-hole plasma has also been observed in CdSe at high temperatures (44) as well as in GaAs (45). This phenomenon of accelerated diffusion may be related to the screening of the electron-phonon interaction which has been predicted and observed in high density carrier energy relaxation (46-48).

6.6 SUMMARY

We have experimentally investigated the transient behavior of exciton screening via femtosecond pump and continuum probe time-resolved reflectivity measurements. Results show that the complete screening of the exciton develops on a time scale of 100 fs or less with above band-gap carrier densities of $\sim 2 \times 10^{17}$ cm^{-3}. A qualitative analysis of reflectivity lineshape indicates that, within the context of as simple oscillator model, the effect of carrier screening can be described chiefly by an increase in damping. No evidence for a wavelength shift of the exciton resonance was observed. Dynamic recovery of the exciton resonance on a

time scale of several hundred picoseconds was also observed and attributed to a rapid spatial expansion of the electron-hole plasma into the bulk sample.

The development and application of ultrashort pulse measurement techniques such as pump and continuum probe will prove to be increasingly important in achieving an understanding of transient behavior and dynamical processes in semiconductors since most characteristic time constants for direct gap materials are too short to be measured by nanosecond lasers. Many processes such as carrier relaxation, dephasing, and scattering occur on a picosecond or subpicosecond time scale.

REFERENCES

1. R.L. Fork, C.V. Shank, C. Hirlimann, R. Yen, and W.J. Tomlinson, "Femtosecond White-light Continuum Pulses," Opt. Lett. 8, 1 (1983).

2. J.G. Fujimoto, S.G. Shevel, and E.P. Ippen, "Femtosecond Time-Resolved Exciton Dynamics in CdSe," Solid State Commun. 49, 605 (1984).

3. C. Klingshirn and H. Haug, "Optical Properties of Highly Excited Direct Gap Semiconductors," Phys. Reports 70, 315 (1981).

4. T.M. Rice, "Semiconductor-Metal Transitions," in Physics of Highly Excited States in Colids, M. Veta and Y. Nishima, eds., Springer-Verlag, New York, 1976, p. 144.

5. G. Beni and T.M. Rice, "Electron-Hole Liquids in Polar Semiconductors," Phys. Rev. Lett. 37, 874 (1976).

6. R. Zimmermann and M. Rösler, "Theory of Electron-Hole Plasma in CdS," Phys. Stat. Sol. (b) 75, 633 (1976).

7. M. Rösler and R. Zimmermann, "Phase Diagram of Electron-Hole Liquids in Polar Semiconductors," Phys. Stat. Sol. (b) 83, 85 (1977).

8. G. Beni and T.M. Rice, "Theory of Electron-Hole Liquid in Semiconductors," Phys. Rev. B 18, 768 (1978).

9. R.F. Leheny and J. Shah, "Experimental Evidence for the Existence of and Electron-Hole Liquid in II-VI Compounds," Phys. Rev. Lett. 37, 871 (1976).

10. R.F. Leheny and J. Shah, "Condensation of Optically Excited Carriers in CdS: Determination of an Electron-Hole-Liquid Phase Diagram," Phys. Rev. Lett. 38, 511 (1977).

11. G.O. Müller, H.H. Weber, V.G. Lysenko, V.I. Revenko, and V.B. Timofeev, "Electron-Hole Liquid in CdS Crystals as Revealed by Non-Equilibrium Transmission Spectroscopy," Solid State Commun. 21, 217 (1977).

12. K. Bohnert, G. Schmieder, and C. Klingshirn, "Gain and Reflection Spectroscopy and the Present Understanding of the Electron-Hole Plasma in II-VI Compounds," Phys. Stat. Sol. (b) 98, 175 (1980).

13. H. Haug, D.B. Tran Thoai, S. Schmitt-Fink, K. Bohnert, C. Klingshirn, and G. Blattner, "The Electron-Hole Plasma in Direct II-VI Compounds," J. Phys. Soc. Japan 49, Suppl. A, 503 (1980).

14. H. Yoshida, H. Saito, S. Shionoya, and V.B. Timofeev, "Time-Resolved Spectra of Spontaneous Luminescence from High Density Electron-Hole Plasma in CdS," Solid State Comm. 33, 161 (1980).

15. A. Cornet, T. Amand, M. Pugnet, and M. Brousseau, "Spot Size Effects in Picosecond Luminescence Experiments," Solid State Commun. 43, 147 (1982).

16. H. Kuroda and S. Shionoya, "Dynamical Processes of High Density Single Excitons and Excitonic Molecules in CdSe," J. Phys. Soc. Japan 36, 476 (1974).

17. T. Daly and H. Mahr, "Time-Resolved Luminescence Spectra in Highly Photo-Excited CdSe at 1.8^{o}K," Solid State Commun. 25, 323 (1978).

18. G.A. Boiko, V.S. Dneprovskii, M.V. Kraevskii, K. Marinova, S.M. Oak, E.K. Silina, and V.S. Fokin, "A Study of Kinetics of Recombination Radiation of CdS and CdSe Crystals," Phys. Stat. Sol. (b) 85, 111 (1978).

19. T. Kobayashi, Y. Segawa, and S. Mabu, "Picosecond Decay Kinetics of CdSe Luminescence Studied by a Streak Camera," Solid State Comm. 31, 253 (1979).

20. A. Cornet, J. Collet, T. Amand, M. Pugnet, and M. Brousseau," Picosecond Luminescence of CdS and CdSe at High Excitation," J. Luminescence 24/25, 609 (1981).

21. H. Saito, W. Graduszus, and E.O. Gobel, "Picosecond Spectroscopy of Highly Excited GaAs and CdS," in Picosecond Phenemona III, K.B. Eisenthal, R.M. Hochstrasser, W. Kaiser, and A. Laubereau, eds., Springer-Verlag, New York, 1982, p. 353.

22. H. Yoshida and S. Shionoya, "Picosecond Luminescence and Relaxation in High Density Electron-Hole Plasma in CdSe," J. Luminescence 24/25, 601 (1981).

23. H. Yoshida, H. Saito, and S. Shionoya, "Picosecond Relaxation Processes of High Density Electron-Hole Plasma in CdSe," Phys. Stat. Sol. (b) 104, 331 (1981).

24. H. Yoshida, H. Saito, and S. Shionoya, "Luminescence and Inter-Valence Band Hole Relaxation in High Density Electron-Hole Plasma in CdSe and CdS," J. Phys. Soc. Japan 50, 881 (1982).

25. D. Hulin, A. Antonetti, L.L. Chase, J.L. Martin, A. Migus, and A. Mysyrowicz, "Electron-Hole Plasma in CuCl After Subpicosecond Photoexcitation," Opt. Commun. 42, 260 (1982).

26. N.F. Mott, "Electrons in Disordered Structures," Adv. Phys. 21, 785 (1972).

27. N.F. Mott, Metal-Insulator Transitions, Barnes and Noble, New York, 1974.

28. J.G. Gay, "Screening of Excitons in Semiconductors," Phys. Rev. B. 4, 2567 (1971).

29. G. Mahler and J.L. Birman, "Theory of Electron-Hole Plasma in Highly Excited Si and Ge," Phys. Rev. B 16, 1552 (1977).

30. R. Zimmermann, K. Kilimann, W.D. Kraeft, D. Kremp, and R. Röpke, "Dynamical Screening and Self-Energy of Excitons in the Electron-Hole Plasma," Phys. Stat. Sol. (b) 90, 175 (1978).

31. S. Schmitt-Rink, J. Lowenau, and H. Haug, "Theory of Absorption and Refraction of Direct-Gap Semiconductors with Arbitrary Free-Carrier Concentrations," Z. Phys. B - Condensed Matter 47, 13 (1982).

32. J. Heidmann and T. Skettrup, "Disappearance of Exciton Reflection in ZnO at High Excitation Levels," Solid State Commun. 23, 27 (1977).

33. R.F. Leheny, J. Shah, G. Carina Chiang, "Exciton-Contribution to the Reflection Spectrum at High Excitation Intensities in CdS," Solid State Commun. 25, 621 (1978).

34. A. Kuroiwa, H. Saito, and S. Shionoya, "Exciton Reflection Spectra under High-Intensity Excitation in CdS and CdSe," Phys. Stat. Sol. (b) 96, 483 (1979).

35. H. Kuroda and S. Shionoya, "Measurements of Exciton Absorption with Picosecond Light Pulses Produced by Self-Phase Modulation Technique," Opt. Commun. 10, 74 (1974).

36. N.J. Frigo, H. Mahr, and D.J. Erskine, "Application of a Two-Wavelength Picosecond Laser to Semiconductors," IEEE J. Quantum Electron. QE-18, 192 (1982).

37. J.J. Hopfield, "Theory of the Contribution of Excitons to the Complex Dielectric Constant of Crystals," Phys. Rev. 112, 1555 (1958).

38. J.J. Hopfield, and D.G. Thomas, "Theoretical and Experimental Effects of Spatial Dispersion on the Optical Properties of Crystals," Phys. Rev. 132, 563 (1963).

39. J.D. Jackson, Classical Electrodynamics, Wiley, New York, 1962.

40. R.G. Wheeler and J.O. Dimmock, "Exciton Structure and Zeeman Effects in CdSe," Phys. Rev. 125, 1805 (1962).

41. C.V. Shank, R.L. Fork, R.F. Leheny, and J. Shah, "Dynamics of Photoexcited GaAs Band-Edge Absorption with Subpicosecond Resolution," Phys. Rev. Lett. 42, 112 (1979).

42. R.F. Leheny, J. Shah, R.L. Fork, C.V. Shank, and A. Migus, "Dynamics of Hot Carrier Cooling in Photo-Excited GaAs," Solid State Commun. 31, 809 (1979).

43. D. Von der Linde, J. Kuhl, and R. Lambrich, "Picosecond Nonlinear Spectroscopy of Electrons and Phonons in Semiconductors," in Picosecond Phenomena II, R.M. Hochstrasser, W. Kaiser, and C.V. Shank, eds., Springer-Verlag, New York, 1980, p. 275.

44. A Cornet, T. Amand, M. Pugnet, M. Brousseau, "Time Resolved Spatial Expansion of the Electron-Hole Plasma in Polar Semiconductors," in Picosecond Phenomena III, K.B. Eisenthal, R.M. Hochstrasser, W. Kaiser. and A. Laubereau, eds., Springer-Verlag, New York, 1982, p. 364.

45. K.M. Romanek, H. Nather, and J. Fischer, "Spatial Expansion of the Electron-Hole Plasma in GaAs," J. Luminescence 24/25, 598 (1981).

46. J. Shah, "Hot Electrons and Phonons Under High Intensity Photoexcitation of Semiconductors," Solid State Electron. 21, 43 (1978).

47. E.J. Yoffa, "Screening of Hot-Carrier Relaxation in Highly Photoexcited Semiconductors," Phys. Rev. B 23, 1909 (1981).

48. M. Pugnet, J. Collet, and A. Cornet, "Cooling of Hot Electron-Hole Plasmas in the Presence of Screened Electron-Phonon Interactions," Solid State Commun. 38, 531 (1981).

CHAPTER 7

CONCLUSION

This thesis research involved the development of a femtosecond high intensity dye laser amplifier and its application to the investigation of ultrafast transient phenomena. The first part of this research focussed on the construction of a four stage femtosecond dye laser amplifier. Pumped with a Nd:YAG laser and used in conjunction with a passively mode-locked ring dye laser, the dye amplifier operates at 620 nm to produce 65-85 femtosecond optical pulses with peak intensities of up to several gigawatts. The high intensities and femtosecond time resolution provided by this laser system facilitates a wide variety of experimental studies which would be impossible with low intensity laser pulses. The second and major portion of this thesis involved the establishment of a research program in high intensity femtosecond time resolved spectroscopy. Several experimental studies have been performed which obtained new information on specific topics of current scientific interest in nonlinear optics and solid state physics as well as developing and demonstrating new femtosecond generation and measurement techniques for the extension of picosecond spectroscopy into the femtosecond regime.

The transient behavior of parametric four wave mixing was investigated with high intensity femtosecond pulses. Special emphasis was placed on the measurement of scattered pulse durations as an indicator of the transient properties of the nonlinear optical process. In contrast to measurements of integrated scattered energy, this technique was shown to be potentially more sensitive for the determination of material time constants as well as incident pulse shape. The application of transient

parametric scattering for optical gating and pulse shortening was demonstrated by the generation of high intensity 37 femtosecond pulses from amplified 65 femtosecond pulses.

The use of nonlinear optical fiber pulse compression techniques for the generation of short pulses was demonstrated by the compression of amplified pulses to durations as short at 16 femtoseconds. This was performed using self phase modulation in a short optical fiber followed by a diffraction grating pair. These pulses consist of only eight optical cycles and are the shortest optical pulses generated to date. Special experimental techniques required for the generation and measurement of these extremely short pulse durations were demonstrated and elucidated.

High intensity 75 femtosecond amplified pulses were applied to generate and investigate nonequilibrium electron heating in metallic tungsten. Observation of multiphoton and thermally assisted photoemission indicated a transient thermal nonequilibrium between the electrons and lattice. Pump-probe techniques were employed to perform the first direct time resolved measurement of electron-phonon energy relaxation in metals. Experiments indicate an electron-phonon coupling constant of $g = .5 - 1 \times 10^{12}$ $W/cm^{3o}K$, corresponding to an energy transfer time of several hundred femtoseconds.

Finally, the viability of high intensity femtosecond spectroscopy for studies of semiconductors was demonstrated by the experimental investigation of femtosecond exciton dynamics in highly excited CdSe. The high intensities produced by the dye amplifier facilitate the application of nonlinear optical techniques for the generation of femtosecond optical pulses at other wavelengths. In particular, the use of pump and continuum probe

techniques can provide a more complete and accurate experimental description of transient physical processes than measurements performed at only a single wavelength. This technique was applied to investigate exciton screening in high excited CdSe through measurements of the time resolved behavior of the exciton reflectivity resonance. The onset of screening by free carriers was observed to develop in less than 100 femtoseconds. This is the first investigation of screening in II-VI semiconductors performed with femtosecond time resolution.

In summary, this thesis has involved the establishment of a research program in high intensity femtosecond time resolved spectroscopy and has encompassed both the initial development and construction of an experimental laboratory facility as well as its applications to experimental investigations. Studies were performed which served to obtain new results on selected topics of current scientific interest in nonlinear optics and solid state physics as well as to develop and demonstrate new femtosecond generation and measurement techniques. Because of its unique capability of producing high intensity optical pulses with less than 100 femtoseconds time resolution, the femtosecond dye amplifier is a highly versatile and powerful experimental system which may be applied to the investigation of a wide variety of ultrafast phenomena. The application of high intensity femtosecond spectroscopy for future studies of semiconductors should be especially fruitful since many of the physical processes of interest in electronic and opto-electronic materials occur on a subpicosecond time scale.

APPENDIX A

INFLUENCE OF DEPHASING RELAXATION ON THE TRANSIENT PROPERTIES OF PARAMETRIC FOUR WAVE MIXING

A.1 INTRODUCTION

As discussed in Chapter 3, transient parametric four wave mixing has been demonstrated as a potentially valuable technique for the measurement of coherent transient behavior as well as optical gating (1-5). In this appendix we apply density matrix perturbation theory to analyze transient parametric scattering including the effects of both population and dephasing relaxation. Emphasis is placed on characterization of the transient behavior of the nonlinear process by measurement of the scattered pulse durations. Thus the influence of the material time constants on the actual transient properties of the four wave mixing process may be determined. The measurement of scattered pulse duration and energy is shown to provide a potentially more sensitive and complete indicator of incident pulse shape and material time constants than is obtainable from scattered energy measurements alone.

This research has been performed in collaboration with Dr. Ting K. Yee from Lincoln Laboratories as part of an ongoing research effort in theoretical nonlinear optics (6-8).* A summary of the investigation described in this appendix is scheduled for publication in (9).

---

*The author also wishes to acknolwedge Edward R. Bade for performing valuable preliminary numerical analysis in this investigation (10).

A.2 DENSITY MATRIX DESCRIPTION OF PARAMETRIC SCATTERING

Let us begin by constructing a description of transient parametric scattering four-wave-mixing based on density matrix perturbation theory. Two intense laser pulses with fields E_1, E_2 and wavevectors k_1, k_2 are directed into a thin nonlinear sample in a copropagating, nearly collinear geometry. The pulses interact via a third order nonlinearity to produce parametric scattering fields with wavevectors $2k_1-k_2$ and $2k_2-k_1$. This process may be rigorously described by density matrix perturbation theory. For simplicity, assume that the fields interact with a two level system consisting of a ground state g and an excited state n. Then the parametric four-wave-mixing may be described by density matrix perturbation terms $\rho_{ng}^{(3)}$ at $2k_1-k_2$ and $2k_2-k_1$.

We apply a recently developed diagrammatic density matrix perturbation technique to facilitate the construction and physical interpretation of the integral solutions for the density matrix terms (6,11,12). Consider the parametric signal at $2k_1-k_2$. There are a total of four perturbation terms which contribute to $\rho_{ng}^{(3)}$. These are represented diagrammatically as shown in Figure A.1. Equations A.1 and A.2 are the density matrix solutions which correspond to the diagrams A.1a and A.1b while the solutions corresponding to diagrams A.1c and A.1d are identical to equations A.1 and A.2 if the ground state population relaxation time is equal to that of the excited state.

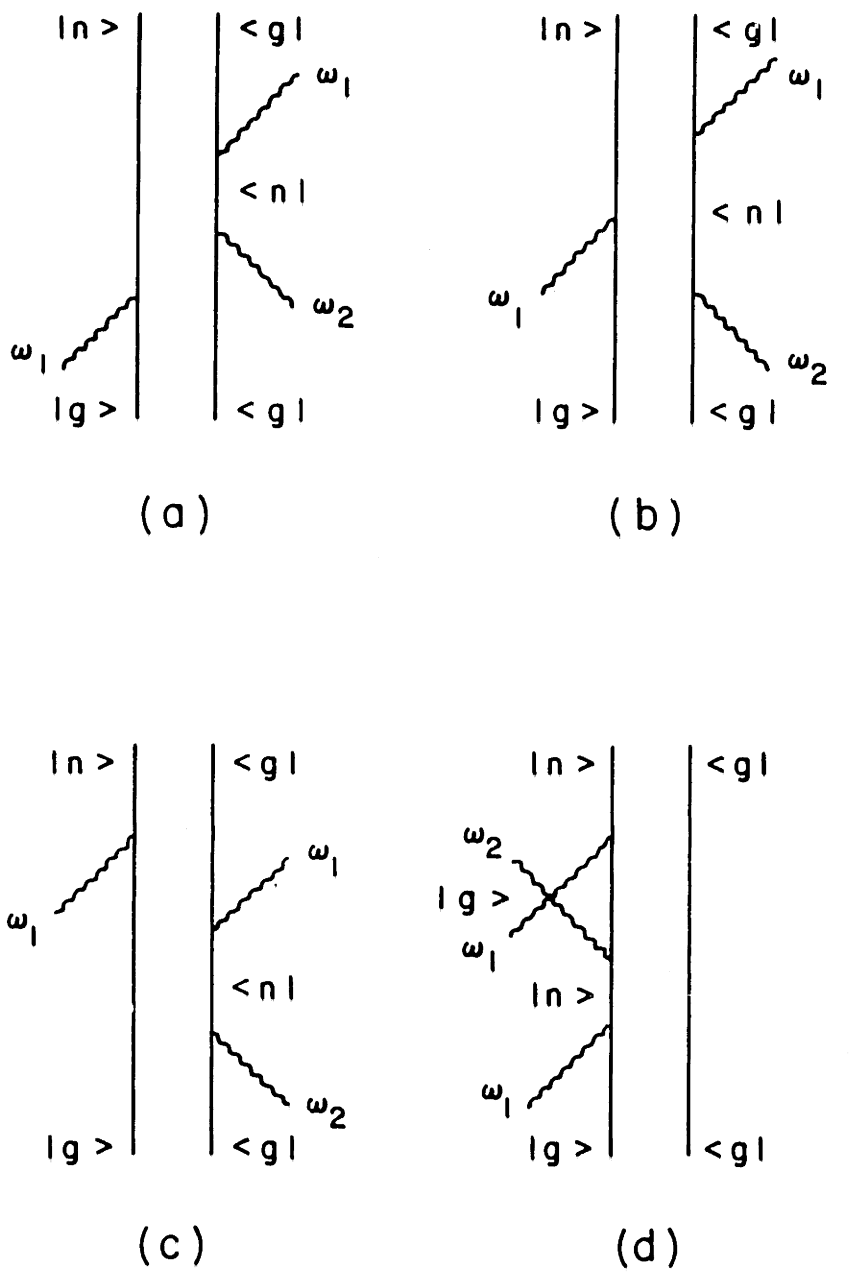

Figure A.1 Diagrammatic representation of density matrix terms contributing to parametric scattering.

$$(A.1)\qquad \rho_{ng}^{(3)}(t) = -(2\hbar)^{-3}$$

$$\int_{-\infty}^{t} dt_3 \exp\{-i(\omega_{ng}-i/T_2)(t-t_3)\}\ \mu_{ng}\cdot E_1(t_3+\Delta T)\ \exp\{-i\omega_1 t_3\}$$

$$\int_{-\infty}^{t_3} dt_2 \exp\{-(t_3-t_2)/T_1\}\ \mu_{gn}\cdot E_2^{*}(t_2)\ \exp\{+i\omega_2 t_2\}$$

$$\int_{-\infty}^{t_2} dt_1 \exp\{-i(\omega_{ng}-i/T_2)(t_2-t_1)\}\ \mu_{ng}\cdot E_1(t_1+\Delta T)\ \exp\{-i\omega_1 t_1\}\ \rho_{gg}^{(0)}$$

$$(A.2)\qquad \rho_{ng}^{(3)}(t) = -(2\hbar)^{-3}$$

$$\int_{-\infty}^{t} dt_3 \exp\{-i(\omega_{ng}-i/T_2)(t-t_3)\}\ \mu_{ng}\cdot E_1(t_3+\Delta T)\ \exp\{-i\omega_1 t_3\}$$

$$\int_{-\infty}^{t_3} dt_2 \exp\{-(t_3-t_2)/T_1\}\ \mu_{ng}\cdot E_1(t_2+\Delta T)\ \exp\{-i\omega_1 t_2\}$$

$$\int_{-\infty}^{t_2} dt_1 \exp\{-i(\omega_{gn}-i/T_2)(t_2-t_1)\}\ \mu_{gn}\cdot E_2^{*}(t_1)\ \exp\{+i\omega_2 t_1\}\ \rho_{gg}^{(0)}$$

The parametric process at $2k_2-k_1$ is described by identical equations and diagrams with the field variables interchanged.

The diagrams provide a graphic illustration of the time evolution of the density matrix perturbation terms. Time is plotted vertically and the ket and bra components of the density matrix are represented by labelled vertical lines. The perturbation matrix elements consist of dipole interactions with the fields and are represented by interaction vertices. In order to develop a physical interpretation for the parametric scattering process, let us consider diagram A.1a and the density matrix solution that it represents. The field E_1 first interacts with the ket component of the density matrix at time t_1 to produce a polarization $\rho_{ng}^{(1)}$ which decays exponentially with the dephasing relaxation time T_2. At time t_2 the field E_2^{*} interacts with the bra components of $\rho_{ng}^{(1)}$ to produce a population of $\rho_{nn}^{(2)}$. This excited population has a periodicity given by k_1-k_2 and

relaxes with a time constant T_1. Finally, at t_3, the population scatters the field E_1, as represented by the interaction of E_1 with the bra component of $\rho_{nn}^{(2)}$, to produce a polarization $\rho_{ng}^{(3)}$ in the $2k_1-k_2$ direction. Diagram A.1b is similar to diagram A.1a except that the first two interactions occur with the opposite time ordering. Taken together, diagrams A.1a and A.1b represent the scattering of the field E_1 by a periodic population produced in the upper level n by $E_1E_2^*$. Diagrams A.1c and A.1d describe scattering by population changes produced in the ground state.

A.3 NUMERICAL SOLUTIONS OF PULSEWIDTH AND ENERGY

Before attempting a numerical evaluation of the density matrix solutions we shall assume for simplicity that the frequency of the incident fields is on resonance with the quantum system. The solutions may then be expressed as integrals over the field envelope functions so that equations A.1 and A.2 reduce to equations A.3 and A.4 respectively.

$$\rho_{ng}^{(3)}(t) \sim \int_{-\infty}^{t} dt_3 \exp\{-(t-t_3)/T_2\}\, E_1(t_3+\Delta T) \int_{-\infty}^{t_3} dt_2 \exp\{-(t_3-t_2)/T_1\}\, E_2^*(t_2) \int_{-\infty}^{t_2} dt_1 \exp\{-(t_2-t_1)/T_2\}\, E_1(t_1+\Delta T) \tag{A.3}$$

$$\rho_{ng}^{(3)}(t) \sim \int_{-\infty}^{t} dt_3 \exp\{-(t-t_3)/T_2\}\, E_1(t_3+\Delta T) \int_{-\infty}^{t_3} dt_2 \exp\{-(t_3-t_2)/T_1\}\, E_1(t_2+\Delta T) \int_{-\infty}^{t_2} dt_1 \exp\{-(t_2-t_1)/T_2\}\, E_2^*(t_1) \tag{A.4}$$

The field envelope functions may be interpreted as perturbing signals while the exponential factors are the system impulse responses. The parametric polarization envelope function is thus given by a multiple convolution integral. The first integral over t_1 describes the polarization produced by E_1 or E_2^* and decays with a time constant given by the dephasing time T_2. The second integral describes the interactions of the second field to produce an excited population grating which decays with a time constant T_1. Finally, the last integral describes the polarization produced by scattering the field E_1 with the population excitation.

In the limit where the pulsewidth is long compared to the dephasing time, the field envelope functions may be treated as slowly varying with respect to the polarization response of the quantum system. The integrals over t_1 and t_3 may be eliminated to reduce equations A.3 and A.4 to:

$$(A.5) \qquad P^{(3)}(t,\Delta T) \sim E_1(t+\Delta T) \int_{-\infty}^{t} dt' \; E_2^*(t') E_1(t'+\Delta T)$$

The polarizations respond instantaneously and follow the incident field envelopes while the integral over t_2 describes the excited population produced by the product of fields $E_1 E_2^*$. Note that in this limit there is no significance to the time ordering of the first two interactions so that the contributions from diagrams A.1a and A.1b become identical, as do those from A.1c and A.1d.

Equations A.3 and A.4 may be integrated to describe the parametrically scattered pulse. The transient properties of the parametric signal may be conveniently described by measuring the pulse duration as determined by the full-width at half-maximum FWHM of the scattered intensity $I \sim P^2$. The total energy of the parametric signal may be obtained by integrating the

intensity:

$$\text{(A.6)} \qquad \varepsilon(\Delta T) \sim \int_{-\infty}^{\infty} dt \; |P^{(3)}(t,\Delta T)|^2$$

Figures A.2-A.4 illustrate the parametric signal FWHM and energy as a function of the delay between the incident pulses ΔT. The curves are computed for several values of T_1 and T_2 to demonstrate the effect of the material time constants on the parametric scattering. The incident pulse shape is gaussian with unity FWHM pulse duration. Figures A.5-A.10 present results obtained using sech and double-sided exponential pulse shapes.

A.4 DISCUSSION AND PHYSICAL INTERPRETATION

The general qualitative features of the theoretical results may be readily explained in terms of the previous diagrammatic model and its physical interpretation. Let us first consider the process in the simplest limits when T_1 and T_2 are shorter than the incident pulse width, $T_1 \ll t_p$ and $T_2 \ll t_p$. Under these conditions, the response of the nonlinear material will be instantaneous and there will be negligible polarization or population memory. The parametric polarization is then given by the product of the incident fields $P^{(3)} \sim E_1(t+\Delta T)E_2^*(t)E_1(t+\Delta T)$. The pulsewidth and energy of the parametric signal are determined from $I \sim |P^{(3)}|^2$ and equation A.6. If the incident pulseshapes are symmetrical and equal in amplitude, then both the energy and pulsewidth are symmetric functions of ΔT. The behavior of the parametric signal energy as a function of incident pulse separation depends upon the energy in the wings of the incident pulses. For gaussian pulses, the scattered parametric energy

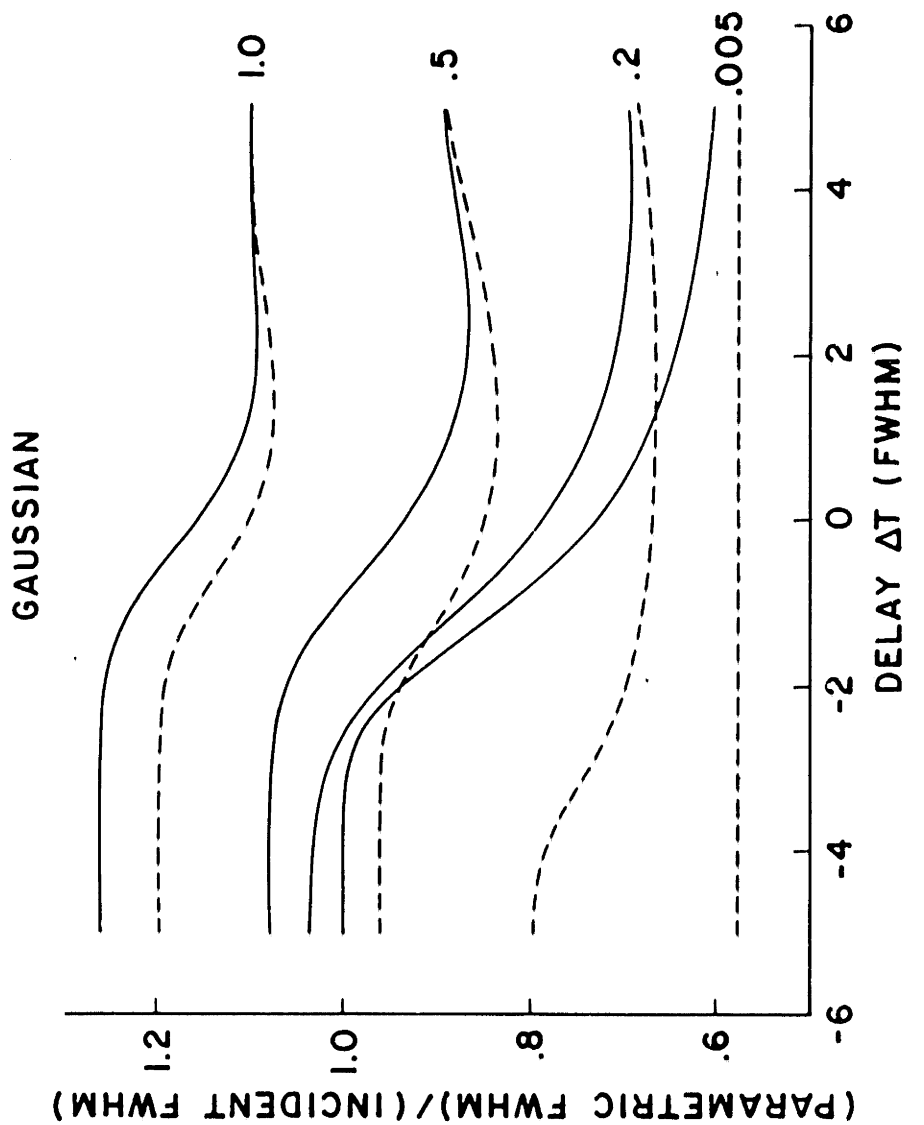

Figure A.2 Parametric pulse FWHM vs. incident pulse separation for gaussian pulses. Dashed curves are for different values of $T_1=T_2$. Solid curves are for $T_1 \to \infty$ with T_2 as labelled.

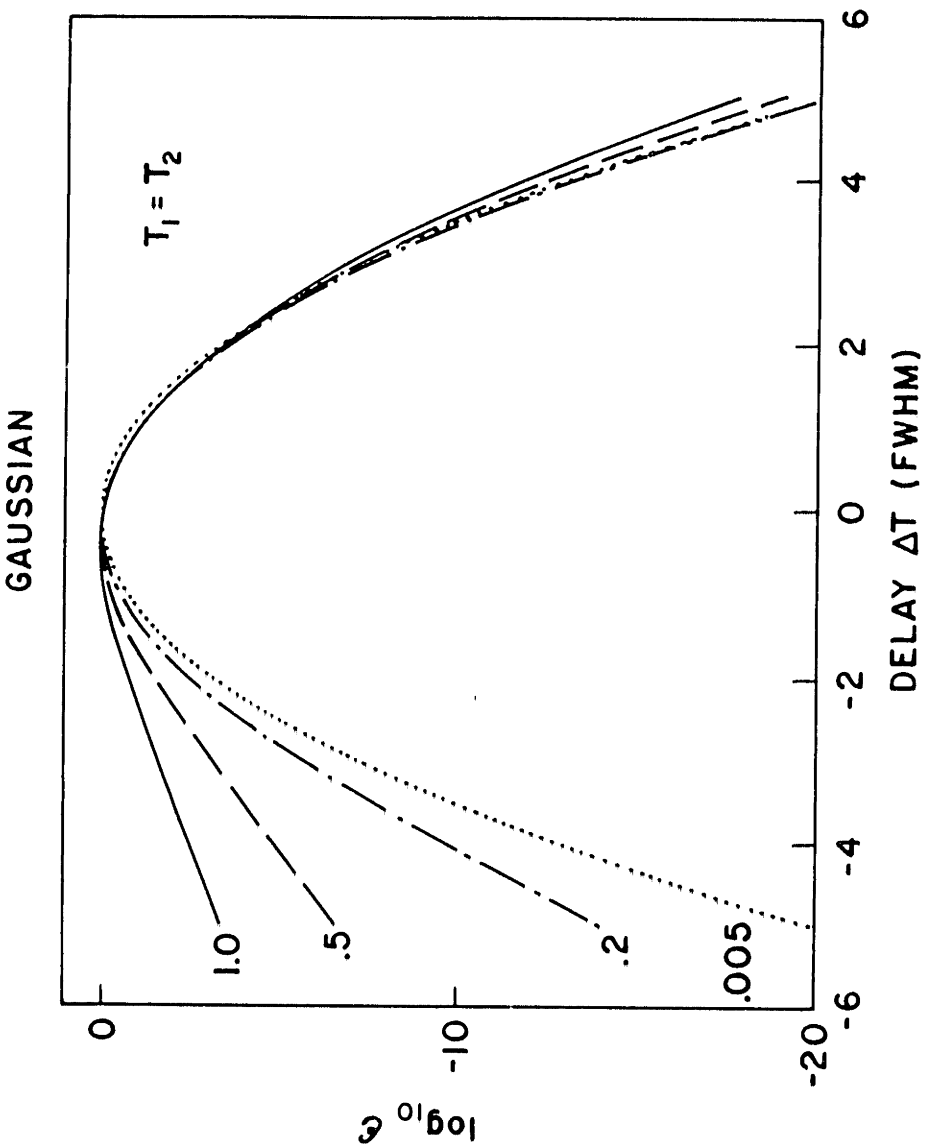

Figure A.3 Parametric pulse energy vs. incident pulse separation for gaussian pulses and $T_1=T_2$. Labelled curves are for different values of $T_1=T_2$.

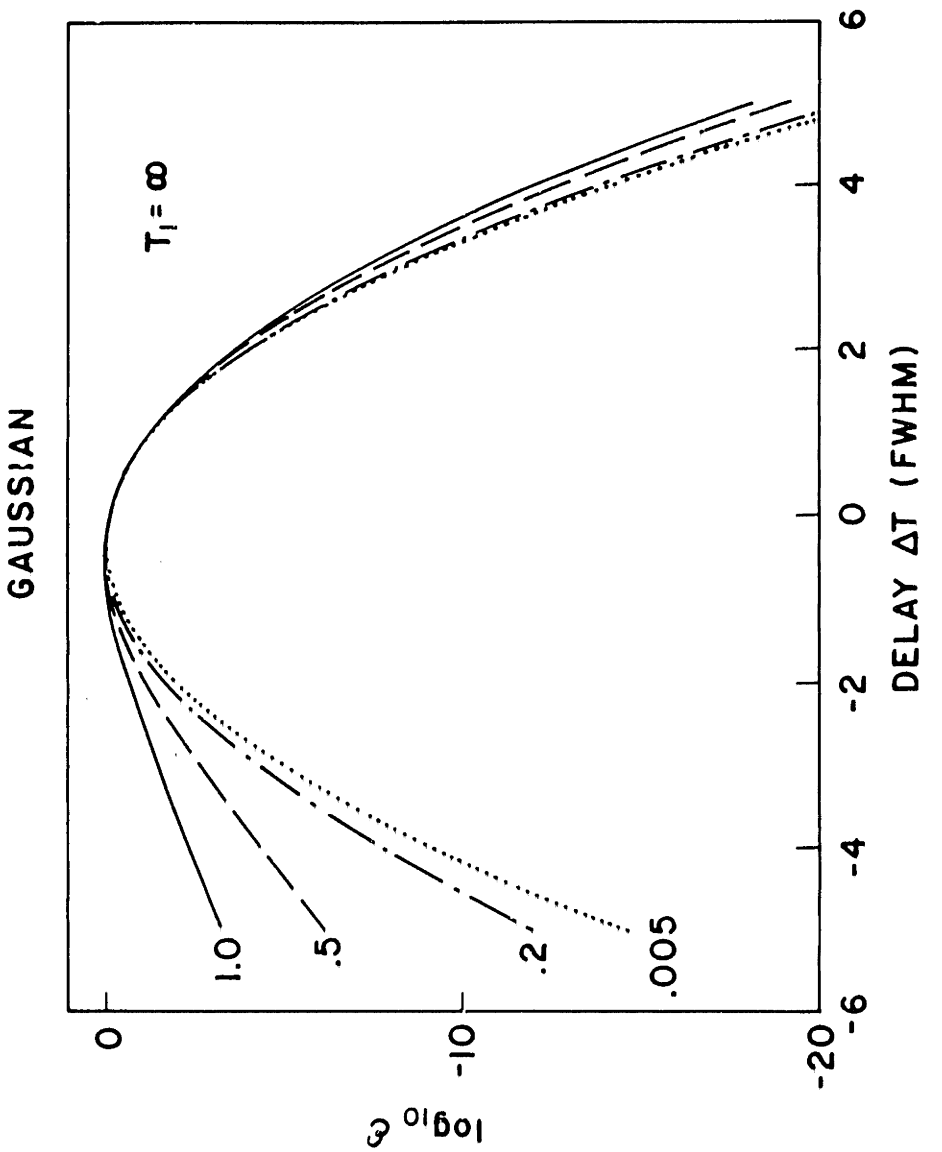

Figure A.4 Parametric pulse energy vs. incident pulse separation for gaussian pulses with $T_1 \to \infty$. Labelled curves are for different values of T_2.

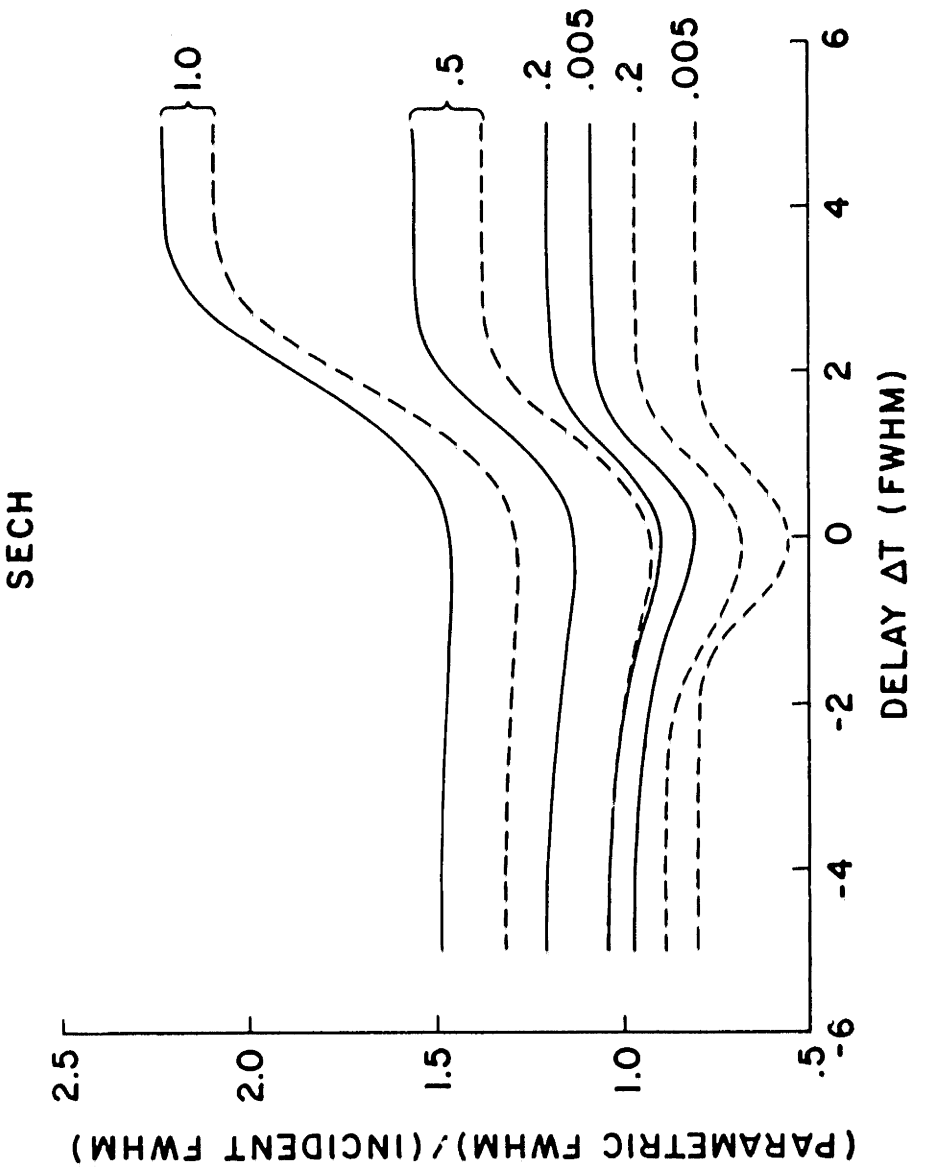

Figure A.5 Parametric pulse FWHM vs. incident pulse separation for sech pulses. Dashed curves are for different values of $T_1=T_2$. Solid curves are for $T_1 \to \infty$ with T_2 as labelled.

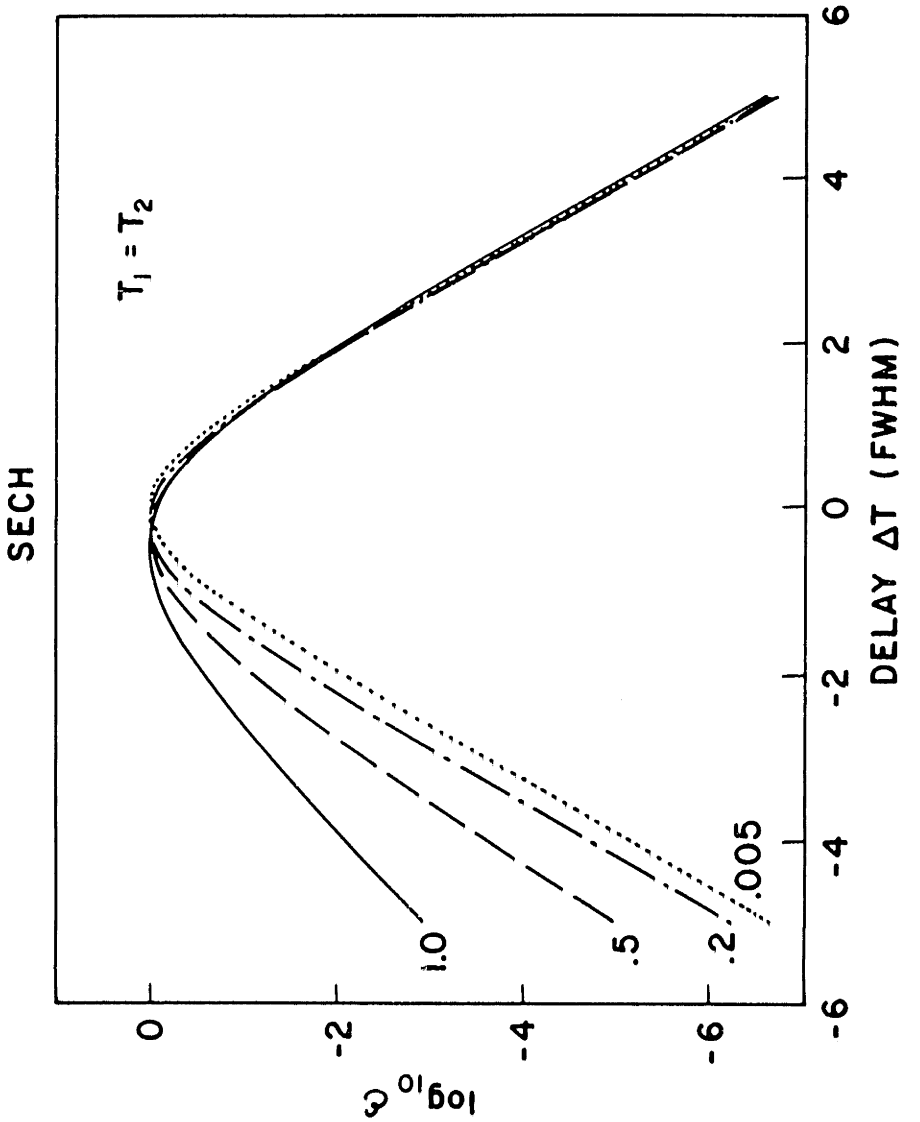

Figure A.6 Parametric pulse energy vs. incident pulse separation for sech pulses and $T_1=T_2$. Labelled curves are for different values of $T_1=T_2$.

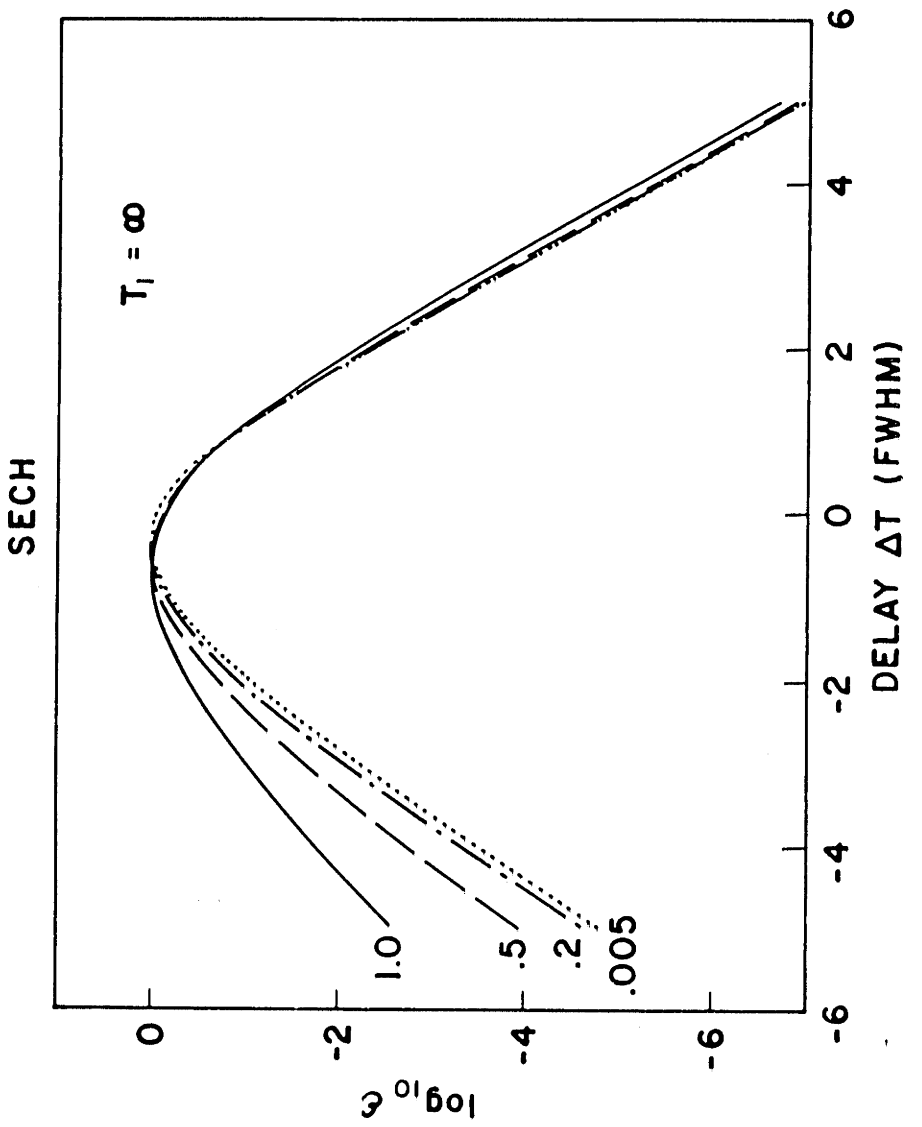

Figure A.7 Parametric pulse energy vs. incident pulse separation for sech pulses and $T_1 \rightarrow \infty$. Labelled curves are for different values of T_2.

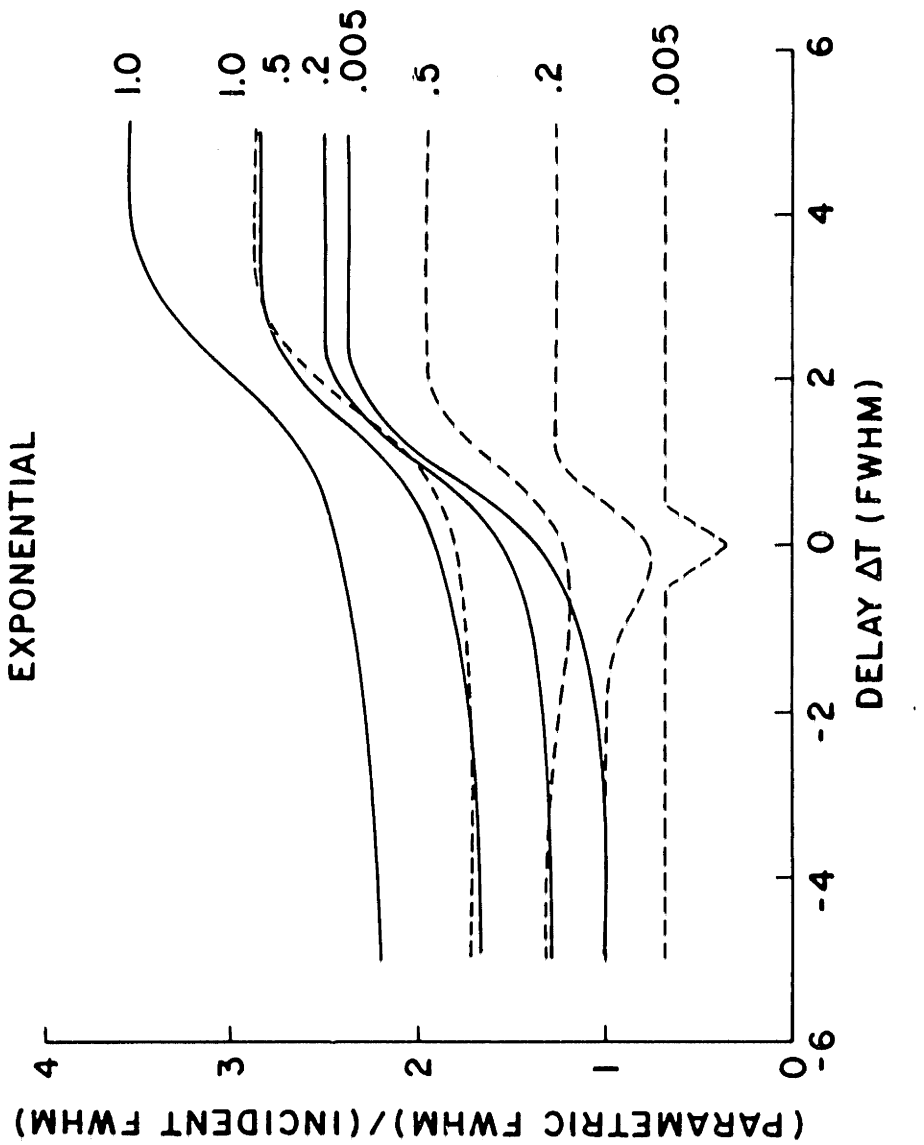

Figure A.8 Parametric pulse FWHM vs. incident pulse separation for double exponential pulses. Dashed curves are for $T_1=T_2$. Solid curves are for $T_1 \to \infty$ with T_2 as labelled.

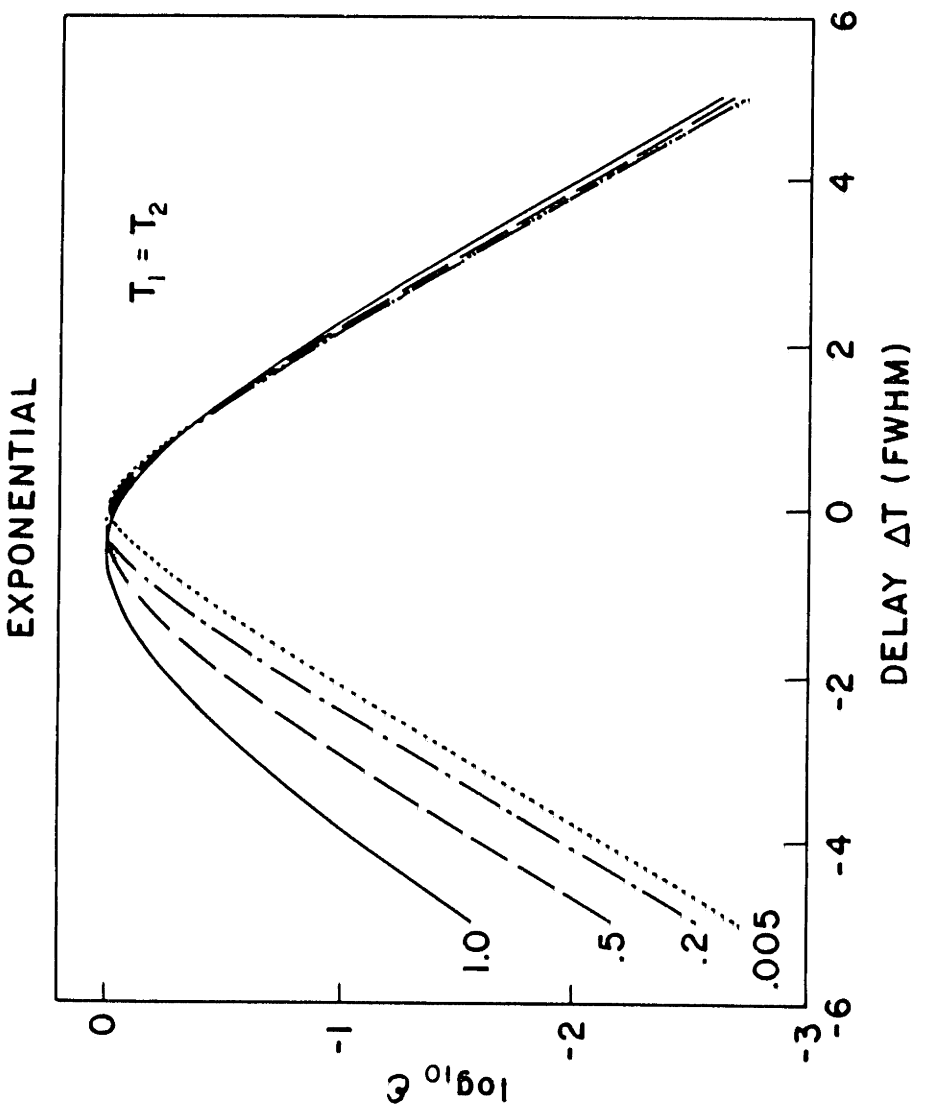

Figure A.9 Parametric pulse energy vs. incident pulse separation for double exponential pulses and $T_1=T_2$. Labelled curves are for different values of $T_1=T_2$.

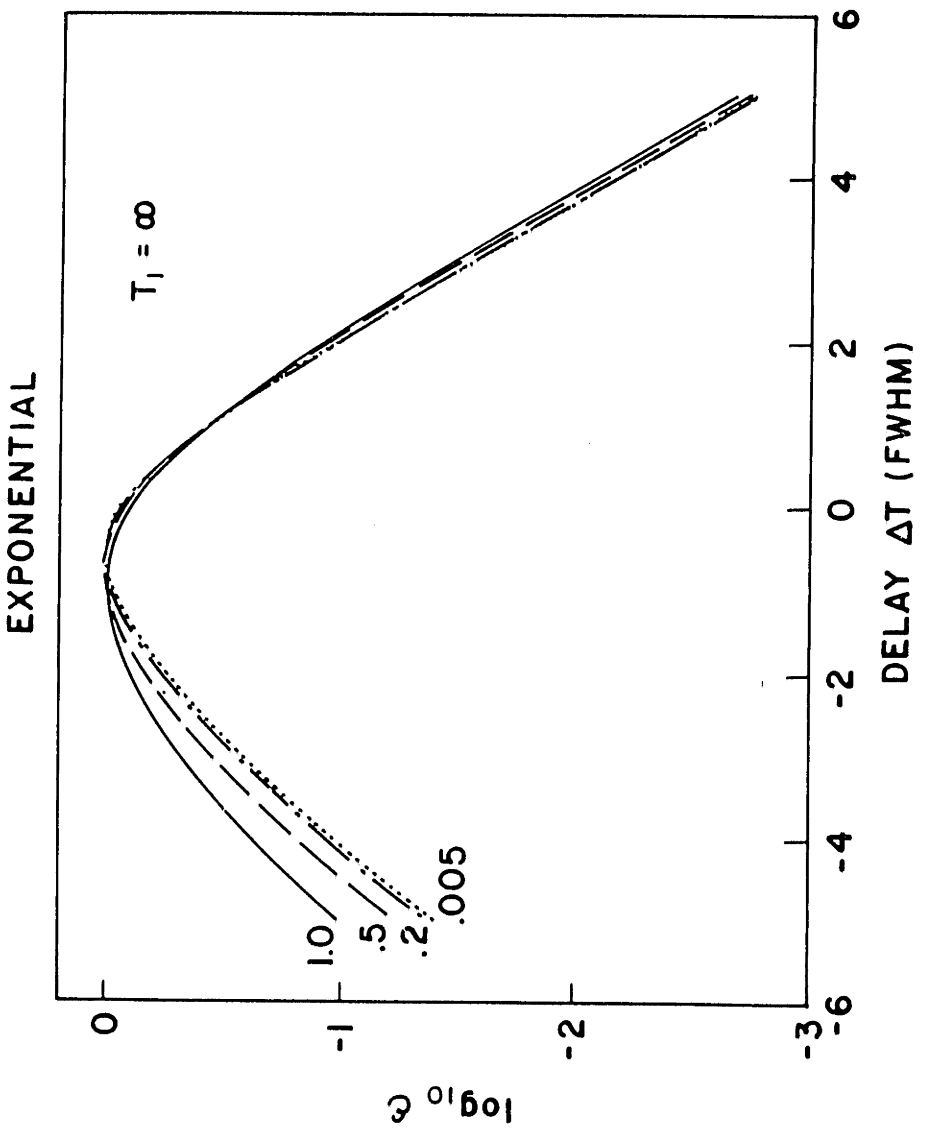

Figure A.10 Parametric pulse energy vs. incident pulse separation for double exponential pulses and $T_1 \rightarrow \infty$. Labelled curves are for different values of T_2.

decreases in proportion to $\exp(-C\Delta T^2)$. This is manifest as a parabolic behavior of the log energy curve for $T_1=T_2=.005$ in Figure A.4. Conversely, for sech or double sided exponential pulses, the parametric energy decreases exponentially with ΔT as evident in the $T_1=T_2=.005$ curves in Figures A.7 and A.10.

As described previously, the pulsewidth of the parametric signal is determined by the product of the incident fields. Note that for $\Delta T=0$ the incident pulses overlap temporarily and $P^{(3)}\sim E^3$ so that the parametric pulsewidth will be determined by the cube of the incident pulse shape. For the case of gaussian pulses with unity FWHM, the product $E_1(t+\Delta T)\ E_2^*(t)E_1(t+\Delta T)$ is always gaussian with pulse duration $1/\sqrt{3}$ irrespective of the delay ΔT. However, for sech and exponential pulses, the product will have a minimum pulse duration for $\Delta T=0$. This is in agreement with the theoretical results obtained for $T_1=T_2=.005$ shown in Figures A.2, A.5, and A.8.

In the limit where $T_2<<t_p$ but T_1 is arbitrary, the polarization response of the nonlinear material will follow the incident pulseshapes but the population will decay with a time constant T_1. The parametric signal is then described by equation A.5. When T_1 is comparable to or longer than the incident pulse duration, there is population memory. Thus, for the parametric signal at $2k_1-k_2$, the scattering of the field $E_1(t+\Delta T)$ will be enhanced when it arrives after the excited population is produced. The scattering for $\Delta T<0$ increases and the maximum of the energy versus ΔT curve is shifted to negative values of delay.

The transient population may be viewed as an optical gate which scatters the incident field E_1. If $\Delta T<0$ the population is created early in the pulse envelope of E_1, then a large portion of E_1 pulse is scattered.

Conversely, if $\Delta T>0$, the population is created later in the pulse so only the trailing edge of E_1 is scattered. This explains the asymmetric dependence of the scattered pulsewidth on ΔT. In general, increasing T_1 will increase the asymmetry in both the energy and pulsewidth curves. This may be easily seen in the $T_1 \to \infty$, $T_2 = .005$ curves of Figures A.2-A.10.

Note that although the total parametric process is in general an asymmetric function of the incident pulse separation ΔT, the amplitude of the excited population grating produced by $E_1(t+\Delta T)$ and $E_2^*(t)$ is symmetric in ΔT. This symmetry may be seen directly from the diagrammatic representation of the parametric process by noting that the diagrams in Figure A.1 contain both possible time orderings of the first two interaction vertices.

For nonlinear materials where the dephasing time T_2 is not negligible in comparison to the incident pulse duration, the polarization response of the material will tend to persist after the excitation. Since the polarization response lasts longer than the incident field, the scattered parametric energy (for the $2k_1-k_2$ direction) will be enhanced when the $E_1(t+\Delta T)$ pulse arrives after the excited population grating is produced by $E_1(t+\Delta T)$ and $E_2^*(t)$. This yields a relative increase in parametric signal energies for negative values of delay T which is manifest as an asymmetry and peak shift in the energy versus delay curves. As shown in Figures A.3, A.4, A.6, A.7, A.9, and A.10, the parametric energy decreases approximately exponentially for $\Delta T<-1$. If T_2 is comparable to or longer than the incident pulsewidth, contributions from the material dephasing time dominate over incident pulse shape effects and the exponential decay is governed by T_2. In contrast, for positive values at ΔT, the scattered

parametric energy is almost independent of the dephasing time and is determined chiefly by the incident pulse shape.

The dephasing time has a direct effect on the duration of the scattered parametric pulse. There are two mechanisms by which the T_2 time governs the transient properties of the parametric signal. First, since the excited population grating is produced by the polarizations induced by E_1 and E_2^*, longer dephasing times will slow down the risetime of the population. Since the population acts as an optical gate, this directly limits the risetime of the signal which is gated. In addition, the transient parametric signal depends on the scattering of the polarization induced by the E_1 field as shown by the last interaction vertices of the diagrams in Figure A.1. A slower dephasing time produces a longer polarization response and hence a longer scattered parametric pulse. Increasing T_2 thus yields a large increase in parametric pulse duration.

Finally, it is important to note that the behavior of the parametric pulse duration is strongly dependent on incident pulse shape. Recall that the pulse duration is determined by the risetime of the excited population grating as well as the time at which the population is produced relative to the pulse being scattered. If the incident pulses are gaussian, the risetime of the population is independent of the incident pulse separation ΔT. In contrast, for sech or double sided exponential pulses, population risetime depends on ΔT and is in fact fastest for $\Delta T=0$. Even if the parametric signal could be produced by scattering from a transient population having an invariant and constant risetime, differences in the incident pulse shape would still be manifest in the scattered parametric pulse. In general, the parametric pulse duration is very sensitive to the rate of energy decrease in the wings of the incident pulse relative to its maximum.

Thus gaussian, sech, and double sided exponential pulses produce strikingly different functional behavior of parametric pulse duration versus ΔT. As shown in Figures A.2, A.5, and A.8, these differences remain manifest even for values of T_1 and T_2 comparable to the incident pulse duration.

A.5 EXPERIMENTAL IMPLICATIONS

Let us now consider the experimental implications of our theoretical analysis of parametric scattering. For measurements of scattered energy, the effects of pulse shape are manifest by the rate of decrease of the energy versus incident pulse separation, while the asymmetry provides information about material time constants. A sensitive analysis of material time constants and pulse shape relies on experimental measurements of the wings of the energy versus ΔT curves. Thus the optimum experimental implementation of this technique requires the use of laser pulses which are highly temporally coherent and the achievement of large signal to noise ratios to allow the measurement of the variation of the parametric energy over several orders of magnitude. Recognizing these concerns, previous investigators (1,2) have employed the peak shift rather than the asymmetry in the energy versus ΔT curves for experimental measurements of dephasing time. Another alternative is a recently described, multiple pulse, transient four-wave-mixing technique (13). The recent development of stable, transform limited sources of subpicosecond pulses has the potential for achieving the high sensitivity and dynamic range desirable for experimental characterization of dephasing times using scattered energy.

As shown by our theoretical results, measurement of scattered parametric pulse duration also provides a sensitive indication of material time constants and incident pulse shape. In particular, pulse duration is

especially sensitive to pulse shape effects which are not as manifest in scattered energy measurements. It is important to note that the energy versus ΔT curves impose practical restrictions on the pulsewidth data which may be experimentally obtained since pulsewidth measurements require sufficient parametric signal energy. However, in contrast to the scattered energy measurements, the pulse duration provides information about material time constants and incident pulse shape even when measurements are performed for relatively small values of incident pulse separation ΔT. As shown in Figures A.2, A.5, and A.8, the strongest functional dependence of the pulsewidth occurs for values of ΔT near zero. Finally, it should be stressed that the scattered pulse duration measurement provides a direct indication of the influence of material time constants on the transient behavior and speed of the four-wave-mixing optical gating process.

A.6 SUMMARY

In summary, we have applied density matrix perturbation theory to analyze transient parametric scattering with special emphasis on the measurement of scattered pulse duration as well as scattered energy. This approach was shown to have the potential for a more sensitive and complete indication of material time constants and incident pulse shape than possible from measurements of scattered energy alone. In addition, our results stress the importance of the theoretical and experimental consideration of the actual transient temporal properties inherent in four wave mixing processes. These issues are relevant not only to the measurement of fast material time constants but also to applications of transient nonlinear processes for fast optical signal processing.

REFERENCES

1. T. Yajima and Y. Taira, "Spatial Optical Parametric Coupling of Picosecond Light Pulses and Transverse Relaxation Effect in Resonant media," J. Phys. Soc. Japan 47, 1620 (1979).

2. T. Yajima, Y. Ishida, and Y. Taira, "Investigation of Subpicosecond Dephasing Processes by Transient Spatial Parametric Effect in Resonant media," in Picosecond Phenomena II, R. Hochstrasser, W. Kaiser, and C.V. Shank Eds. Berlin, Germany: Springer-Verlag, 1980, pp. 190-194.

3. A.L. Smirl, T.F. Boggess, B.S. Wherrett, G.P. Perryman, and A. Miller, "Picosecond Optically Induced Anisotropic State Filling in Semiconductors," Phys. Rev. Lett. 49, 933 (1982).

4. B.S. Wherrett, A.L. Smirl, and T.F. Boggess, "Theory of Degenerate Four-Wave Mixing in Picosecond Excitation-Probe Experiments," IEEE J. Quantum Electron. QE-19, 680 (1983).

5. J.G. Fujimoto and E.P. Ippen, "Transient Four-Wave Mixing and Optical Pulse Compression in the Femtosecond Regime," Opt. Lett. 8, 446 (1983).

6. J.G. Fujimoto and T.K. Yee, "Diagrammatic Analysis of Third Order Nonlinear Optical Processes," IEEE J. Quantum Electron. QE-19, 861 (1983).

7. J.G. Fujimoto and T.K. Yee, "Diagrammatic Density Matrix Analysis of Transient Third Order Nonlinear Processes," presented at the Annual Meeting of the Optical Society of America, New Orleans, LA, October 1983.

8. T.K. Yee and J.G. Fujimoto, "Generalized Analysis of Pressure Induced Nonlinear Optical Processes," Optics Communications, in press.

9. J.G. Fujimoto and T.K. Yee, "Influence of Dephasing Relaxation on the Transient Properties of Parametric Four-Wave Mixing," Applied Physics B, in press.

10. E.R. Bade, "Optical Pulse Compression and Transverse Relaxation in Four Wave Mixing," S.B. Thesis, Department of Electrical Engineering and Computer Science, Massachusetts Institute of Technology (1983).

11. S.Y. Yee, T.K. Gustafson, S.A.J. Druet, and J.-P.E. Taran, "Diagrammatic Evaluation of the Density Operator for Nonlinear Pptical Calculations," Opt. Commun. 23, 1 (1977).

12. T.K. Yee and T.K. Gustafson, "Diagrammatic Analysis of the Density Operator for Nonlinear Optical Calculations: Pulsed and CW Responses," Phys. Rev. A, 18, 1597 (1978).

13. A.M. Weiner and E.P. Ippen, "Novel Transient Scattering Technique for Femtosecond Dephasing Measurements," Opt. Lett. 9, 53 (1984).